UNIVERSITY OF PÉCS

Doctoral School of Physics

Laser physics, nonlinear optics, and spectroscopy Program

Designs of optimized semiconductor contact grating terahertz sources

Ph.D. Thesis

Nelson Matheka Mbithi

Supervisor:

Dr. Gyula Polónyi

Pécs 2022

Acknowledgements

First and foremost, I would like to thank my supervisor, Dr. Gyula Polónyi, for his unwavering support and guidance over the 4 years. His knowledge of optics and terahertz generation has taught me a lot. I sincerely appreciate his efforts in assisting me with my Ph. D work. I'd also like to thank Prof. Dr. János Hebling for his assistance, guidance, advice, and discussions during the experiments and theoretical calculations. His high standards of achievement, as well as his research philosophy, have benefited me. I want to express my gratitude to Dr. Zoltán Tibai for discussions on contact grating simulations. I would also like to express my gratitude to Dr. György Tóth for providing MATLAB models for the numerical calculations of the terahertz generation. I would also like to thank Prof. József Andras Fülöp for introducing me to optics research, basics of terahertz generation, laser physics and his guidelines in my initial studies. I would also like to thank everyone at the Szentágothai THz laboratory who has assisted and helped me over the years. Special thanks to Dr. Priyo Syamsul Nugraha for introducing and teaching me the basics of laser and laboratory practices. I am grateful to all the staff members in the institute of physics at the University of Pecs for their encouragement and support during my study.

Last but not least, I would like to acknowledge every person who has contributed to the success of this research directly or indirectly. Finally, I am thankful to my family and the Garissa University fraternity for their support during my study.

Abstract

Numerical simulations were performed in the 1-5 μm wavelength range to investigate the possible advantage of using longer pumping wavelengths to suppress 2- to 7-photon absorption in GaAs and GaP for efficient terahertz pulse generation. A strong advantage of suppressing the lowest multiphoton absorption was realized. However, more than 0.9% and 1.14% conversion efficiency were predicted for GaAs and GaP, respectively, when the pump wavelength was long enough to allow only the 6^{th} or higher order multiphoton absorption. An optimum pulse duration of 125 fs was achieved in both GaP and GaAs at an optimum phase matching frequency of 2 THz. In addition, it was realized that the nonlinear refraction index could significantly reduce the terahertz generation efficiency and shorten the optimum wavelength to achieve the highest conversion efficiency. The optimum long pumping wavelength realized was 2 μm and 3 μm for GaP and GaAs, respectively. Furthermore, investigations of GaP and GaAs contact grating terahertz sources designs based on rectangular and trapezoidal profiles for phase-matched terahertz generation by optical rectification in the long infrared wavelength range were performed numerically. The calculations were done at transverse electric field (TE) and transverse magnetic field (TM) polarization states. Based on the rectangular grating profile, nearly wavelength-independent diffraction efficiencies as high as 69% and 75% in the ±1st diffraction orders in the TE polarization state were predicted in GaAs and GaP, respectively. In the TM polarization state, diffraction efficiencies as high as 80% and 82% were predicted in GaAs and GaP, respectively. Similar diffraction efficiencies as in rectangular profiles were predicted in the trapezoidal grating profile in both GaAs and GaP in TE and TM polarization states. The possibility of diffraction efficiency enhancement by applying an antireflective coating on the grating profiles was also investigated numerically. Diffraction efficiencies of more than 89% and 91% were predicted in GaAs and GaP, respectively, in the TE polarization state and at 3 μm and 2.06 μm pump wavelengths by adding an antireflective coating.

Table of Contents

Contents

List of Figures

List of Tables

List of Abbreviations and Acronyms

ARC Antireflective Coating

BS Beam Splitter

EOS Electrooptic Sampling

OR Optical rectification

GaP Gallium Phosphide

GaAs Gallium Arsenide

GaSe Gallium Selenide

GDD Group Delay Dispersion

GVD Group Velocity Dispersion

ZnTe Zinc Telluride

CdTe Cadmium Telluride

InP Indium Phosphate

InAs Indium Arsenide

InSb Indium Antimony

IR Infrared

SHG Second Harmonic Generation

SEM Scanning Electron Microscopy

THz Terahertz

TDTS Time-Domain Terahertz Spectroscopy

SFG Sum Frequency Generation

DFG Difference Frequency Generation

FFT Fast Fourier Transform

FCA Free Carrier Absorption

MPA Multiphoton Absorption

$LiNbO_3$ Lithium niobate

BBO Beta Barium Borate

InGaAs Indium Gallium Arsenide

InSb Indium Antimonide

IR	Infrared
PFT	Pulse Front Tilt
FWHM	Full Width at Half Maximum
TM	Transverse Magnetic field
TE	Transverse Electric field
CG	Contact Grating
D.E	Diffraction Efficiency
TPFP	Tilted Pulse Front Pumping
fs	Femtosecond
OPA	Optical Parametric Amplification
DAST	4-N-methylstilbazolium tosylate
DSTMS	4-N,N-dimenthylamino-4′N′-methyl-stilbazolium2,4,6-rimethylbenzenesulfonate
OH1	2-[3-(4hydroxystyryl)-5.5-dimethylcyclohex- 2-enylidene] malononitrile

List of symbols and Variables

λ_p	Pump wavelength
e	Elementary electric charge
T	Temperature
α	Linear absorption coefficient
τ	Pulse duration
c	Speed of light in vacuum
P	Polarization
ϵ_o	Permittivity of free space
ϵ_r	Relative permittivity
I	Intensity of laser
W	Laser power
E	Electric field
$\chi^{(1)}$	Linear susceptibility
$\chi^{(2)}$	Second order nonlinear susceptibility
$\chi^{(3)}$	Third-order nonlinear susceptibility
η_{THz}	THz generation efficiency
L	crystal length
l_{THz}	Terahertz interaction length
ω	Optical pump frequency
Ω	Terahertz frequency
E_g	Bandgap energy
d	Groove spacing
n_c	Index of coating material
t	Thickness of coating
λ_p	Pump wavelength
f	Duty cycle
β_n	n^{th} nonlinear absorption coefficient
h	Groove depth

d_1	Line width
ϕ	Wall angle
n_{opt}	Optical refractive index
n_{gr}	Group refractive index
n_{THz}	Terahertz refractive index
H	Magnetic field
J	Current density
l_c	Coherence length

Chapter One

1.0 Introduction

1.1 Terahertz radiation

Terahertz (THz) radiation is a type of electromagnetic radiation that exists between the infrared and microwave regions of the electromagnetic spectrum. Its frequency ranges from 0.1 to 10 THz (or wavelength ranges from 3 mm to 30 μm). Ideally, 1 THz frequency is equivalent to a wavelength of 300 μm, with a corresponding wavenumber of 33.3 cm^{-1}, and photon energy of 4.14 meV. Figure 1-1 shows the electromagnetic spectrum. The terahertz radiation is sometimes known as the "sub-millimeter wave" or "far-infrared" region of the electromagnetic spectrum. Terahertz radiations have the peculiar ability to penetrate various materials such as papers, plastics, cloths, nonpolar liquids, gases, and organic compounds.

Although there has been scientific interest in this frequency range since the early 1920s, when spectroscopists first used terahertz radiation to describe absorption and emission frequencies that fall below the far infrared [1]. However, due to inadequate technologies and a scarcity of high-energy THz sources and detectors, this part of the electromagnetic spectrum has remained one of the least explored [2]. Recent advances in THz sources have started to open the field to new applications. The sources of terahertz radiation are either natural or artificial. Natural sources involve radiations emitted as part of blackbody radiation with temperatures greater than 10 K [3], while artificial sources include; gyrotron, backward wave oscillators, and lasers [4]. Lasers play an essential role in terahertz pulse generation. Lasers are classified as continuous wave (CW) or pulsed laser systems. The pulsed laser emits electromagnetic radiation consisting of pulses, e.g., femtosecond lasers, while the continuous laser emits continuous electromagnetic pulses. With the emergence of femtosecond lasers, THz science has rapidly grown, increasing the development of new and improved terahertz generation and detection techniques.

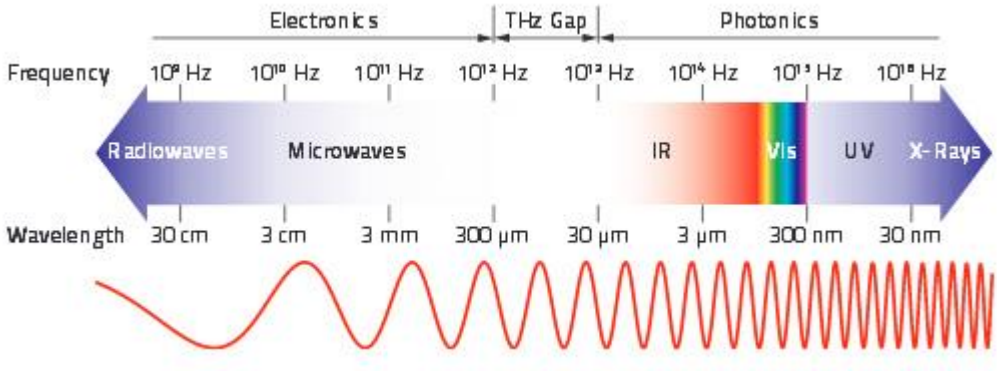

Figure 1- 1:The electromagnetic spectrum [5].

Several techniques, including photoconductive antennae, laser-plasma based, and optical rectification and free electron lasers, have been explored to generate terahertz radiation. In photoconductive antennae, a femtosecond laser pulse induces photoexcitation of charge carriers in a semiconductor substrate. The charges are subsequently accelerated by a biased electric field, resulting in a time-varying current that emits terahertz radiation. However, there are disadvantages associated with this technique that include: saturation at low excitation fluences, thereby limiting scalability [6], it requires high bias voltage for compensation of high power dissipation, and noise resulting from the high-voltage switching circuits, and the generated THz pulses have low energy and field strength. The highest reported THz pulse energy in photoconductive antenna is 8.3 µJ generated from interdigitated ZnSe with an aperture size of 12.2 cm^2 illuminated with a 400 nm pump laser with multi-mJ energies at 10 Hz repetition rate [7]. The laser-based plasma technique, on the other hand, allow for the use of high intensities for terahertz generation because there is no damage threshold, resulting in generation of ultrabroadband THz pulses with up to µJ (0.1-1 µJ) [8] pulse energy in the range 1-100THz. However, the terahertz generation conversion efficiency still very low [9] and upscaling to higher energies is difficulty due to plasma instabilities [10, 11]. In addition, electron accelerator-based THz sources delivers THz pulses with µJ to mJ range with high field strengths more than 100 MV/cm [12] , but this source is limited due to inaccessibility of the large scale facilities. Furthermore, optical rectification is the most efficient and effective technique for generating terahertz radiations in nonlinear crystals using femtosecond laser pulses. It allows scaling of terahertz pulses by increasing fluence and results in the generation of pulses with broad bandwidth [13]. So far, using optical rectification in combination of tilted-pulse-front technique in lithium niobate THz pulse energy of 1.4 mJ [14], a peak electric field as

high as 6.3 $MVcm^{-1}$ [14], and a conversion efficiency of 3.8% [15] have been reported. Terahertz pulses have also been generated in organic crystals such as DAST [16] , DSTMS [17], OH1 [18] by optical rectification. For instance, terahertz pulses with energies of 0.9 mJ and conversion efficiency of 5.7% have been demonstrated in DSTMS pumped at collinear geometry [16, 17]. Terahertz pulses have also been reported to be generated in semiconductors such as ZnTe [19], GaP [20], GaAs [21], GaSe [22] among other nonlinear media. More details of optical rectification technique will be discussed in chapter 2. Optical rectification in nonlinear media has enabled the development of novel THz sources with microjoule to millijoule energy range [23-25]. However, despite the advances in THz science, only a few high energy THz sources based on optical rectification in semiconductors have been reported [19], hence, the need to develop more high-intensity semiconductor THz sources for application in spectroscopy, medicine, material science, among others. Therefore, this work aims to numerically design and optimize scalable and highly efficient semiconductor contact grating terahertz sources that can be pumped at a long infrared wavelength range.

1.2 Application of THz pulses

The advent of THz sources which can generate pulses with high energies and peak electric and magnetic fields in the THz range (0 to 10THz) has made feasible applications. These applications are based on the materials' responses to fundamental processes such as lattice vibrations in solids, vibrational motions in organic compounds, and rotational transitions in molecules on interaction with terahertz radiations. For instance, in medicine, high energy THz pulses have been applied to image a gelatin-soluble medicine capsule using computed tomography [26, 27], and most recently, proposed for hadron therapy [28]. It can also be a good substitute to X-rays in imaging live tissues and cells since it is non-invasive. In material science, intense THz pulses have enabled the investigation of hydrogen bromide molecules orientation and alignment [29], electron-hole re-collisions in semiconductor quantum wells [30], ultrafast carrier dynamics in semiconductors [31], nonlinear responses in nanotubes [32], quality control [33], and non-perturbative interband responses in semiconductor materials [34], analysis to monitor illegal materials such as explosives and illicit drugs for security applications [35] and nonlinear spectroscopy, resonant and nonresonant control of matter [36]. In strong-field physics, intense THz pulses have been used for particle acceleration [37, 38], post acceleration to higher energies [39] and

manipulation of charged particles [40], as well as longitudinal compression and acceleration of relativistic electron bunches [41, 42] and electron undulation [43].

1.3 Organization of the Thesis

This dissertation is organized in eight chapters: Chapter 1 describes an overview of the THz radiation and, their applications. Chapter 2 discusses the theory of nonlinear optical processes and optical rectification as a techniques of terahertz pulse generation, THz sources based on optical rectification and the theory of multiphoton absorption. Chapter 3 contains the motivation and scientific goals. Chapter 4 describes theoretical model for investigation of single-cycle terahertz pulse generation in semiconductors. The schemes of contact grating THz source, with an emphasis on rectangular and trapezoidal grating structures are described. Rectangular grating structures with antireflective coatings are also described.

Chapter 5 contains the results and discussion of designs of semiconductor contact gratings, as well as numerical calculations of the single-cycle terahertz pulse generation in gallium arsenide and gallium phosphide. Chapter 6 contains a conclusion and outlook of the study. Chapter 7 contains the thesis statements. Chapter 8 and 9 contains the summaries of my study.

Chapter Two

2.1 Nonlinear optical processes

When a femtosecond laser pulse propagates through a nonlinear material, it induces a time-dependent polarization change, resulting in the emission of electromagnetic radiation. The scalar relationship between the polarization P, linear electric susceptibility χ, and electric field E of the pump radiation can be written as

$$P(t) = \epsilon_o \chi E(t) \tag{2- 1}$$

This indicates that the material's polarization is proportional to the electric field. Beside the linear process, the nonlinear material also experiences nonlinear processes. These processes can be described by expanding χ in powers of the field E as illustrated by Eq. (2-2).

$$P(t) = P^{(1)} + P^{(2)} + P^{(3)} + \cdots = \epsilon_o(\chi^{(1)}E + \chi^{(2)}EE + \chi^{(3)}EEE + ..) \tag{2- 2}$$

where $\chi^{(2)}$ and $\chi^{(3)}$ are the second- and third-order nonlinear susceptibilities, respectively. The time-varying polarization $P(t)$ acts as a source of new components of electromagnetic fields. The associated wave equation governing electromagnetic radiation propagation in the nonlinear optical medium is of the form

$$\nabla^2 E - \frac{n}{c^2}\frac{\partial^2 E}{\partial^2 t} = \frac{1}{c^2 \epsilon_o}\frac{\partial^2 P_{nl}}{\partial^2 t} \tag{2- 3}$$

where n is the linear refractive index of the material.

The second term of the expansion of Eq. 2-2, yields the second-order nonlinear optical process, which is expressed as

$$P_{nl}^{(2)} = \epsilon_o \chi^{(2)} EE \tag{2- 4}$$

2.1.1 Second-order nonlinear phenomena

Suppose an optical field $E(t)$ consisting of two oscillating frequencies, ω_1 and ω_2 is incident on a nonlinear material. This optical field can be expressed as

$$E(t) = E_1 e^{-i\omega_1 t} + E_2 e^{-i\,\omega_2 t} + c.c. \tag{2- 5}$$

On substituting Eq. (2-5) onto (2-4), the expression becomes

$$P_{nl}^{(2)}(t) = \epsilon_o \chi^{(2)} E^2(t) = 2\epsilon_o \chi^{(2)}[E_1 E_1^* + E_2 E_2^*] + \epsilon_o \chi^{(2)}[E_1^2 e^{-2i\omega_1 t} + E_2^2 e^{-2i\omega_2 t} + 2E_1 E_2 e^{-i(\omega_1+\omega_2)t} + 2E_1 E_2^* e^{-i(\omega_1-\omega_2)t} + c.c.) \tag{2- 6}$$

Eq. (2-6) consists of several frequency components of the nonlinear polarization, which can be expressed as [44],

$$
\begin{aligned}
P_{nl}^{(2)}(2\omega_1) &= \epsilon_0 \chi^{(2)} E_1^2 e^{-2i\omega_1 t} && \text{(SHG)},\\
P_{nl}^{(2)}(2\omega_2) &= \epsilon_0 \chi^{(2)} E_2^2 e^{-2i\omega_2 t} && \text{(SHG)},\\
P_{nl}^{(2)}(\omega_1+\omega_2) &= 2\epsilon_0 \chi^{(2)} E_1 E_2 e^{-i(\omega_1+\omega_2)t} && \text{(SFG)},\\
P_{nl}^{(2)}(\omega_1-\omega_2) &= 2\epsilon_0 \chi^{(2)} E_1 E_2^* e^{-i(\omega_1-\omega_2)t} && \text{(DFG)},\\
P_{nl}^{(2)}(0) &= 2\epsilon_0 \chi^{(2)} [E_1 E_1^* + E_2 E_2^*] && \text{(OR)}
\end{aligned}
\qquad (2\text{-}7)
$$

According to Eqs. 2-7, the second-order nonlinear polarization has four distinct, nonzero frequency components. These include the frequency upconversion processes such as second harmonic generation (SHG) and sum frequency generation (SFG), the frequency downconversion processes such as difference frequency generation (DFG), and lastly, the optical rectification (OR) which produces a frequency independent steady state polarization. The optical rectification is responsible for terahertz pulse generation in nonlinear media.

2.2 Optical rectification

Optical rectification (OR) was the first process used to generate electromagnetic (microwave) pulses from picosecond laser pulses. Indeed, in 1962, Bass *et al*. [45] demonstrated the first DC optical rectification using 694 nm continuous wave (CW) in potassium dihydrogen phosphate and potassium deuterium phosphate. Yang *et al*. [46] in 1971 demonstrated broadband (0.06-0.36 THz) THz-pulse generation in lithium niobate pumped by Nd:glass laser. In 1984, Auston *et al*. demonstrated a high-bandwidth capabilities of optical rectification by generating THz pulses with frequencies up to 4 THz in lithium tantalate by Cherenkov cone radiation utilizing ultrafast laser pulses [47].

Optical rectification, also known as the nonlinear optical effect, is a second-order nonlinear optical process based on the difference-frequency generation of the spectral components of femtosecond laser pulses. When an intense laser beam pass through a nonlinear medium, it undergoes optical rectification, resulting in the production of a DC or low frequency polarization. The nonlinear polarization that results from optical rectification can be described as follows [48];

$$P_{nl}^{(2)}(\Omega_{THz}) = \epsilon_o \chi^{(2)} \int E(\omega + \Omega) E^*(\omega) d\omega \quad (2\text{- }8)$$

where ϵ_o is the vacuum permittivity, ω is the pump frequency, and Ω is the THz frequency, E is the Fourier component of the pump pulse, E^* is the complex conjugate of the electric field.

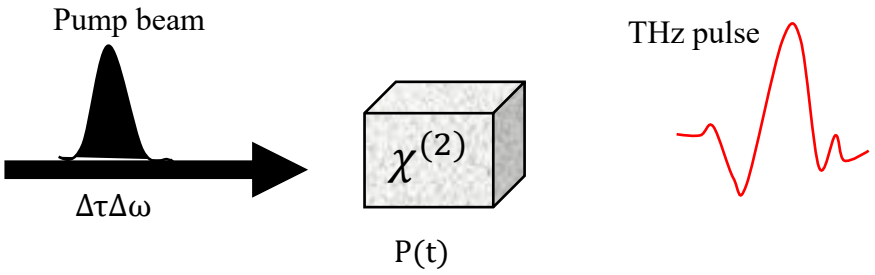

Figure 2-1: Optical rectification process in a nonlinear medium.

The femtosecond pump pulses induces a transient polarization, P(t), which in turn emits a THz-bandwidth pulse, as shown in Fig. 2-1. The second time derivative of the transient polarization determines the time evolution of the THz pulse. This is expressed as [25];

$$E_{THz} \propto \frac{d^2 \mathrm{P(t)}}{dt^2} \quad (2\text{- }9)$$

$\Delta\tau$ is the pulse width and $\Delta\omega$ is the bandwidth.

OR occurs in non-centrosymmetric crystals. It can also occur in centrosymmetric crystals only if a strong electric field is applied to break the symmetry. Optical rectification is dependent on the effective nonlinear coefficient (d_{eff}) and figure of merit (FOM) of the nonlinear material [49]. Several non-centrosymmetric crystals with high FOMs and d_{eff} have been investigated to generate THz pulses by optical rectification [49], ferroelectric materials such as lithium niobate ($LiNbO_3$), lithium tantalate ($LiTaO_3$), organic crystals such as DAST, DSTMS, HMQ-TMS and OH1, and semiconductors crystals like ZnTe, GaP, GaAs, ZnSe, CdTe, etc. Furthermore, by satisfying the phase-matching criteria in nonlinear materials, the efficiency of THz pulse generation by optical rectification can be increased, resulting in the generation of high energy and field strength terahertz pulses with a narrower spectral bandwidth [50]. The THz generation efficiency (η_{THz}) in the case of optical rectification, is highly dependent on the intensity of the pump (I_{pump}), and the square of crystal length (L). This is expressed as Eq. (2-10), in the case of velocity matching an no dispersion [51].

$$\eta_{THz} = \frac{2\Omega^2 d_{eff}^2}{\epsilon_o c^3 n_{IR}^2 n_{THz}} L^2 I_{pump}. exp[-\alpha_{THz}/2] \frac{sinc^2\left(\frac{\alpha_{THz} l}{2}\right)}{[\alpha_{THz} l/4]^2} \quad (2\text{- }10)$$

where n_{IR} is the optical refractive index and n_{THz} is the THz refractive index. According to Eq. (2-10), the THz generation efficiency (η_{THz}) scales with the square of the nonlinear coefficient (d_{eff}^2), and square of THz angular frequency (Ω^2).

During THz pulse generation by OR in nonlinear crystals, it is necessary to take into account the multiphoton absorption process [52] and the effects of nonlinear interactions (such as self-phase modulation, second-and third harmonic generation) between the optical and THz fields as they affect the generation efficiency [53]. The following sections discusses the theoretical aspects of phase matching techniques, multiphoton absorption process and nonlinear refractive effects.

2.3 Phase-matching techniques

To achieve phase matching condition, the phase velocity of the generated terahertz pulses must match the optical group velocity of the femtosecond laser pulses. The phase matching requirement assures that the generated THz pulses are in phase with the optical pulses. A phase mismatch causes destructive interference of the THz pulses generated, thus, resulting to low THz generation efficiency. The phase matching conditions can be achieved by; (i) collinear phase-matching in optically isotropic crystals in particular pump wavelengths and THz frequencies, such as zinc blende crystals like GaP, ZnTe, GaAs etc. (ii) noncollinear phase-matching (TPFP) in anisotropic crystals, such as ferroelectric materials like $LiNbO_3$ and $LiTaO_3$ by angle tuning (TPFP) (iii) birefringence of the nonlinear material, like GaSe and ZGP and iv) Quasi-phase matching e.g., periodically poled lithium niobate (PPLN). Here, only the collinear and noncollinear techniques of achieving phase matching are discussed.

2.3.1 Collinear phase-matching

For collinear phase-matching geometry, a case in which the generated THz waves propagate in the same direction as the pump beam. This can be achieved by selecting an appropriate phase-matching wavelength or frequency. Collinear phase-matching results in not only on long interaction lengths but also in generation of THz pulses with excellent beam quality. It's given by [54]

$$n_{THz}^{ph} = n_{opt}^{gr} \tag{2- 11}$$

In terms of velocity Eq. (2-11) can be expressed as $v(\Omega) = v_{gr}(\omega)$, where $n_{opt}^{gr} = c/v_{gr}$ is the group index and v_{gr} is the group velocity. For semiconductors, such as zincblende (GaP, GaAs, ZnTe, etc.), because of their small nonlinear coefficient and small PFT angles, collinear phase-matching is possible. F**Hiba! A hivatkozási forrás nem található.**igure 2-2 shows the optical group refractive and THz indices of ZnTe, collinearly phase-matched at 0.8 μm. Similar trend is expected in other zincblende semiconductors.

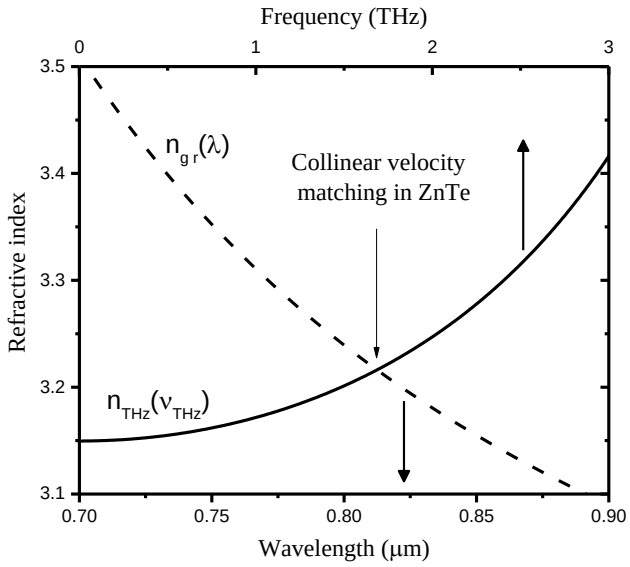

Figure 2- 2: Optical group indices and THz indices of ZnTe collinearly phase-matched [2].

2.3.2 Noncollinear phase-matching

A collinear phase-matching condition is impossible in some nonlinear materials, such as ferroelectric crystals ($LiNbO_3$ and $LiTaO_3$), and semiconductors pumped at long infrared wavelengths [19, 55, 56], since the THz refractive index n_{THz}^{ph} is larger than the group index n_{opt}^{gr} [57], the group velocity of the optical pulse is faster than the phase velocity of the generated THz pulses. Hence, there is mismatch which affects THz generation and yield. In this case, phase-matching conditions can only be fulfilled by tilting the pulse front using a dispersive element such as a grating or prism [58].Tilting the pulse front makes it possible to comply with the phase-matching condition for efficient THz generation. Figure 2-3 shows the general configuration considered when the THz pulses are generated at an angle (γ) with respect to the pump beam propagation

direction. The pump pulse propagate with a tilted intensity front inside the nonlinear medium. The THz pulses are generated.

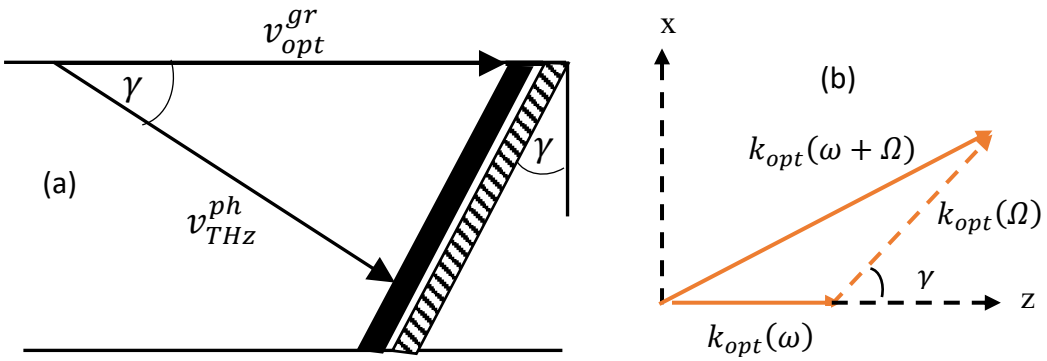

Figure 2-3: Noncollinear phase-matching scheme for pulse-front-tilted OR (a) and the wavevectors (b) [*58*].

Figure 2-3 illustrates that THz pulses generated by the tilted pulse front propagate perpendicular to the PFT angle (γ) of the pump pulse, satisfying the phase-matching criteria. This can be expressing as [58]

$$n_{THz}^{ph}\cos(\gamma) = n_{opt}^{gr} \tag{2- 12}$$

In terms of velocity Eq. (2-12) is expressed as $v_{opt}^{gr}\cos(\gamma) = v_{THz}^{ph}$. Figure (2-3b) show the description of TPFP in terms of wavevectors. Different frequencies ω and $\omega+\Omega$, propagate in the nonlinear medium in a different direction depending on the amount of angular dispersion introduced on the pump by the grating. The expression linking PFT angle (γ) of the excited THz pulses and the angular dispersion introduced by the dispersive element can be obtained as [59]

$$\tan(\gamma) = \frac{n_{opt}}{n_{opt}^{gr}}\omega\left(\frac{\partial\theta}{\partial\omega}\right)_{\omega_p} \tag{2- 13}$$

where $\left(\frac{\partial\theta}{\partial\omega}\right)_{\omega_p}$ is the angular dispersion introduced by the grating. The angular dispersion contributes to the group velocity dispersion (GVD)[60], which causes a chirp, broadens the pulse duration and reduces the tilt angle. The group velocity dispersion (GVD) is expressed as

$$\mathrm{GVD} = \frac{\mathrm{d}(\mathrm{v_{gr}^{-1}})}{\mathrm{d}\omega} = \frac{\omega}{\mathrm{c}}\left[\mathrm{n}\left(\frac{\partial\theta}{\partial\omega}\right)^2 - \frac{\partial^2\mathrm{n}}{\partial\omega^2}\right] \tag{2- 14}$$

where $\frac{\partial^2\mathrm{n}}{\partial\omega^2}$ is the square of material dispersion.

However, the use of dispersing element to tilt the pulse front results to the temporal broadening of the optical pulse due to dispersion. The resulting pulse duration becomes [61]

$$\tau(z) = \tau_o \sqrt{1 + \left(\frac{4 \ln 2 \, d^2\phi/d\omega^2}{\tau_o^2}\right)^2} \qquad (2\text{- }15)$$

Here, $\tau(z)$ is the pump pulse duration, τ_o is Fourier limited pump pulse duration, and $d^2\phi/d\omega^2$ is the group delay dispersion.

2.4 Coherence length

The coherence length l_c, which specifies the maximum thickness of the crystal that can be used to enhance THz generation and detection efficiency. It is defined as a function of the frequency as [62]:

$$l_c = \frac{\pi}{\Delta k} = \frac{c}{2v_{THz}|n_{THz} - n_{gr}|} \qquad (2\text{- }16)$$

The maximum coherence length occurs when the refractive index of THz radiation equals the group index of the laser pulses, according to Eq. 2-16, that is, in collinear phase-matching geometry case [63, 64]. To generate THz pulses efficiently from nonlinear crystals, the thickness of the THz generator crystal should be shorter than the interaction length in order to avoid conversion cancellation due to phase mismatch between the optical laser pulse and THz pulse. Furthermore, a long interaction of the laser pulse inside the crystal is essential for effective THz pulse generation. To prevent pulse distortion, the thickness of the electro-optic crystal should be much smaller than the coherence length [65]. Birefringence has been used to achieve long coherence lengths. However, the phase-matching bandwidth is quite limited because of the huge difference in refractive index between optical and THz beams. Long interaction lengths can also be achieved by tilting the pulse front [66]. Semiconductors have long effective THz generation length resulting from the smaller PFT angles [52]. Figure 2-4 shows plots of coherence lengths of some selected zincblende semiconductors as a function of optical pump wavelength.

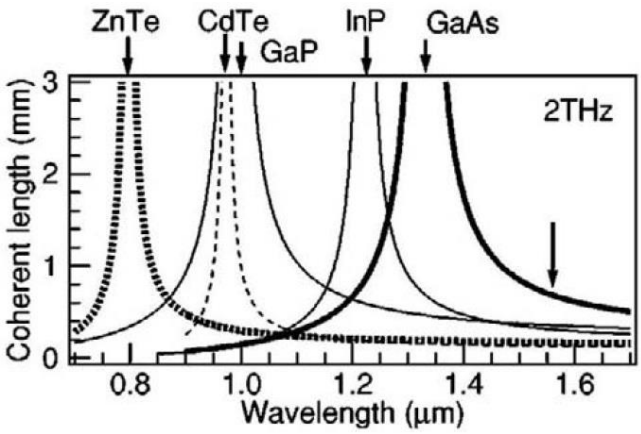

Figure 2-4:Coherence length as a function of optical wavelength for selected zincblende semiconductors at 2THz phase-matching frequency [*67*].

As illustrated in Fig. 2-4, ZnTe exhibits an enhancement in coherence length at 0.8 μm. As a result, ZnTe is the best electro-optic crystal for generating and detecting THz pulses utilizing a 0.8 μm pump laser system [67]. Also, other selected semiconductors, such as CdTe, GaP, InP, and GaAs, are collinearly phase-matched at 0.97 μm, 1 μm, 1.22 μm, and 1.33 μm, respectively, at 2 THz phase matching frequency as shown in Figure 2-4.

2.5 Multiphoton absorption

Linear electronic absorption can occur in dielectric materials or semiconductors only if the photon energy is greater than the band gap energy. However, bridging that bandgap at high optical intensity is possible by simultaneous absorption of two or more lower energy photons, where the sum of the photon energies exceeds the bandgap energy. Such nonlinear absorption processes are called multiphoton absorption (MPA) and constitute losses, thus limiting the efficiency of nonlinear optical materials. The simplest MPA is the two-photon absorption.

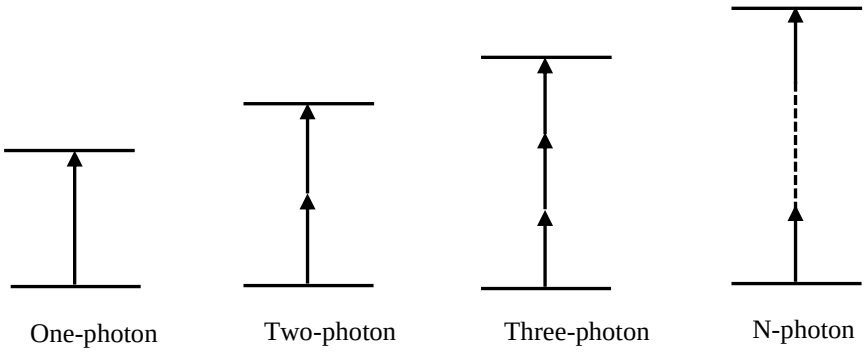

Figure 2-5: Several examples of multiphoton absorption processes.

In semiconductor materials, multiphoton absorption plays a critical role in determining the pump intensity to be used in the generation of THz pulses due to nonlinear absorption at higher intensities. The stronger the photon absorption, the lower the useful pump intensity. The multiphoton absorption (MPA) coefficients are determined by open z-scan measurements. For a given wavelength only one type of MPA dominates. Considering MPA of the order N, the optical intensity, $I(r,t,z_c)$ along the propagation direction z is described by the following coupled nonlinear equations

$$\frac{d}{dz}I(r,t,z_c) = -\beta_n I^n - \alpha_{fc} n_{fc} I \qquad (2\text{-}17)$$

where r is transverse radial coordinate, t time, z_c is the propagation distance inside the crystals, β_n is an nth order multiphoton absorption (MPA) coefficient, α_{fc} is the free carrier absorption (FCA) cross section, and n_{fc} is the density of free carriers accumulated during the MPA process. The first term on the right side of Eq. 2-17 due to MPA is proportional to I^n, while the second term due to FCA is proportional to I^{n+1}. Consequently, the former will prevail at low peak intensities, and if FCA is neglected, one can write Eq. 2-17 as

$$\frac{d}{dz}I(r,t,z_c) = -\beta_n I^n \qquad (2\text{-}18)$$

The optical intensity $I(r,t,z_c)$ of the laser pulse inside the crystal is given by

$$I(r,t,z_c) = I_o \frac{w_o^2}{w^2(z_c)} e^{-4\ln(2)\frac{t^2}{\tau^2}} e^{-\frac{2r^2}{w^2(z_c)}} \qquad (2\text{-}19)$$

Here, I_o is the peak intensity inside the crystal, w_o is the beam waist, $w(z_c)$ is the beam radius intensity at 1/e^2 and τ is the pulse duration at FWHM. Figure 2-5 shows several multiphoton absorption processes. As we move from lowest to higher orders, the effect of photon absorption becomes negligible. In addition, higher order multiphoton absorptions are weaker and, consequently, more difficult to study since much larger intensities are needed than lowest order multiphoton absorption, which may lead to damaging of the crystals due to high intensities.

2.6 Free carrier absorption

Semiconductors have a small bandgap energy (E_g) that is less than twice the photon energy; as a result, when pumped in collinear geometry, saturation effects result due to the presence of strong low-order multiphoton absorption [19]. For instance, ZnTe has a bandgap of 2.26 eV at a pump wavelength of 0.8 μm (1.55 eV photon energy), hence

2PA is dominant. This results in increase in free carrier concentration since the photon absorption is proportional to the carrier densities.

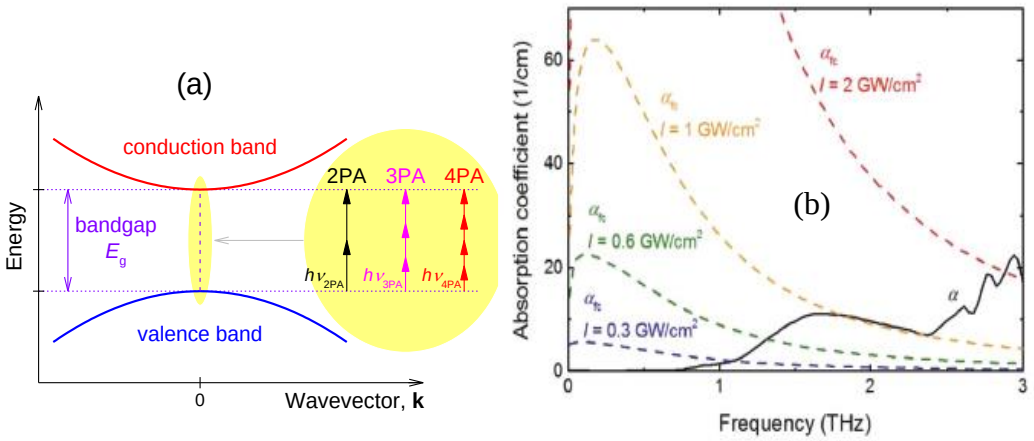

Figure 2-6: Photon absorption in direct-bandgap semiconductors [19], (b) linear absorption coefficient α and FCA coefficients α_{fc} in ZnTe at various pump intensities, as a function of THz frequency [68].

Consider a case of absorption over the bandgap in a semiconductor when the energy difference equals the energies of at least two photons, electrons are promoted from the valence band to the conduction band (Fig. 2-6a), while in these states, free carriers interact with incident radiation. Electrons in the conduction band further absorbs the incident radiation and move to a higher energetic state within the band. Similarly, the promoted holes in the heavy-hole band can be excited into a higher energy state. The free-carrier absorption is thus proportional to the carrier densities. The charge carrier densities depends nonlinearly on the incident intensities, while their generation rate depends on the order of multiphoton absorption involved. The increase in free-carrier concentration resulted in increase in absorption at the THz frequencies thus limiting the pump intensity for THz generation. In ZnTe, for instance, when pumped at 0.8 μm pump wavelength with a pulse duration of 100 fs, FCA owing to 2PA becomes comparable to the linear absorption at 1 THz, which is already below 1 GW/cm^2 pump intensity (Fig. 2-10b), restricting further increase in intensity. The free-carriers density (n_{fc}) generated by the incident pump pulse can be calculated from the Eq. 2-20 [69, 70].

$$n_{\mathrm{fc}} = \frac{I\tau}{hc/\lambda_o}\left(\alpha + \frac{1}{2}\beta_2 I + \frac{1}{3}\beta_3 I^2 + \frac{1}{4}\beta_4 I^3 + \cdots\right) \qquad (2\text{-}20)$$

where I is the pump intensity, τ is the pulse duration, h is the Planck's constant, $\lambda_o = 2\pi c/\omega_o$ is the pump central wavelength, α is the linear absorption, β_2, β_3, and β_4 are

the two-, three-, and four photon absorption coefficients, respectively. The FCA coefficient (α_{fc}), can be calculated from the Drude-model as

$$\alpha_{fc}(\Omega) = \frac{2\Omega}{c}\Im m\sqrt{\varepsilon_{\infty}.\left(1 - \frac{\omega_p^2}{\Omega^2 + i\Omega/\tau_{sc}}\right)} \quad (2\text{- }21)$$

where ε_{∞} is the high-frequency dielectric constant, $\omega_p^2 = e^2 n_{\text{fc}}/(\varepsilon_o \varepsilon_{\infty} m_{\text{eff}})$ is the plasma frequency, e is the electron charge, m_{eff} is the effective mass and τ_{sc} is the electron scattering time.

2.7 Intensity-dependent refractive index

The refractive index of many optical materials depends on the intensity of the light used to measure the refractive index. This can be described by the relation [44]

$$n = n_o + n_2 I \quad (2\text{- }22)$$

where n_o is the usual (i.e., linear, or low intensity) refractive index, and n_2 is an optical constant that characterizes the strength of the optical nonlinearity, it's given by [44]

$$n_2 = \frac{3}{4n_o^2 \varepsilon_o c}\chi^{(3)} \quad (2\text{- }23)$$

where $I = \frac{1}{2} n_o \varepsilon_o c E^2$ is the intensity of the incident wave and $\chi^{(3)}$ is the third order nonlinear susceptibility. The n_2 is measured in m^2/W. For any given material there is a maximum change in refractive index. This maximum change comes about either because of saturation effects or because there is a maximum laser intensity that can be used as a consequence of laser damage effects. Several processes occur as a result of the intensity dependent refractive index. This include self-focusing, self-phase modulation, among others. Self-focusing of light occurs when a beam of light having a nonuniform transverse intensity distribution propagates through a material for which n_2 is positive. The light beam induces a refractive index variation within the material with a larger refractive index at the centre of the beam that at its periphery, thus material itself acts as a lens, causing the beam to come to a focus within the material.

2.7.1 Self-phase modulation

Self-phase modulation is the change in the phase of an optical pulse resulting from the nonlinearity of the refractive index of the material medium. When short optical pulses propagate through a dispersive nonlinear optical media, the spectral content of the pulse can become modified by the nonlinear optical process of self-phase modulation. the

shape of the pulse can become modified by means of propagation effects such as dispersion of the group velocity within the medium. This process is especially important for very short optical pulses, which necessarily have a broad spectrum. In general, self-phase modulation and group-velocity dispersion occur simultaneously, and both tend to modify the shape of the optical pulse.

2.8 Diffraction grating

Gratings are classified into different ways, namely: amplitude and phase gratings, surface relief and volume phase gratings, master and replicated gratings, ruled or holographic gratings, and reflection and transmission gratings. The grating equation determines the diffraction properties of each grating type. Figure 2-7 shows the structure and the parameters that describe a grating profile.

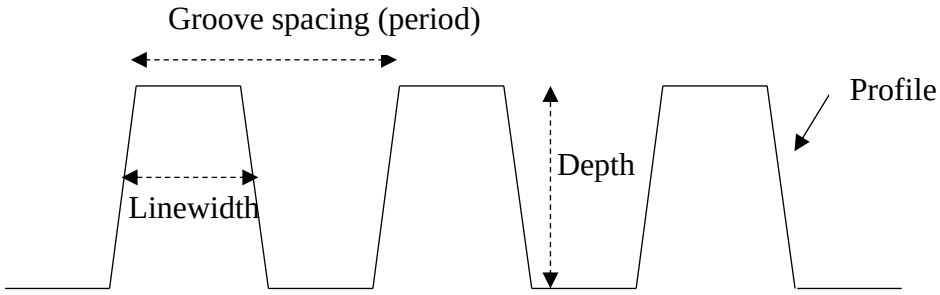

Figure 2-7: The grating structure showing the grating parameters.

- The groove spacing (period) is defined as the distance between the equally spaced grating grooves (or grating lines) as indicated in Fig. 2-7. The inverse of the groove spacing is the groove density or grating resolution, which is given as the number of grating lines per mm.
- The grating depth is the distance between the top of the grating and the bottom of the grooves. The duty cycle (filling factor) of the grating is defined as the line width divided by the groove spacing.
- The linewidth (ridge width) is the product of the duty cycle and the groove spacing or grating period.
- The grating profile is a general term for the shape of the grating grooves, which could be rectangular, sinusoidal, trapezoidal, or more complex, in each case being quantifiable by additional parameters.

2.9 Terahertz sources based on optical rectification

2.9.1 Organic crystals THz sources

The most widely used organic crystal for terahertz applications are the DAST [16, 71], DSTMS [17, 71, 72], OH1[71, 73] and HMQ-TMS [74]. Organic crystals have large effective nonlinear coefficients and high FOM compared to other nonlinear crystals [75]. They are collinearly phase-matched at laser wavelength range of 1.2–1.6 μm resulting in generation of collimated and aberration free THz beam that is suitable for achieving high field strengths due to good focusability of the THz beam [76]. They are suitable for generating terahertz pulses in the mid-infrared frequency range of 1-20 THz [71]. High field THz pulses with 0.9 mJ pulse energy has been reported to be generated from a 400 mm^2 partitioned DSTMS crystal by optical rectification of a 30 mJ Cr:Mg_2SiO_4 laser pulse centered at 1.25 μm pump wavelength [17]. The THz pulse had peak electric field and magnetic field of 42 MV/cm and 14 T, respectively, with a spectral range of 0.1-5 THz. An optical-to-THz conversion of over 3% was achieved. Rovere *et al.* reported generation of terahertz pulses in an organic crystal (HMQ-TMS) with electric field greater than 200 kV/cm, and a conversion energy efficiency of 0.26% collinear pumped by ytterbium laser with an optical pump energy of 420 μJ, pulse duration of 170 fs and central wavelength of 1030nm [74]. Generation of THz pulses with a conversion efficiency of 6% has been demonstrated in DAST at collinear geometry pumped with high power mid-IR optical parametric chirped pulse amplifier (OPCPA) generating 30 mJ pulse energy at a repetition rate of 20 Hz, 100 fs pulses centred at 3.9 μm [16]. However, scaling up the energies in organic materials is difficult due to the presence of strong phonon absorption at low frequencies [76], availability in small crystal sizes [17], and a relatively low damage threshold [25]. Nevertheless, collinearly phase matching wavelength of organic crystals lies in the range 1.2–1.6 μm which requires coupling of an optical parametric amplifier (OPA) to the femtosecond laser system. since OPAs have low optical-to-optical conversion efficiency, this lowers the usable pump fluence [71, 76].

2.9.2 Lithium niobate THz source

Lithium niobate is one of the most commonly used nonlinear crystals for the generation of intense THz pulses by optical rectification owing to its high figure of merit (18.2 pm^2cm^2/V^2), high effective nonlinear coefficient (168 pm/V) and large bandgap (3.8 eV). It's also pumped by common pump lasers with central wavelengths of 800 nm and

1030nm. Yang *et al*. demonstrated the generation of THz pulses in lithium niobate for the first time in 1971, where the crystal was pumped by Nd:glass laser [46]. However, due to a lack of phase matching, efficiency was low. The tilted pulse front pumping (TPFP) technique, as shown in Fig. 2-7 [58], was invented to improve the efficiency. Since the invention of the TPFP technique, optical rectification combined with the tilted pulse front technique in lithium niobate crystals for phase-matched terahertz generation has been demonstrated. For instance, with the TPFP technique, terahertz pulses with 10 μJ [77] and 57 μJ [78] and a conversion efficiency of 5 x 10^{-4} [78] have been reported. Xu *et al*. has demonstrated generation of 0.2 mJ THz pulses with a conversion efficiency of 0.3% at room temperature employing TPFP technique pumped by 0.8 μm Ti:Sapphire laser with a pulse duration of 50fs [79]. Additionally, by increasing the pump fluence to 186 mJ/cm^2 utilizing laser pulses with a pulse duration of 785 fs, it was shown that THz pulses with more than 0.4 mJ energy and 0.77% efficiency were generated even at room temperature [24]. A conversion efficiency of 3.8% has been achieved with 0.68 ps pulses centered at 1.03 μm pump wavelength by cryogenically cooling the crystal with 1.2 mJ pump energy [15]. So far, the highest reported THz pulse energy in the low-frequency range is 1.4 mJ, with a peak electric field as high as 6.3 MVcm^{-1} [14]

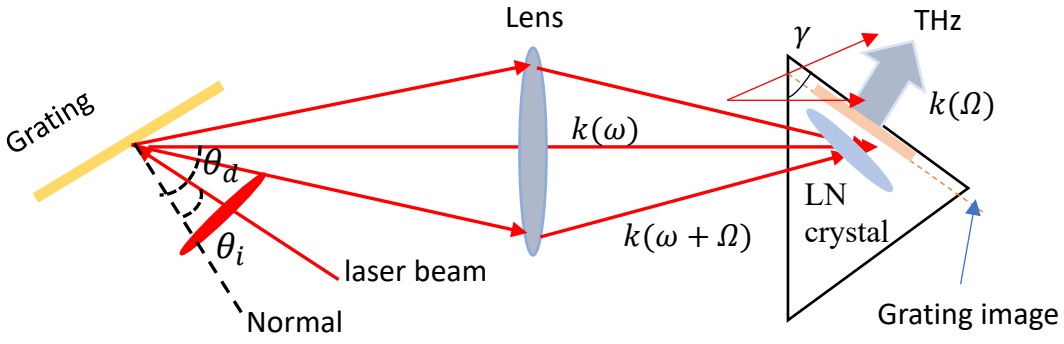

Figure 2-8: Implementation of TPFP technique using a grating and imaging system [*58*].

Use of the conventional pulse-front-tilt setups consisting of a diffraction grating and imaging optics (such as a lens or a telescope) as shown in Fig. 2-8, where θ_i is the incident angle and θ_d is the diffracted angle, can lead to distortion of the pump beam and THz beam due to imaging errors thus reducing the THz yield [80]. PFT angle is connected to angular dispersion and group velocity dispersion (GVD), as mentioned in section 2.4.2; since a large PFT angle is needed to achieve phase matching in lithium

niobate, this corresponds to a large GVD which causes broadening of the pulse duration within the crystal and, consequently, reduces the pump intensity [81], since intensity is inversely proportional to the pulse duration. In addition, tilting the pump laser pulse front in order to generate terahertz pulses makes it more challenging to focus the generated terahertz because the shape of the intensity profile is distorted [82]. Several techniques to improve the TPFP technique have been proposed and demonstrated: this includes: the use of contact grating (CG) for tilting the pulse front [83], which is image free and distortionless. With the CG scheme, THz pulses with 0.41 μJ and conversion efficiency of 1.5×10^{-4} have been demonstrated in lithium niobate using 2.7 mJ pump energy [84]. However, implementation of the CG technique in LN is challenging due to the large PFT angle needed for phase matching. Another technique proposed to improve TPFP is the use of a hybrid CG scheme which combines the conventional TPFP setup with imaging optics [85], but it is challenging to implement practically due to nonuniform pump propagation length, which results in varying interaction lengths affecting the focusability of the THz beam hence limiting achievable field strength. In addition, the use of plane-parallel LN with an echelon structure on the input surface for PFT has been proposed [86] and successfully implemented [87]. THz pulses with 1 μJ energy and conversion efficiency of 5×10^{-4} have been demonstrated [87]. Due to the uniform interaction length between the pump and THz beams, this technique enables scaling of the THz pulse energies and field strength by increasing the pump spot size and energy.

2.9.3 Semiconductor THz sources

Semiconductor nonlinear materials have recently been used for THz generation. They are characterized by (i) small pulse-front-tilt angles ($< 30^{o}$) (Fig. 2-10). The small PFT angles have various advantages, including a small crystal length variation throughout the pumped area that minimizes spatial nonuniformity in THz generating processes, smaller angular dispersion and less fluctuation in pump pulse duration with propagation distance, allowing for a longer effective interaction length, compensating for the smaller nonlinear coefficient; (ii) small effective nonlinear coefficients and electro-optic coefficients [75], as indicated in Table 2-1; (iii) small absorption than lithium niobate and organic crystals in the THz range [88]. The small absorption can help compensate the small nonlinear coefficient [68]; (iv) wide bandwidth range e.g., up to 7 THz for GaP [57, 87]; (v) broad transmission range [89]); (vi) optically isotropic with

collinear phase matching fulfilled at a specific pump wavelength [67]. For example, CdTe, GaP, and InP are collinearly phase-matched at 0.97 μm, 1 μm and 1.22 μm pump wavelengths, respectively, at 2THz phase matching frequency.

When group III element atoms of the periodic table combine with the group V element atoms, III-V semiconducting compounds are formed. They crystallize into the cubic zincblende structure with a $\bar{4}3m$ point group symmetry. The zinc blende crystals are characterized by a single lattice constant. Crystals with this structure include ZnTe, GaAs, GaP, ZnSe, InP, e.t.c. In GaP and GaAs, each atom is in the centre of a regular tetrahedron, with atoms of the other kind at each of its four corners, as shown in Fig. 2-9. Gallium phosphide is a broadband isotropic zincblende semiconductor material (spectrum range to 7 THz [90]), with a relatively large (direct) bandgap of 2.79 eV and indirect bandgap of 2.27eV [91], a nonlinear coefficient, $d_{eff} = 24.8\ \mathrm{pm/V}$, available in large sizes, has a wide transparency range [91], and has a relatively small absorption and dispersion in the THz range [20]. GaP has its transverse optical phonon resonances near 11 THz [92], thus making it suitable for THz pulse generation with broad bandwidth. GaP is the commonly used semiconductor material for optical rectification as it's collinearly phase-matched and avoids direct strong two-photon absorption [69]. Figure 2-9(a) shows the structure of gallium phosphide unit cell. GaAs is another isotropic cubic zincblende semiconductor crystal with a class symmetry of $\bar{4}3$. Figure 2-9(b) shows the structure of gallium arsenide unit cubic cell. It has a direct bandgap of 1.43 eV, a refractive index of about 3.6 in the optical region, a large nonlinear coefficient, $d_{eff} = 65.6\ \mathrm{pm/V}$ at the infrared wavelength [89], and a broad transmission range from 0.97 to 17μm [89] and has a transverse optical phonon resonances at 8.06 THz. GaAs has a low THz absorption coefficient of ~1 $\mathrm{cm^{-1}}$at 1-2 THz frequencies at room temperature [55]. Table 2-1 shows a summary of properties of some selected crystals used for THz pulse generation via optical rectification.

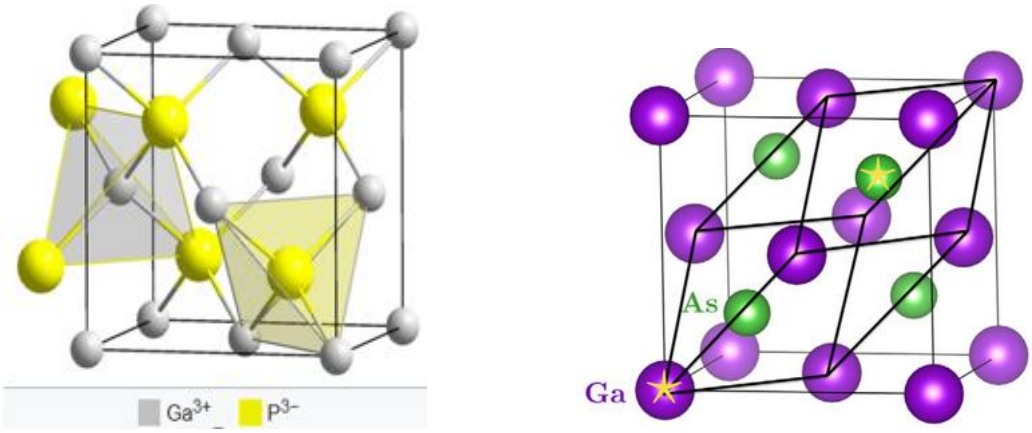

Figure 2- 9: The cubic unit cell structure for (a) gallium phosphide [93] and (b) gallium arsenide [94].

Table 2 1: Properties of materials suitable for THz generation via OR [75]

Material	$d_{eff}\left(\frac{pm}{V}\right)$	$\frac{r_{ijk}}{\left(\frac{pm}{V}\right)}$	n_{800nm}^{gr}	n_{THz}	$n_{1550\,nm}^{gr}$	α_{THz} cm^{-1}	FOM $\left(\frac{pm^2cm^2}{V^2}\right)$
CdTe	81.8	6.8	3.73	3.24	2.81	4.8	11.0
GaAs	65.6	1.6	4.18	3.59	3.56	0.5	4.21
GaP	24.8	0.97	3.67	3.34	3.16	0.2	0.72
ZnTe	68.5	4.04	3.31	3.17	2.81	1.3	7.27
GaSe	20.8	1.7	3.13	3.27	2.82	0.5	1.18
sLN	168	30.3	2.25	4.96	2.18	17	18.2
DAST	615	47	3.39	2.58	2.25	50	41.5

ZnTe is the most common used nonlinear material by optical rectification owing to its high figure of merit (FOM) value and collinearly phase matched for Ti:Sapphire laser pumping wavelength of 0.8 μm [66]. Similarly, GaP and GaAs have been collinearly pumped at 1 μm and 1.56 μm [95, 96], respectively, for THz pulses generation. Unfortunately, semiconductors have a small bandgap energy (E_g) that is less than twice their photon energy; as a result, when semiconductors are pumped in collinear geometry, saturation effects result due to the presence of strong low-order multiphoton absorption [19], limiting the useful pump intensity and, thus, the terahertz energy. For instance, THz pulses with 1.5 μJ and a conversion efficiency of 3.1×10^{-5}, have been reported using a large-aperture ZnTe crystal pumped at collinear phase-matching geometry with a 48 mJ pump energy [97]. The low THz pulse energies and conversion efficiency are associated with strong 2PA. THz pulses with a conversion efficiency of 0.05% and spectral range from 0.1 to 3 THz have been generation via OR in GaAs

pumped at 1.8 μm (beyond the cut-off wavelength of 2PA) using a modified tilted-pulse-front scheme [55]. THz pulses with a broadband range of 0.3 to 7 THz have been demonstrated in GaP pumped by Ti:Sapphire laser [98]. Xu *et al*. has demonstrated THz pulse generation in GaP by optical rectification of 1 μm pulses with a pulse duration of 20 fs, a repetition 78 MHz and average power of 5.5 W [20]. Recently, GaP has been considered as a CG semiconductor THz sources for long wavelength pumping [99]. Experiments have demonstrated that the 3PA dominate the multiphoton absorption process when GaP is pumped at collinear geometry [100], while strong 2PA dominates in GaAs [101] pumped at collinear geometry. Due to the absence of strong 2PA in GaP, this feature enables it to be more favorable in scaling the efficiency and peak electric field even at higher frequencies than ZnTe and GaAs.

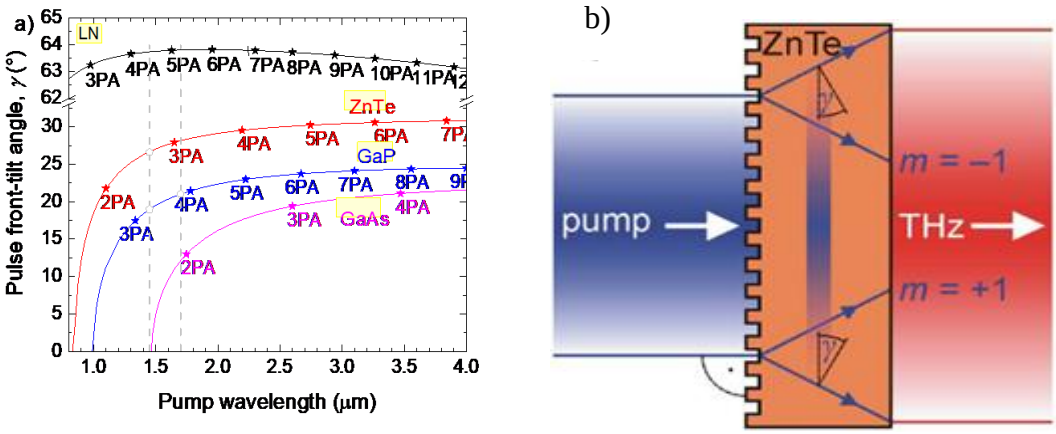

Figure 2-10: (a) Pulse front tilt angles against pump wavelengths [*19*],(b) Scheme of ZnTe CG THz source with collinear geometry [*56*].

Long infrared pump wavelengths have been proposed and applied to eliminate the strong low order multiphoton absorption [19, 21, 70, 102], enabling the use of high intensity, which results in high energy THz pulse generation. For instance, THz pulses with 0.6 μJ and a conversion efficiency of 5.4×10^{-4}, and a spectral range extending to 3 THz have been generated GaAs crystal, pumped at a wavelength of 1.8 μm, sufficiently long to suppress 2PA [55]. More recently, THz pulses with energies as high as 14 μJ and conversion efficiency of 0.7% have been reported in ZnTe pumped at 1.7 μm infrared pump wavelength [19]. At this wavelength, the 2PA and 3PA and associated free carrier absorption (FCA) have been suppressed since the cut-off wavelength of 3PA is 1.65 μm. However, phase matching conditions are no longer met at long pump wavelengths; hence, tilting the pulse-front is required to fulfill the phase

matching conditions for efficient terahertz generation. The contact grating (CG) technique offers the possibility of achieving phase matching conditions owing to their small PFT angles (Fig. 2-10a). The CG technique has been applied successfully in the ZnTe (Fig. 2-10b), where THz pulses with a peak energy of 3.9 μJ, an electric field of 0.57 MV/cm, and optical-to-THz conversion efficiency of 0.3% have been reported [56]. This THz generating efficiency is two orders of magnitude higher than the previous highest value reported in ZnTe [97]. On the other hand, ZnTe exhibits saturation effects at high-intensity irradiation, due to strong low order multiphoton absorption, limiting its application [69]. Gallium phosphide (GaP) and gallium arsenide (GaAs) can be viable alternatives to ZnTe as they have comparable effective nonlinear coefficients, easy to grow to large sizes, and are less expensive. In addition, GaP has a broad tunable range up to 7 THz [90]. Figure 2-11 illustrates an overview of the achieved highest pulse energies and peak electric field strengths of various selected THz sources.

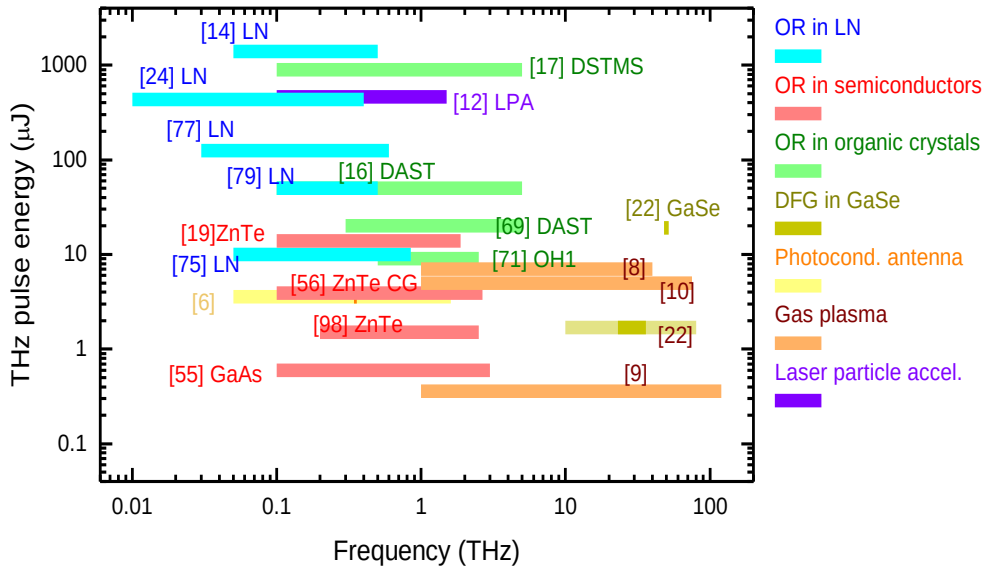

Figure 2- 11: Overview of some of the reported THz pulse energies [*68*].

2.10 Theoretical models of multiphoton absorption in semiconductors

The two- and three photon absorption processes in semiconductors have been studied extensively in both theoretically and experimentally. Scaling laws for multiphoton absorption coefficients in direct bandgap semiconductors have been developed based on a two-band model [103, 104]. A review of theoretical models and experimental values for two-photon (2PA) and three-photon (3PA) absorption coefficients for a few materials can be found in [104, 105]. However, data on 4PA and on higher order

multiphoton absorption coefficients are scarce and not available for some semiconductor materials. Two theories, namely, Keldysh and Wherrett can be used to estimate the higher order MPA coefficients, since in the past they were successfully used for prediction of 2PA [103, 105]. However, it is worth to mention here that only the coefficient values calculated with Keldysh theory will be presented.

2.10.1 Keldysh theory

The Keldysh theory is based on the perturbation theorem, a process in which an electron undergoes transition states. Electronic wave functions approximate this transition states to account for the acceleration of the electrons by an incident alternating current field. This electron transition is accompanied by simultaneous absorption of several quanta, an effect similar to the tunnelling effect of an electron passing through a barrier [105]. Higher-order multiphoton absorption coefficients can be estimated from the Keldysh tunnelling theory as well. In our calculation, we used the Keldysh expression for the multiphoton transition rate per unit volume, W [106].

$$W = \frac{2\omega}{9\pi N}\left(\frac{\mu^*\omega}{N\hbar}\right)^{\frac{3}{2}}\left(\frac{e^2E_o^2N^2}{16\mu^*\omega^2E_g}\right)^N \times exp\left[2\langle \tilde{E}g/\hbar\omega + 1\rangle\left(\frac{1-e^2E_o^2N^2}{4\mu^*\omega^2E_g}\right)\right] \times \Phi\left[\left(2\langle \tilde{E}g/\hbar\omega + 1\rangle - 2\tilde{E}g/\hbar\omega\right)^{1/2}\right] \quad (2\text{-}24)$$

where the notation $\langle \quad \rangle$ means the integer part of the argument and $\tilde{E}g$ is the effective band gap in the presence of the radiation, $\tilde{E}g = E_g\left(1+\frac{1}{2\gamma^2}\right)$, $\gamma \ll 1$ corresponds to quantum-mechanical tunnelling, μ^* is an electron effective mass, E_O is the electric field, E_g is the bandgap energy, $\hbar$ is the reduced Planck's constant, ω is the laser pump frequency, e is the electron charge, and Φ is the Dawson integral given by $\Phi(z) = \exp(-z^2)\int_0^z \exp(y^2)\,dy$.

The Keldysh parameter (γ) is given by

$$\gamma = \sqrt{\frac{2m\omega^2E_g}{e^2E^2}} \quad (2\text{-}25)$$

where m is the reduced effective electron-hole mass, and E is the electric field of the laser pulse inside the crystals.

Chapter Three

3.1 Motivation

Lithium niobate and organic crystals have large effective nonlinear coefficients and higher FOMs which are advantageous for generation of THz pulses by OR. However, there are challenges of scaling the THz pulse energies and field strengths, for example, in LN, nonlinear interaction between the pump and THz beam leads to beam distortions [107, 108], large PFT angle leads to limited interaction length for THz pulse generation due to large angular dispersion [81]. In addition, use of imaging optics in the case of conventional TPFP leads to imaging errors, which distorts the THz beam making it more difficult to focus [82]. Improvements in THz pulse generation in LN have been made [85, 86], but still challenges exist in implementation. On the other hand, organic materials have limitations as mentioned in section 2.6.1 in scaling THz pulse energies. Semiconductors pumped at long wavelengths [19, 70] have been considered viable. The CG based on TPFP setup was proposed to achieve a collinear THz generation scheme with which the extractable THz energy became scalable [83]. ZnTe CG has been designed [109] and implemented, where a conversion efficiency of 0.3% and THz pulse energy of 3.9 μJ has been reported. However, there were difficulties in the growth of ZnTe CG crystals due to microbubbles [56]. GaP and GaAs CG THz sources are promising alternatives as they are easier to grow and less expensive.

3.2 Scientific goals

The main aim of this work was to numerically investigate THz generation efficiency and design optimized, scalable and highly efficient semiconductor contact grating terahertz sources pumped at long infrared wavelength range. By numerical simulations, the basic design aspects of semiconductors ZnTe and GaP, as well as their optimal pumping and phase matching conditions at infrared wavelengths below 2 μm, have been determined [99].

- The first goal of the study was to extend by numerical calculations the determination of design aspects and the optimum pumping and phase matching conditions of GaAs and GaP pumped at long infrared wavelengths greater than 2 μm. The aim was to determine by numerical calculations the optimum pumping parameters such as pulse duration, pump intensity, crystal length, and phase-matching frequency that yield the highest terahertz conversion efficiency to give more insight into the semiconductor contact grating THz sources.

In addition, it has been predicted and demonstrated that the elimination of low order multiphoton absorption (MPA) processes by using long pump wavelength can result in a significant increase of THz generation efficiency [19, 21, 70, 102], due to the possibility of using higher pump intensities without increasing the density of free carriers and their absorption in the THz range.

- The second goal of the study was to numerically investigate the possibility of increasing terahertz generation efficiency in semiconductors by using longer pump wavelengths to suppress strong low order multiphoton absorption and determine the optimum long pump wavelength limit where the suppression of multiphoton absorption in semiconductors GaP and GaAs is beneficial. The aim was to determine by numerical calculations the extent to which the suppression of higher order multiphoton absorption has a significant benefit on the terahertz generation efficiency. Another aim was to investigate the effect of nonlinear refractive index on THz generation efficiency in semiconductors.

Scalable ZnTe CG THz source has been reported as mentioned in section 3.1. However, growing large size ZnTe crystals is difficult due to microbubbles [56].

- The third goal was to extend the design of the scalable and efficient semiconductor contact grating to other semiconductors GaP, and GaAs THz sources. I aimed to determine a set of design parameters (duty cycle and groove depth) by numerical calculations that yield the highest diffraction efficiencies based on rectangular and trapezoidal structures in GaP and GaAs contact gratings to give practical guidance for designing and fabrication of highly efficient THz pulse sources. Another aim was to investigate the effect of deviations from the perpendicular wall on diffraction efficiency.
- The fourth goal was to investigate the possible ways of increasing the diffraction efficiencies of the GaP and GaAs as high as possible, to even more than 90% at long infrared wavelengths. The aim was to enhance the diffraction efficiencies of the GaP and GaAs CG by adding antireflective (AR) coatings layers to the CG. Here, numerical investigations of three different ways of adding AR coatings were performed.

Chapter Four

4.0 Description of models and approaches

4.1 Theoretical model used for simulating the THz generation

Numerical calculations were performed to investigate the optimal pump parameters for efficient THz generation in gallium phosphide (GaP) and gallium arsenide (GaAs). The calculations were performed in the spectral domain by solving the one-dimensional wave equation with nonlinear polarization. The theoretical model was based on the Ravi *et al.* [53] model. The Ravi *et al.* model took into account cascading effects caused by up-and down-conversion, pump pulse length fluctuation with propagation distance due to dispersion, and THz absorption in the THz frequency range caused by a complex dielectric function. In contrast to the Ravi *et al*. model, which was used in the simulation of THz pulse generation in lithium niobate, which is a large bandgap dielectric material, the model we used considered the effects of free carriers generated in the semiconductors due to the high optical field intensity on the THz field. The instantaneous refractive index and absorption of the semiconductors at the THz frequency range were calculated according to the equations (4-1) and (4-2), respectively.

$$n_{THz}(\Omega, \mathrm{z}) = \Re e\left(\sqrt{\varepsilon_{r0}(\Omega) + \varepsilon_{fc}(\Omega, z)}\right) \tag{4- 1}$$

$$\alpha(\Omega, \mathrm{z}) = {}^{2\Omega}/_{c}\, \Im m\left(\sqrt{\varepsilon_{r0}(\Omega) + \varepsilon_{fc}(\Omega, z)}\right) \tag{4- 2}$$

where $\varepsilon_{r0}(\Omega)$ is the dielectric constant of the semiconductor without free carriers [110], $\varepsilon_{fc}(\Omega, z)$is the permittivity attributed to the free carriers. It is given by equation (4- *3*)

$$\varepsilon_{fc}(\Omega, z) = -\frac{q^2}{\varepsilon_0 m_{eff}} \frac{N_{wa}(z)}{\Omega^2 + i\,\Omega/\tau_{sc}} \tag{4- 3}$$

Here, q is the charge of the electron, ε_0 is the vacuum permittivity, m_{eff} is the effective mass of the electron, τ_{sc} is the electron scattering time, $N_{wa}(z)$ is the weighted average of the free carrier density at the z point in the crystal, which was determined according to Eqs. (4-4) and (4-5)

$$N_{wa}(z) = \frac{\int_{-\infty}^{\infty} A_{THz}^2(t, z) N_c(z, t)\mathrm{d}t}{\int_{-\infty}^{\infty} A_{THz}^2(t, z)\mathrm{d}t} \tag{4- 4}$$

$$N_c(z,t) = \frac{\beta_n}{nh\nu_0} \int_{-\infty}^{t} I_{op}^{n}(t',z)\mathrm{d}t', \quad (4\text{- }5)$$

where A_{THz}^2 represent the envelope of the THz field, β_n is the nth photon absorption coefficient, h is the Planck constant, ν_0 is the central pump frequency and $I_{op}(t,z)$ is the temporal intensity of the pump at the z point.

The pump wavelengths considered in the calculations of the THz generation efficiency were in the range 1- 5 μm for both GaAs and GaP. The lowest-order effective multiphoton absorption considered was 2PA and 3PA, in GaAs and GaP, respectively. The coefficients of photon absorptions used in the calculations were obtained as follows; 2PA and 3PA of GaAs from Ref. [111] and Ref. [101], respectively, 2PA and 3PA of GaP from Ref. [105], 4PA of GaP from Ref. [112]. The 4 to 6PA in GaAs and 5 to 7PA in GaP were estimated due to the absence of known coefficients for these materials in the wavelength ranges of interest. Sohn *et al*. had measured photon absorption up to the 11th order in GeSbS chalcogenide glass using a z-scan technique over a wavelength range of 1.1 μm to 5.5 μm [113]. It was revealed that the ratio of the neighboring constants follow an exponentially decreasing scale, where the ratio between the neighboring values is nearly constant (see Table 4-1). In order to validate the estimated multiphoton absorption coefficients, calculations were performed using the Keldysh photoionization model [106] . The Keldysh photoionization model predicted an almost constant ratio as well, as shown in Table 4-1. Based on this, the known constants of 2PA and 3PA for both GaAs and GaAs were used to have the ratio with which, the missing coefficient values in $\mathrm{cm}^{2n-3}/\mathrm{GW}^{n-1}$ units, where n is the order of multiphoton absorption, were estimated. Table 4-1 summarizes the multiphoton absorption coefficients at various orders used in the simulations of THz pulse generation.

4.2 Keldysh theoretical calculations

The Keldysh model assumes monochromatic laser spectrum. Calculations of the 2 to 5th -orders of MPA coefficients in GaAs and 2 to 7th -orders of MPA coefficients in GaP were performed using the Keldysh photoionization model [106]. A peak intensity of 50 GW/cm^2 was considered in the calculations, where the Keldysh parameter $\gamma \ll 1$, for both GaP and GaAs. In the calculations of γ, the coupling between the valence bands and their contributions to nonlinear absorption were neglected. By numerically

solving the Keldysh Eqs. given in [106] and using the effective masses of GaP and GaAs from Ref. [114], the MPA coefficients for the GaP and GaAs at various selected wavelengths were obtained. In the calculations, the wavelength for each order was chosen in a way that it corresponds to the center of the frequency range of the given order. In the case of GaP, 2-, 3-, 4-, 5-, 6-, and 7PA, corresponds to wavelengths 0.59-, 1.07-, 1.53-, 1.98-, 2.43- and 2.9 μm, respectively. For the GaAs, the 2-, 3-, 4-, 5-, and 6PA correspond to pump wavelengths 1.15-, 2.06-, 2.97-, 3.85- and 4.73 μm, respectively. For the GeSbS glass, the MPA order and corresponding pump wavelengths are given Ref. [113]. Figure 4-1 (a) illustrates a plot of the coefficients obtained from the Keldysh Eqs. for GaP and GaAs, whereas Fig. 4-1 (b) depicts a plot of absorption coefficients for GeSbS glass obtained from Ref. [113]. The coefficients were obtained in $\mathrm{cm}^{2n-3}/\mathrm{GW}^{n-1}$ units.

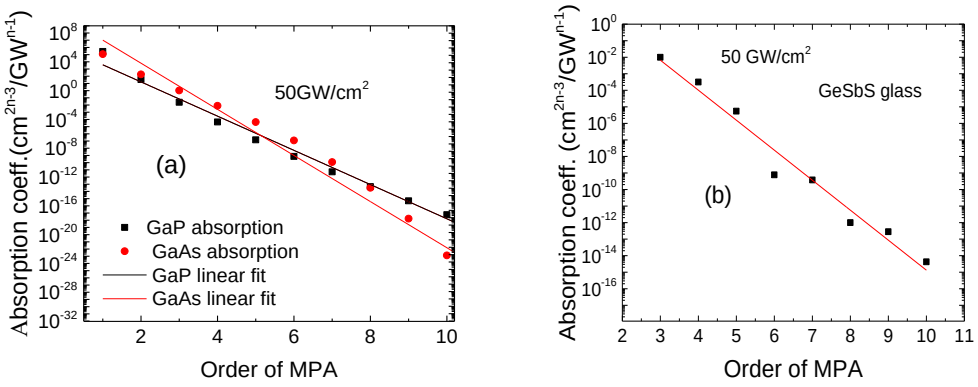

Figure 4-1: A plot of absorption coefficient against the order of MPA (a) GaAs and GaP, (b) GeSbS glass.

A comparison of the calculated photon absorption coefficients with the available experimental coefficients in the case of GaP and GaAs was made. The 2PA coefficients calculated using the Keldysh model were almost an order of magnitude higher than the known experimental coefficients for both GaP and GaAs. The calculated 3PA in the case of GaP was almost in agreement with the known experimental coefficient, whereas in the case of GaAs, it was 2.3 times higher than the experimental value. The ratios of the corresponding neighboring coefficients were calculated, and obtained a constant ratio between the corresponding coefficients, similar to the case of GeSbS glass (Fig. 4-1b) [113]. Moreover, no comparison was made with the theoretically calculated coefficients for the higher-order multiphoton absorptions due to a lack of known experimental coefficients. Table 4-1 summarizes the experimental, estimated

coefficient values obtained by comparing the neighbouring constants and the theoretical calculations based on the Keldysh model. It should be mentioned here that the referenced coefficients in the Table 4-1 were obtained experimentally, while estimated refers to the coefficient values predicted by comparing neighboring constants.

Table 4- 1: Multiphoton absorption (MPA) coefficients of GaP, GaAs and GeSbS.

MPA order	GaP		GaAs		GeSbS
	Estimated	Keldysh	Estimated	Keldysh	
2PA cm/GW	4[105]	34.6	26 [111]	184	-
3PA ($\times 10^{-2}\mathrm{cm}^3/\mathrm{GW}^2$)	4.2 [105]	4	35 [101]	82	0.87 [113]
4PA ($\times 10^{-4}\ \mathrm{cm}^5/\mathrm{GW}^3$)	4.4 [112]	4.4	4.7	78	1.1 [113]
5PA ($\times 10^{-6}\ \mathrm{cm}^7/\mathrm{GW}^4$)	4.6	1.46	6.4	43	1.78 [113]
6PA ($\times 10^{-8}\ \mathrm{cm}^9/\mathrm{GW}^5$)	4.8	4.64	86	32	2.38 [113]
7PA ($\times 10^{-10}\ \mathrm{cm}^{11}/\mathrm{GW}^6$)	5.0	-	-	-	3.82 [113]

4.3 Contact grating THz source scheme

The contact grating (CG) scheme relies on a grating structure formed on the entrance surface of a semiconductor nonlinear crystal for tilting the pulse front [83]. As shown in Figure 4-2 (a), the pump beam is incident normally to the grating surface. The incoming pump beam is diffracted at the grating surface. At normal incidence, the diffraction introduces a pulse front tilt (PFT) angle (γ), equal to the diffraction angle (β) (see Fig. 4-2a). The pump beam then propagates within the crystal with the pulse front tilt angle (γ), suitable for velocity-matched THz pulse generation.

The two symmetrical diffracted orders (±1st) fulfil the velocity matching conditions. In this case, the two diffracted beams superpose each other, and the tilted pump pulse fronts are on opposite side of each other and are parallel to the grating front. This superpositioned pump pulse front generates the THz pulses, which propagate collinearly with the pump beam at a distance equal to $L/\cos\gamma$, where L is the crystal length.

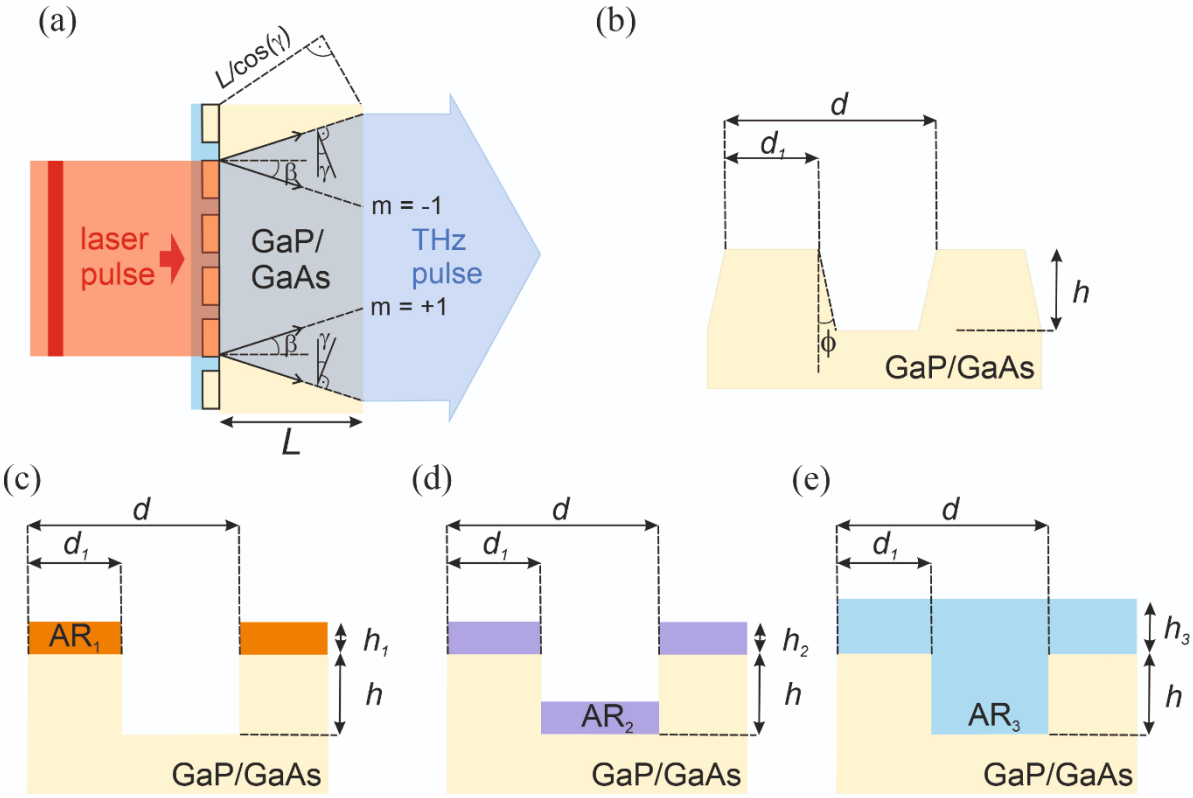

Figure 4-2: (a) Contact-grating schemes for GaP and GaAs (b) Cross-section of a trapezoidal structure with ϕ-wall angle, (c), (d) and (e) Rectangular structures with anti-reflecting (AR) coatings of $n_{AR_1} = n_{SiO_2}$, $n_{AR_2} = \sqrt{n_{GaP/GaAs}}$, and a Norland optical adhesive 170 (NOA), respectively; d-groove spacing, d_1-ridge width h - groove depth, h_1 - AR_1 thickness, h_2- AR$_2$ thickness, h_3 - AR_3 thickness, $n_{GaP/GaAs}$- refractive index of GaP/GaAs, and L - crystal length.

4.4 Contact grating design parameters

The contact grating design parameters for selected wavelengths were determined as follows: The optical and group refractive indices were calculated from Sellmeier equations obtained from Ref. [115] and from Ref. [91] for GaAs and GaP, respectively, whilst the THz indices for GaP and GaAs were calculated from equations obtained in Ref. [116] and Ref. [117], respectively. The Sellmeier Eqs. were:

$$\mathrm{n}^2(\lambda) = 3.5 + \frac{7.4969\lambda^2}{\lambda^2 - 0.4082^2} + \frac{1.9347\lambda^2}{\lambda^2 - 37.17^2} \tag{4- 6}$$

$$n^2(\lambda) = 1 + \frac{1.39\lambda^2}{\lambda^2 - 0.172^2} + \frac{4.131\lambda^2}{\lambda^2 - 0.234^2} + \frac{2.57\lambda^2}{\lambda^2 - 0.345^2} + \frac{2.056\lambda^2}{\lambda^2 - 27.52^2} \tag{4- 7}$$

The pulse-front tilt angles (γ) were calculated from the velocity matching Eq. given by [58]

$$\cos(\gamma) = \frac{n_g}{n_{THz}} \tag{4- 8}$$

where $n_g = n_p - \lambda_p \left. dn_p \right/ d\lambda_p$ is the group index, n_p, λ_p, and n_{THz} are the optical refractive index, pump wavelength and THz index, respectively. The diffraction angle

(β) was determined by the n_p (phase) index of the GaP or GaAs at the pump wavelength and by the d grating groove spacing according to the grating Eq. given by Eq. 4-9 [109]

$$n_p \sin(\beta_m) = m\lambda_p/d \quad (4\text{-}9)$$

where m = ±1, ±2… is the diffraction order.

The groove spacing d for a given wavelength was carefully chosen so that the diffraction angle (β) for the $\pm$1st order equals the γ angle needed for velocity matching. In the diffraction orders, there were $\pm$1st and $\pm 2^{nd}$ beside the 0^{th} orders in both GaAs and GaP. However, for the calculation of diffraction efficiency, only the sum of the $\pm$1st diffraction orders were considered since they fulfilled the velocity matching condition, thus, yielding the highest diffraction efficiency. Table 4-2 shows some of the gallium phosphide and gallium arsenide materials' optical properties at some selected wavelengths.

Table 4-2: PFT angle(γ), optical refractive index (n_p), group index (n_g), and multiphoton absorption (MPA) at 2 THz phase matching frequency.

GaP					GaAs				
λ_p (μm)	γ=β (°)	n_p	n_g	MPA	λ_p (μm)	γ=β (°)	n_p	n_g	MPA
1.03	7.81	3.11	3.32	3	2.06	17.38	3.36	3.46	3
2.06	22.88	3.036	3.086	5	3.00	20.98	3.33	3.38	4
3.00	24.36	3.02	3.05	6	3.90	22.04	3.32	3.36	5
3.90	24.78	3.014	3.041	8					

To minimize Fresnel losses and enhance the diffraction efficiency on the contact gratings, a numerical investigation of the effect of adding three different types of antireflection coatings (ARCs) on the contact grating (CG) surface, namely: adding SiO_2, adding a material with a refractive index equal to the square root of the refractive index of the CG (GaP or GaAs), and adding Norland optical adhesive (NOA) 170 was performed. Figure 4-2(c) illustrate adding of SiO_2 coating thickness on the CG. The AR thickness can be added into 8 steps based on contact photolithography technique. Moreover, after processing SiO_2 AR layer can only be found on the upper surface of the CG profile. More details of the fabrication process using the photolithography method can be found in Figure 1 of Ref. [118]. Figure 4-2(d) illustrates adding a material with a refractive index equal to the square root of the refractive index of the

CG (GaP or GaAs), where an evaporation technique can be used to add the AR coating and Figure 4.2(e) shows adding Norland optical adhesive 170 (NOA). This can be done by overfilling the grooves with NOA, followed by UV curing, and polishing the NOA to the required thickness. The starting antireflective coatings' layer thickness h_1, h_2 and h_3 were calculated from the Eq. given by

$$h_1 = h_2 = h_3 = \frac{\lambda_p}{4n_c} \tag{4- 10}$$

where n_c is the refractive index of the AR coating material. The ARCs thicknesses were scanned around these starting values.

4.5 Contact grating profiles

The parameters that define the diffraction efficiency are the groove spacing (d), groove depth (h), and duty cycle f, (f=d_1/d, Fig. 4-2). A set of these parameters, which give maximum diffraction efficiency, were determined from numerical calculations. The calculations were carried out using Gsolver (Grating Solver development company) version 5.1 and COMSOL Multiphysics version 5.4 softwares. The GSolver software is based on rigorous coupled wave equations [119], whilst COMSOL Multiphysics software is based on numerical solutions of partial differential equations utilizing finite element methods [120]. Diffraction efficiencies were calculated for the rectangular and trapezoidal grating profiles at the pump wavelength range of 2 to 4 μm. In all calculation, we considered the case where the pump beam was incident perpendicular to the grating surface, as shown in Fig. 4-2. The choice of pump wavelengths was particularly interesting as it enabled the elimination of strong lowest-order multiphoton absorption, allowing the use of higher pump intensities and was also based on the available pump sources for experimental demonstrations. Transverse electric field (TE) and transverse magnetic field (TM) polarization states were studied for the rectangular and trapezoidal grating profiles.

Chapter Five

5.0 Results and discussion

5.1 Numerical investigation of THz generation efficiency

To investigate the effect of multiphoton absorption on the terahertz generation efficiency, numerical simulations of terahertz generation in GaP and GaAs were done at wavelengths corresponding to the suppression of various orders of multiphoton absorption. The wavelengths in GaP correspond to the suppression of 3-, 4-, 5-, 6-, and 7PA, whereas the wavelengths in GaAs correspond to the suppression of 2-, 3-, 4-, 5-, and 6PA. The specific wavelength was chosen to be in the middle of the frequency range associated with the specified order of multiphoton absorption (MPA) being investigated.

5.1.1 Gallium Phosphide

Figure 5-1(a) shows a plot of calculated THz generation efficiency as a function of pump pulse duration for various pump intensities at a pump wavelength of 1.98 μm, 4 mm crystal length and at 2 THz phase matching frequency. In the calculation of the THz generation efficiency, the pump energy inside the crystal and the Fresnel loss at the output of the crystal were considered but the diffraction efficiency was not considered. At this wavelength, 5PA is the effective highest order MPA process. The value of the 5PA coefficient used in the calculation was $4.6 \times 10^{-6}\mathrm{cm}^7/\mathrm{GW}^4$. At low pump intensity, efficiency increases as pump intensity increases. At a pump intensity of 17.5 GW/cm^2 and a pump pulse duration of 100 fs, a maximum efficiency of 0.72% was achieved. At very high intensities, the efficiency decreased, and the optimal pump pulse duration shortened. This can be attributed to the increasing THz absorption caused by fast-increasing density of free carriers which increases with pump intensity. A similar trend can be observed in Fig. 5-1 (b) for a plot of THz generation efficiency as a function of pulse duration at various intensities, 2.9 μm pump wavelength, 4 mm crystal length, and 2 THz phase matching frequency. At 2.9 μm pump wavelength, only the 7PA is the effective multiphoton absorption process. The value of the 7PA absorption coefficient used in the calculation was $5.0 \times 10^{-10}\mathrm{cm}^{11}/\mathrm{GW}^6$. However, its effect was not very strong as 5PA, thus allowing higher intensities to be used. For instance, the optimum pump intensity increased to 27.5 GW/cm^2 resulting in a maximum efficiency of 1.14% at optimal pulse duration of 125 fs.

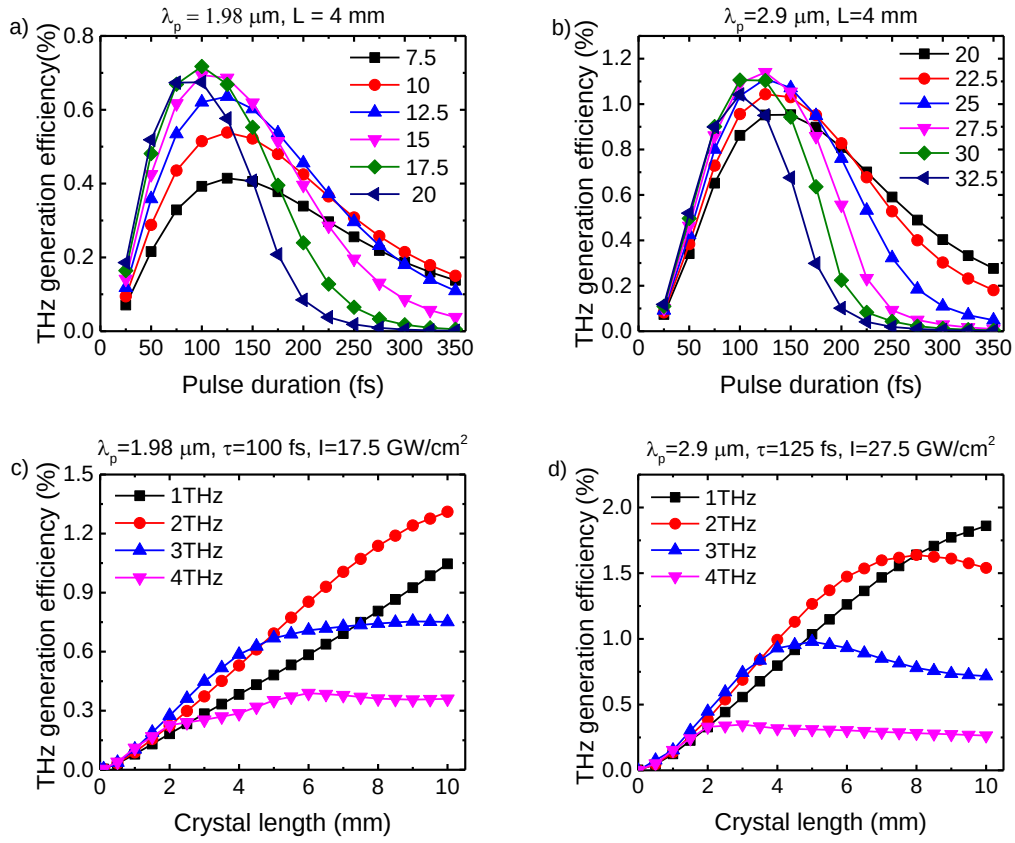

Figure 5-1: GaP THz generation simulation results. (a) and (b): efficiency (η) of THz generation versus pulse duration at different pump intensities (in GW/cm^2) and at 1.98 μm and 2.9 μm pump wavelength, respectively, for 4 mm crystal length and for 2 THz velocity matching. (c) and (d): THz generation efficiency (η) versus crystal length at 1.98 μm and 2.9 μm at 1, 2, 3 and 4 THz frequencies.

Figure 5-1 (c) displays the efficiency dependency on the crystal length for 1 THz, 2 THz, 3 THz, and 4 THz phase matching frequencies with a pump intensity of 17.5 GW/cm^2, at a wavelength of 1.98 μm, and an optimal pulse duration of 100 fs. The efficiency increases monotonically with crystal lengths at 1 THz and 2 THz. However, at 3 THz, the efficiency increases monotonically until to a crystal length 6 mm, after which the increase becomes moderate with increase of crystal length. At 4 THz, the efficiency increases with crystal length up to 6 mm, followed by a slight decrease as the crystal length increases further. The same trend can be observed at 2.9 μm wavelength (Fig. 5-1d), but with the difference that the saturation can be observed not only at 3 and 4 THz, but also at 2 THz phase matching frequency. These observations can be attributed to absorption and dispersion, as well as the larger group delay dispersion in the case of longer wavelength pumping, which increases with the THz phase matching frequency [81]. One cause for the plateau is the effect of back conversion, which increases with crystal thickness. This causes a shift of the pump spectrum, which affects the phase matching.

5.1.2 Gallium Arsenide

Figure 5-2(a) depicts a plot of calculated THz generation efficiency versus pump pulse duration for various pump intensities at a pump wavelength of 2.06 μm, 4 mm crystal length, and a phase matching frequency of 2 THz. In the calculations, 3PA coefficient value of $0.35\ \mathrm{cm}^3/\mathrm{GW}^2$ was considered since it's the only MPA process effective at this wavelength. At low pump intensity, the efficiency rises with the increase of pump intensity. Maximum efficiency of 0.12% was achieved at a pump intensity of 1.25 GW/cm^2, and a pump pulse duration of 100 fs. At very high intensities, the efficiency decreased, and the optimal pump pulse duration shortened, because of the FCA in the same way as it was in GaP, except that at much smaller pump intensities. A similar trend can be observed in Fig. 5-2(b) for the same type of plot of THz generation efficiency at 3.85 μm pump wavelength, 4 mm crystal length, and 2 THz phase matching frequency. At 3.85 μm pump wavelength, only the 5PA is the lowest effective MPA process. The value of the 5PA absorption coefficient used in the calculation was $64 \times 10^{-6}\mathrm{cm}^7/\mathrm{GW}^4$. The efficiency increased to a maximum value of 0.9% at an optimal pump intensity of 6 GW/cm^2 and an optimum pulse duration of 125 fs.

Figures 5-2 (c) and (d) show the efficiency dependency on crystal length for 1 THz, 2 THz, 3 THz, and 4 THz phase matching frequencies with a pump intensity of 1.25 and 6 GW/cm^2, at a wavelength of 2.06 and 3.85 μm, and at optimal pulse duration of 100 and 125 fs, respectively. The monotonic increase with crystal length and the saturation of this increase at higher frequencies follow a similar trend to GaP, along with the movement of this saturation to the shorter crystal lengths at longer wavelength. In these regards, the interpretation at GaP also applies to GaAs. When comparing Figs. 5-1(c) and 5-2(c), the substantial saturation of THz generation efficiency at even short crystal lengths at 1 THz phase matching can be seen in Fig. 5-2(c). This can be attributed to the strong effect of FCA at low THz frequencies in the case of GaAs pumped at short infrared wavelength, where 3PA with a high coefficient is effective.

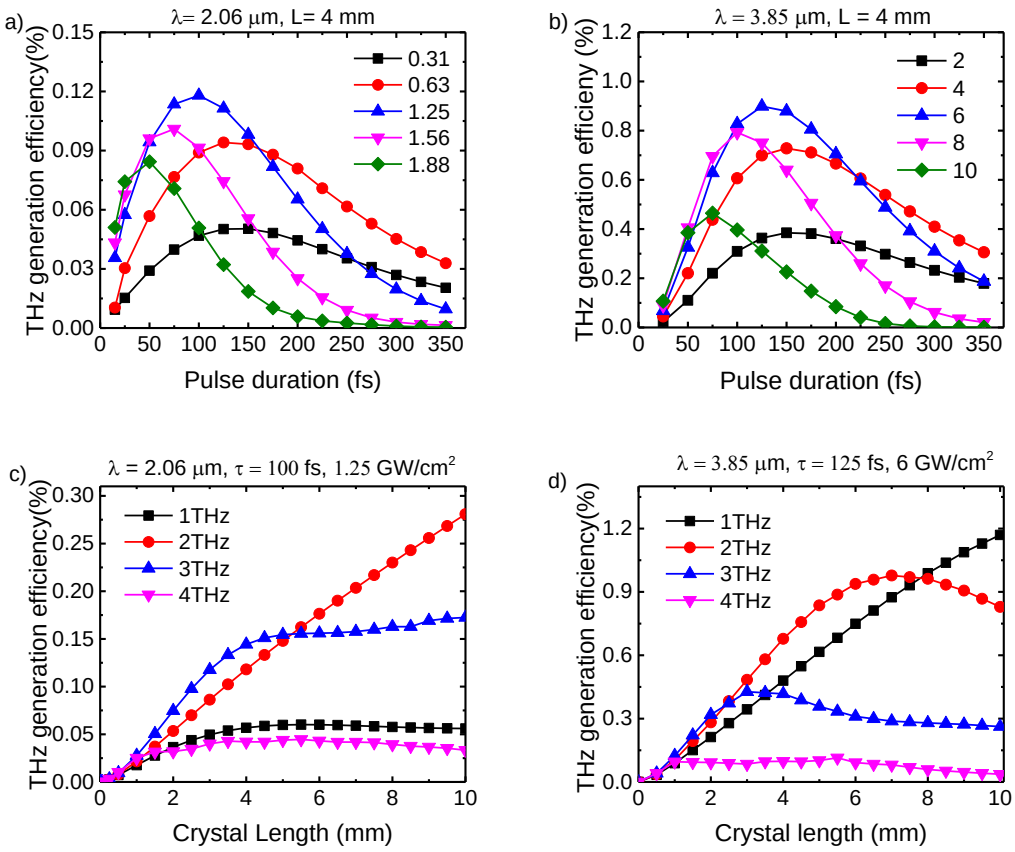

Figure 5-2: THz generation simulation results for GaAs. (a) and (b) efficiency of THz generation (η) versus pulse duration at different pump intensities (in GW/cm^2) and at 2.06 μm and 3.85 μm pump wavelength, respectively, for 4 mm crystal length and for 2 THz velocity matching, (c) and (d) THz generation efficiency versus crystal length at 2.06 μm and 3.85 μm at 1, 2, 3 and 4 THz frequencies.

Figure 5-3 shows the dependency of efficiency on the pulse duration at 2.06 μm pump wavelength, 1 mm crystal length, 2 THz frequency, and at a pump intensity of 1.25 GW/cm^2 and 2.5 GW/cm^2 for GaP and GaAs, respectively. THz generation efficiency of 0.14% and 0.23% were achieved at 2.5 GW/cm^2 in GaP and GaAs, respectively. It can be evident that GaAs has the highest THz generation efficiency at all intensities due to its large effective nonlinear coefficient. Despite this, GaP outperforms GaAs at short pump wavelengths due to the smaller MPA. The smaller bandgap of GaAs compared to GaP results in disadvantageously larger MPA coefficients for a given order.

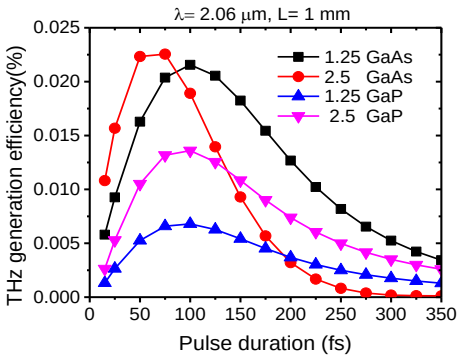

Figure 5- 3: THz generation efficiency vs pulse duration in GaP and GaAs at 2.06 μm wavelength, 2 THz phase-matching frequency, 1 mm crystal length at 1.25 and 2.5 GW/cm^2.

5.1.3 THz waveforms

Figures 5-4 (a) and (b) show simulated THz waveforms and corresponding spectra, respectively, for 4 mm thick crystal length GaP at 2.9 μm pump wavelength, optimum pulse duration of 125 fs and 27.5 GW/cm^2 pump intensity, at 2 THz, 3 THz and 4THz phase matching frequencies. At this pump wavelength, the electric field strength is approximately 23 kV/cm for 2 THz, 18.9 kV/cm for 3 THz and 9 kV/cm for 4 THz, as indicated in Fig. 5-4 (a). The decrease of the electric field strength with the increase in phase matching frequency is due to absorption and dispersion, which increases with THz frequency. It's worth to note that a shift of the peak field strength can be observed due group delay dispersion (GDD), which increases with phase matching frequency. Fig. 5-4(b) show their corresponding normalized spectra.

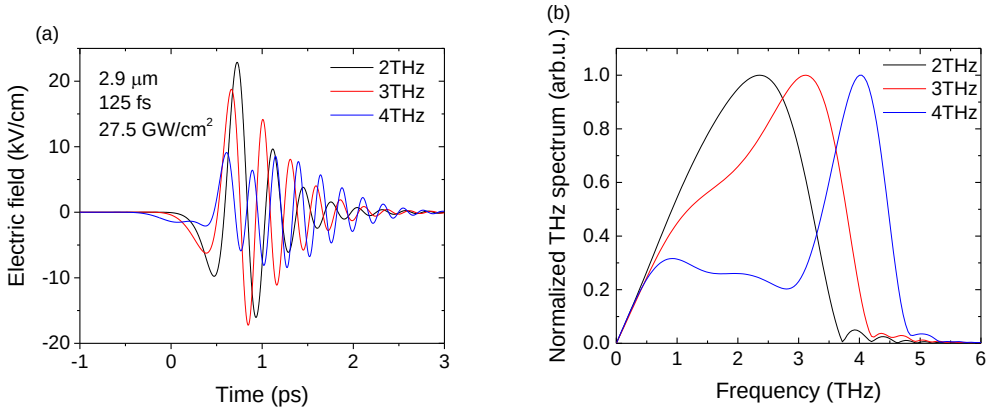

Figure 5-4: (a) Simulated GaP THz pulse field profiles for 4 mm thick crystal at 2.9 μm pump wavelength, (b) The corresponding spectra at 2, 3 and 4 THz phase matching frequencies.

Similar waveforms and spectra as GaP can be obtained in GaAs for 4 mm thick crystal length at 3.85 μm pump wavelength, optimum pulse duration of 125 fs and 6 GW/cm^2 pump intensity, at 2 THz, 3 THz and 4THz phase matching frequencies, as shown in

Figs. 5.5 (a) and (b). However, the field strengths obtained are lower than those in GaP due to stronger MPA and associated free carrier absorption in GaAs, allowing the use of intensity 4.5 times less than in GaP.

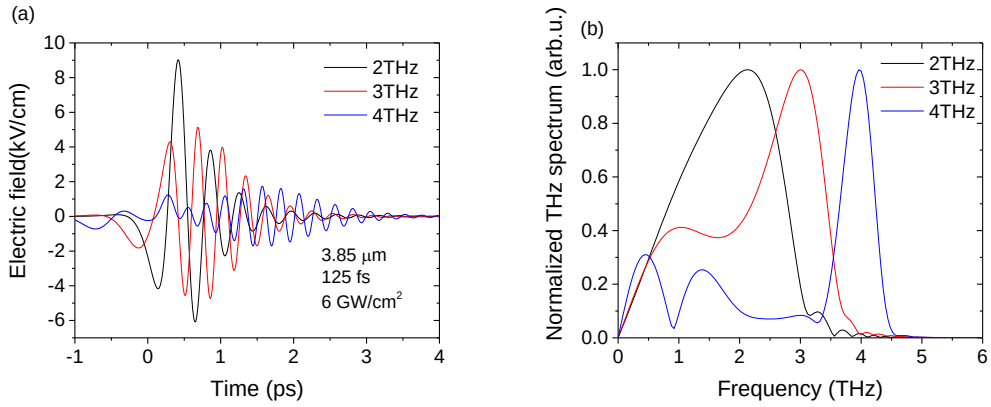

Figure 5-5: (a) Simulated GaAs THz waveforms for 4 mm thick crystal at 3.85 μm pump wavelength, (b) The corresponding spectra at 2, 3 and 4 THz phase matching frequencies.

5.2 Effect of long pumping wavelength on the conversion efficiency

Many publications have predicted and experimentally demonstrated that eliminating low order MPA processes by using long pump wavelengths can result in a significant increase in THz generation efficiency [19, 21, 70, 102], because higher pump intensities can be used without increasing the density of free carriers and their absorption in the THz range. However, to the best of our knowledge, no publication has been published on the investigation of the probable practical limit of useful long pump wavelength. We can conclude from the results of our numerical calculations that such a limit, as well as an optimum pumping wavelength, exist. The following are the reasons for the finite optimum wavelength: i) the yield from each eliminated multiphoton order decreases with the order, ii) the cascade effect increases with efficiency, iii) the efficiency of the optical parametric amplifier (OPA) intended to be used for pumping the THz source decreases with wavelength due to the Manley-Rowe relation. Figure 5-6(a) illustrates a plot of overall conversion efficiencies as a function of the MPA orders for GaAs and GaP, for crystal lengths of 4 and 7 mm, to reveal the optimal long pumping wavelength for the two different THz source materials. The overall conversion efficiency was computed by multiplying the highest THz generation efficiency at each MPA order wavelength by the OPA efficiency (calculated using the Manley-Rowe relation, and supposing 50% conversion efficiency into the signal and idler beams together). In the case of GaAs, at 4 mm crystal length, THz generation efficiency increases monotonically but with decreasing slope as MPA orders increase. At 7 mm crystal

length, the efficiency steadily increases up to 4PA, then flattens, followed by a decrease with the order of MPA; consequently, going beyond the cut-off wavelength of 4PA (3850 nm) is not advantageous. Similar behavior can be seen in GaP at 4 mm and 7 mm crystal lengths (Fig. 5-6(a)), leading to an optimal pumping wavelength at about 2000 nm (above the cut-off wavelength of 5PA).

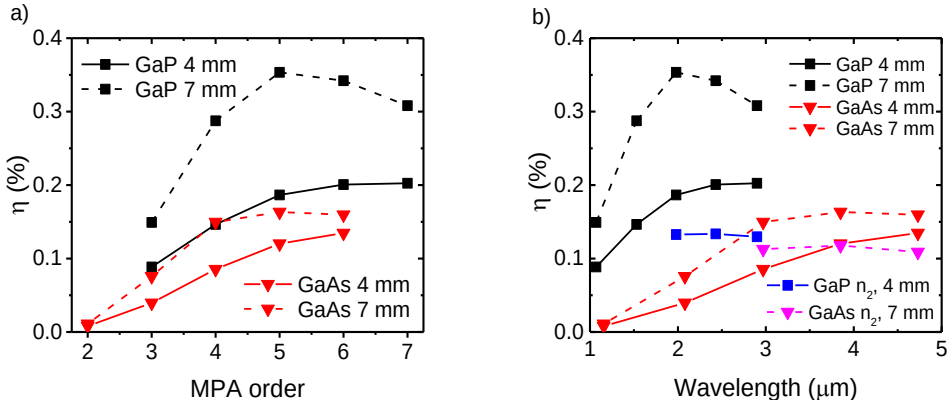

Figure 5-6: Overall conversion efficiency plotted against (a) MPA order and (b) wavelength for GaAs and GaP with the pumping OPA efficiency taken into account. Blue and magenta colours indicate results for GaP and GaAs, respectively when the effect of the nonlinear refraction was considered, with multiplication factors.

5.3 Investigation of the effect of nonlinear refraction

Ravi *et al*. investigated the effect of the nonlinear refraction on THz pulse generation in lithium niobate besides other processes [53]. However, such investigation may not have been performed in semiconductors. Only Vodopyanov paper [102] mentions that it might have some effect. Numerical calculations to investigate the effect of nonlinear refraction through self-phase modulation on the generation efficiency were performed. The model used for THz generation calculation was modified to take into account the nonlinear refractive index and its changes with the wavelength as stated in Ref. [121]. According to Fig. 5-6(b), the efficiency of GaP was reduced by approximately 30% for the 4 mm crystal length. In the case of GaAs, the efficiency decreased by almost 25% for a 7 mm crystal length. Beside lowering the THz generation efficiency, self-phase modulation shifts the optimum pumping wavelength to shorter values. The optimum wavelength realized was 2 μm for GaP and 3 μm for GaAs.

5.4 Rectangular CG profile

5.4.1 Transverse magnetic field (TM)

Rectangular structures have a higher diffraction efficiency than other profiles [122]. Figure 5-7 (a) shows a plot of calculated diffraction efficiencies for the GaP with a rectangular profile in the TM polarization state with a groove spacing of $d =$

1.74 µm as a function of groove depth h, and duty cycle f, at 2.06 µm pump wavelength and a phase matching frequency of 2 THz. Diffraction efficiencies greater than 78% can be achieved with corresponding optimal values of groove depth, $h \approx$ 0.95 to 1.15 µm and duty cycle, $f \approx 20$ to 25%, respectively. A maximum diffraction efficiency of 80% was achieved at $f = 22.5\%$ and $h = 1.04$µm. A similar plot can be seen in Fig. 5-7

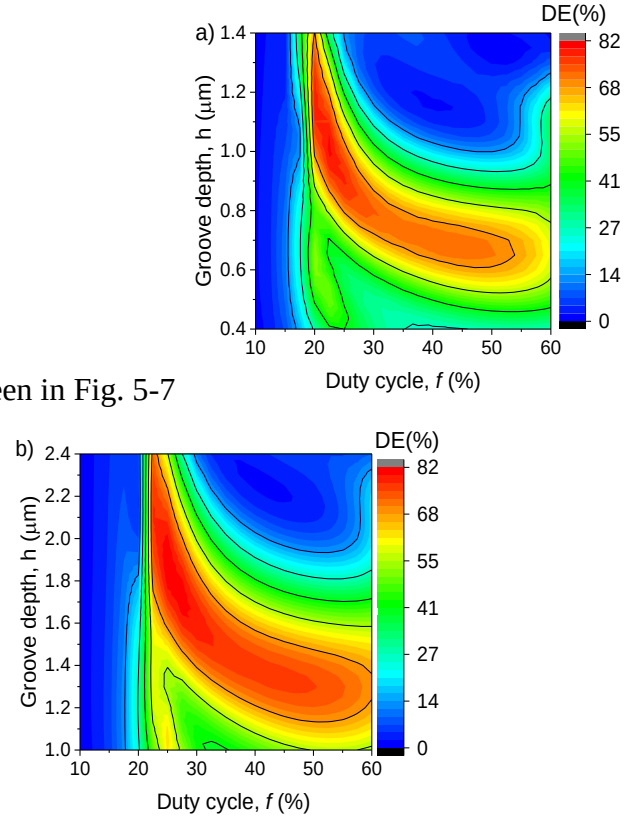

Figure 5-7(b) at 3.9 µm pump wavelength and 2 THz phase matching frequency with a groove spacing $d = 3.09$ µm. Diffraction efficiency greater than 82% can be attained with corresponding groove depth and duty cycle of $h \approx 1.7$ to 2.0 µm and $f \approx$ 22.5 to 30%, respectively. A maximum diffraction efficiency of 82% was achieved at $f = 25\%$ and $h = 1.9$ µm.

Figure 5-8 shows a plot of calculated diffraction efficiencies for GaAs in the TM polarization state versus groove depth h and duty cycle f, at 3 µm and 3.9 µm pump wavelengths, 2 THz phase matching frequency. It can be evident in Fig. 5-8 (a) that diffraction efficiencies greater than 77% with $h \approx 1.3$ to1.5 µm and $f \approx$ 17.5 to 22.5% optimum parameters can be predicted at 3 µm. A maximum diffraction efficiency of 79% was achieved at $f = 20\%$ and $h = 1.45$ µm. In addition, a diffraction efficiency of 80% was attained at 3.9 µm with optimal duty cycle, and groove depth of $f \approx 19.5$ to 22.5% and $h \approx 1.5$ to 2.1 µm, respectively. Table 5-1

summarizes the optimized parameters and calculated diffraction efficiencies for GaAs and GaP at various selected wavelength range in the TM polarization state.

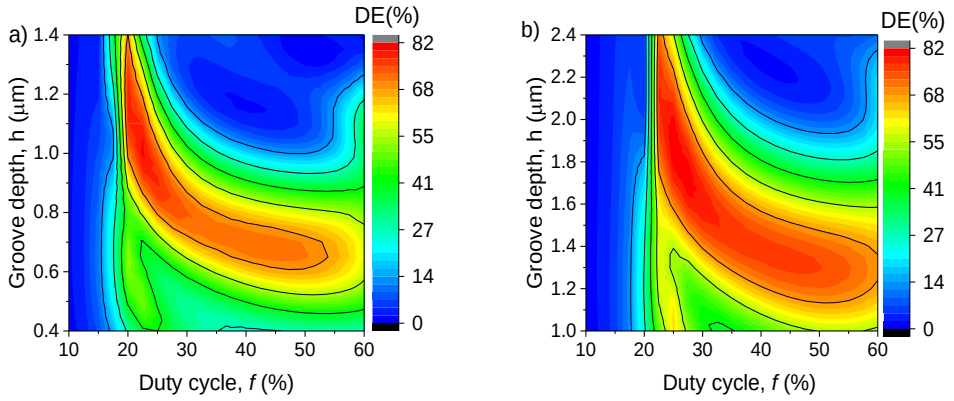

Figure 5-7: CG based on GaP: Diffraction efficiency (DE) as a function of duty cycle f and groove depth h, and 2 THz for (a) $\lambda_p = 2.06$ μm, groove spacing d = 1.74 μm and (b) $\lambda_p = 3.9$ μm, groove spacing d = 3.09 μm, both for TM mode.

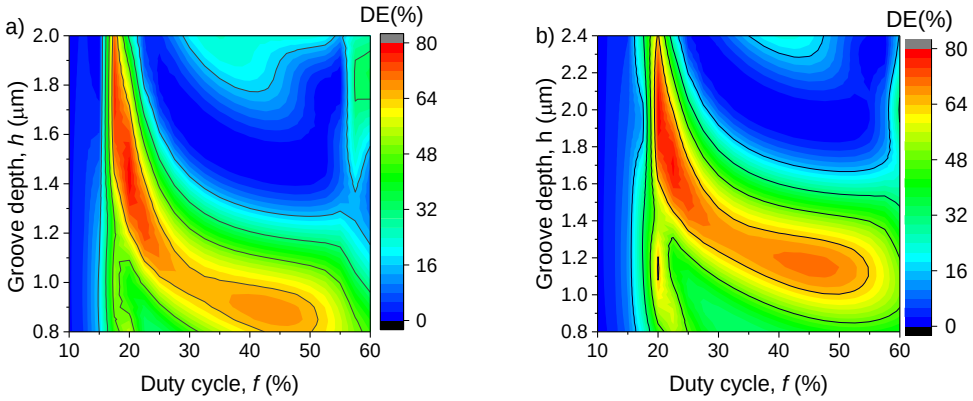

Figure 5-8: Diffraction efficiency (D.E) as a function of duty cycle f and groove depth h, and 2 THz for (a) $\lambda_p = 3\ \mu m$, groove spacing $d = 2.51\ \mu m$ and (b) $\lambda_p = 3.9\ \mu m$, groove spacing $d = 3.13\ \mu m$ both for TM mode for GaAs CG.

Table 5-1: Optimized parameters and calculated diffraction efficiencies at 2 THz for GaP and GaAs for TM polarization state.

GaP						GaAs					
λ_p (μm)	γ=β (°)	d (μm)	h(μm)	f(%)	DE(%)	λ_p (μm)	γ=β (°)	d (μm)	h(μm)	f(%)	D E(%)
2.06	22.88	1.74	1.04	22.5	80	2.06	17.38	2.05	1.41	15	75
2.4	23.66	1.97	1.25	22.5	80.5	2.074	17.48	2.06	1.42	15	77
3.0	24.28	2.41	1.35	25	81	3.00	20.98	2.51	1.45	20	79
3.90	24.78	3.09	1.9	25	82	3.90	22.04	3.13	2.04	20	80

5.4.2 Transverse electric field (TE)

Figure 5.9 (a) shows a plot of calculated diffraction efficiencies (DE) for the GaP CG with a groove spacing, $d = 1.74$ µm µm as a function of groove depth h, and duty cycle f, at 2.06 µm pump wavelength and a phase matching frequency of 2 THz in the TE mode. Diffraction efficiencies of more than 72% can be attained over the $h \approx$ 0.38 to 0.46 µm groove depth, and $f \approx 32$ to 43% duty cycle ranges, respectively, with a maximum diffraction efficiency of 75% at $h = 0.4$ µm and $f = 40\%$. A similar plot can be seen in Figure 5.9 (b) at 3 µm pump wavelength and 2 THz phase matching frequency with a groove spacing $d = 2.41$ µm. Diffraction efficiencies greater than 73% can be achieved over the $h \approx 0.59$ to 0.70 µm groove depth-, and $f \approx 40$ to 47% duty cycle ranges, respectively, with a maximum diffraction efficiency of 76% at $h =$ 0.65 µm and $f = 45\%$.

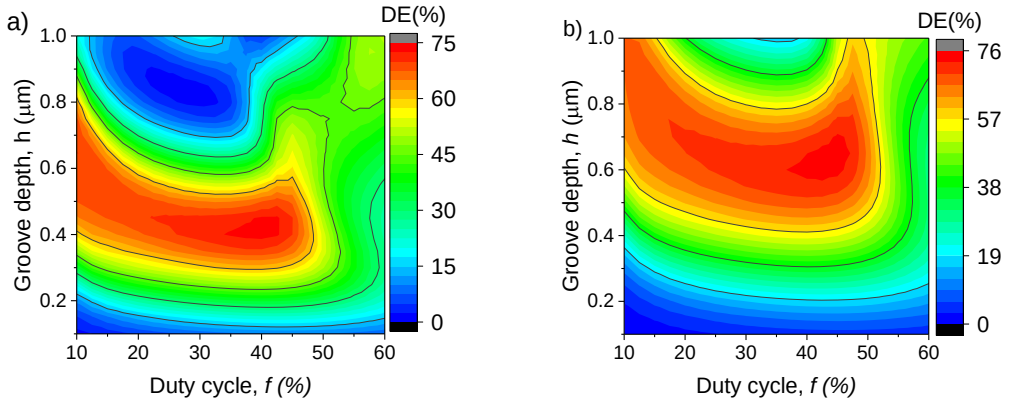

Figure 5-9: Contour plot of diffraction efficiency (DE) as a function of duty cycle *f* and groove depth h, at 2 THz velocity matching for (a) $\lambda_p = 2.06\ \mu$m groove spacing $d = 1.74\ \mu$m and (b) $\lambda_p = 3\ \mu$m groove spacing $d = 2.41\ \mu$m both for TE mode for GaP CG.

Figure 5.10 (a) shows a plot of diffraction efficiencies for GaAs CG with a groove spacing, $d = 2.51$ µm versus groove depth h and duty cycle f, at 3.00 µm and a phase matching frequency of 2 THz. It can be evident in Figure 5.10 (a) that it is feasible to achieve diffraction efficiencies greater than 66% with $h \approx 0.45$ to 0.62 µm and $f \approx$ 30 to 42%, with a maximum diffraction efficiency of 68% at $h = 0.55$ µm and $f =$ 37.5%. In addition, diffraction efficiencies greater than 67% were attained at 3.9 µm with optimal duty cycle and groove depth of $f \approx 30$ to 43% and $h \approx 0.63$ to 0.80µm, respectively (Fig. 5.10b), with a maximum diffraction efficiency of 69% at $h = 0.7$ µm and $f = 40\%$. Table 5-2 summarizes the numerical calculation of results for the optimum diffraction efficiencies for GaAs and GaP at various wavelengths.

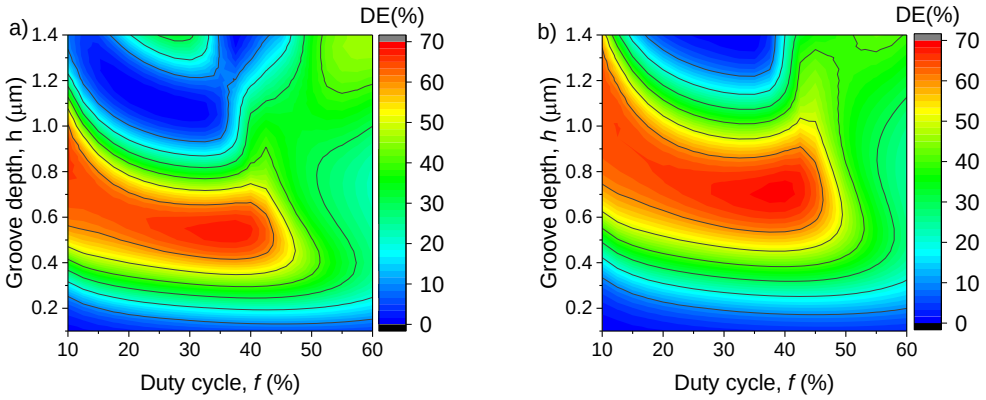

Figure 5-10: Contour plot of calculated GaAs CG diffraction efficiency (DE) as a function of duty cycle f and groove depth h, at 2THz for (a) $\lambda_p = 3.00\ \mu$m, groove spacing $d = 2.51\ \mu$m and (b) $\lambda_p = 3.90\ \mu$m, groove spacing $d = 3.13\ \mu$m both for TE mode.

Table 5-2: Optimized parameters and diffraction efficiencies at 2 THz at normal incidence for GaP and GaAs for Rectangular profile, TE polarization state.

GaP						GaAs					
λ_p (μm)	$\gamma=\theta$(°)	d (μm)	h (μm)	f (%)	DE (%)	λ_p (μm)	$\gamma=\theta$(°)	d (μm)	h (μm)	f (%)	DE (%)
1.03	7.81	2.44	0.25	42.5	59	2.06	17.38	2.05	0.35	30	63
2.06	22.88	1.74	0.4	40	74	3.00	20.98	2.51	0.55	37.5	68
3.00	24.37	2.41	0.65	45	75	3.90	22.04	3.13	0.7	40	69

Tables 5-1 and 5-2 show that diffraction efficiency increases with the wavelength in both GaP and GaAs. It can also be seen that GaP has better diffraction efficiencies at all wavelengths and polarizations than GaAs. These behaviours can be attributed to the smaller Fresnel loss at lower refraction index, and to the larger diffraction angles. The latter is favorable since the larger the diffraction angle, the fewer the number of the diffraction orders; thus, the diffracted beam is more concentrated in the lowest orders. In addition, TM polarization resulted in higher diffraction efficiencies. However, the TM polarization state was characterized by deep groove depths and low duty cycles, which is hard to fabricate; moreover, the effective nonlinear coefficient is 60% smaller typically compared to TE [123], resulting in a significantly decreased THz generation efficiency. Therefore, in the THz generation, the TE polarization state is the most preferred.

5.5 Effect of wall angle on diffraction efficiency

It has been mentioned previously that it is harder to implement a perfect rectangular grating profile due to deep groove depths and low duty cycles [109]. In addition, there are deviations of the wall angles (defined as angular deviation from the perpendicular wall of the grating surface) from the targeted perpendicular wall angles during fabrication, as can be observed on the scanning electron microscope (SEM) image of the GaP sample (Fig. 5-11). Therefore, an alternative design profile that yields a relatively shallower grating profile but with comparable diffraction efficiencies as a rectangular profile was required. The trapezoidal grating profile was considered an alternative to the rectangular profile.

Numerical calculations were carried out to investigate the influence of wall angle on the diffraction efficiency in the trapezoidal structure. The highest diffraction efficiencies were determined by optimizing the groove depth (h) and duty cycle (f) for every wall angle ϕ^{o}.

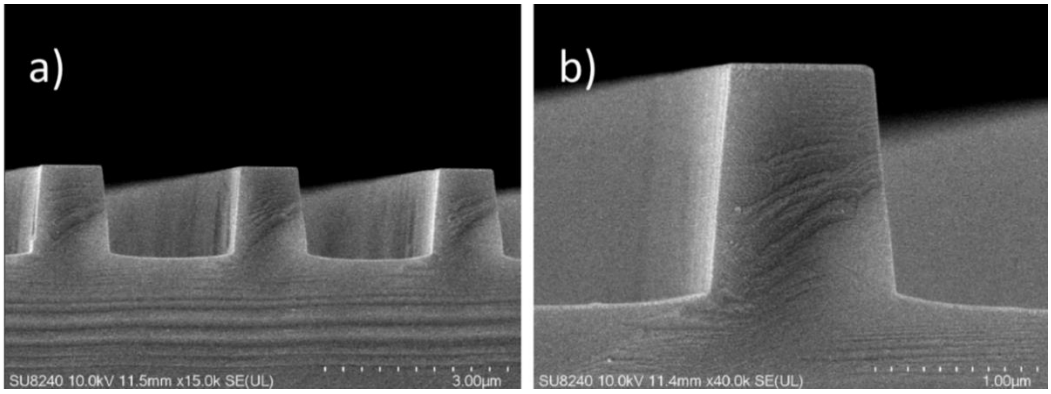

Figure 5-11: SEM images of fabricated GaP CG design in different scales (a, b). The target was rectangular profile with perpendicular walls, but about 5° wall angle was realized. *Image from Kelvin Nanotechnology, Glasgow-UK Ltd.*

Figure 5-12 depicts a contour plot of calculated diffraction efficiency for gallium phosphide as a function of duty cycle f, groove depth h at 3 THz, wall angle $(\phi) = 0^{o}$, and a pump wavelength of 2.06 µm. A maximum diffraction efficiency of 74% can be realized with $h = 0.45$ µm and $f = 42.5\%$ optimal values at the TE mode. Considering the wall angle dependency, it can be observed in Figure 5-12 (b) that at higher duty cycles (greater than 27%, the diffraction efficiency decreases monotonically from the perpendicular wall (wall angle of $\phi = 0^{o}$). However, the decrease of the diffraction efficiency with the wall angle is relatively moderate; a decrease of even less than 5% can be evident at a wall angle $\phi = 25^{o}$. On the other hand, at low duty cycles (less than

25%), the diffraction efficiency increases monotonically with wall angle up to a maximum value close to 74% at $\phi = 20^o$, followed by a monotonical decrease with wall angle.

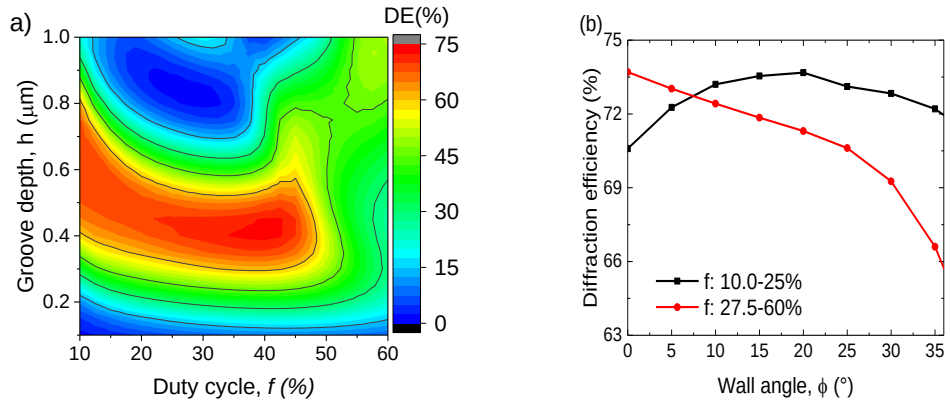

Figure 5-12: (a) Calculated GaP diffraction efficiency (DE) as a function of groove depth h and filling factor f, at perfect rectangular grating shape (wall angle, $\phi = 0^o$) and (b) Diffraction efficiency (DE) versus various wall angles $\phi(^o)$, at $\lambda_p = 2.06\ \mu$m, $d = 1.74\ \mu$m and 3 THz phase-matching frequency for TE polarization state.

The same trend can be observed for GaAs at 2.06 μm in Figure 5-13, where at higher duty cycles (greater than 27.5%), the diffraction efficiency decreases monotonically with wall angle (Fig. 5-13b), even though the decrease is negligible, for instance, at $\phi = 20^o$ the decrease is less than 2%. On the other hand, at low duty cycles (less than 25%), the diffraction efficiency increases monotonically with wall angle to a maximum value of 62% at $\phi = 10^o$, followed by a monotonical decrease with wall angle. Here, we note that the decrease of the diffraction efficiency with wall angle is minimal for $\phi < 25^o$. However, $\phi > 25^o$, there is a large drop in the diffraction efficiency.

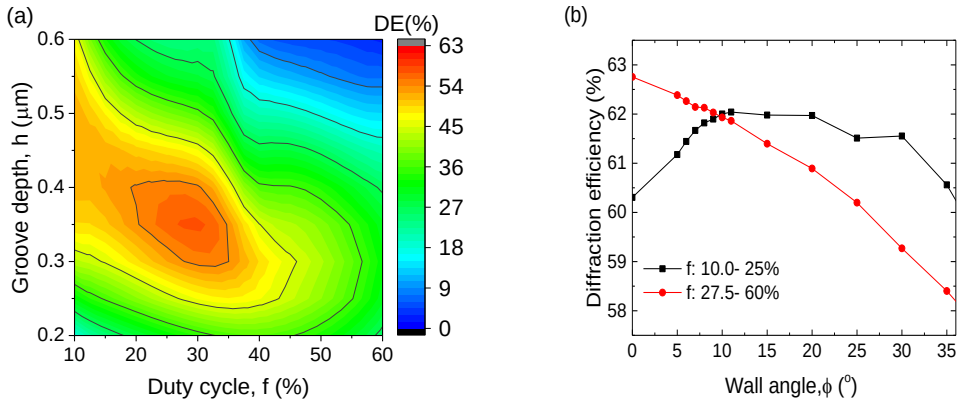

Figure 5-13: (a) Contour plot of calculated GaAs diffraction efficiency (DE) as a function of groove depth h and filling factor f, at perfect rectangular grating shape (wall angle, $\phi = 0^o$) and (b) Optimal diffraction efficiency (DE) versus various wall angles $\phi(^o)$, at $\lambda_p = 2.06\ \mu$m, $d = 2.05\ \mu$m and 3 THz phase-matching frequency for TE mode.

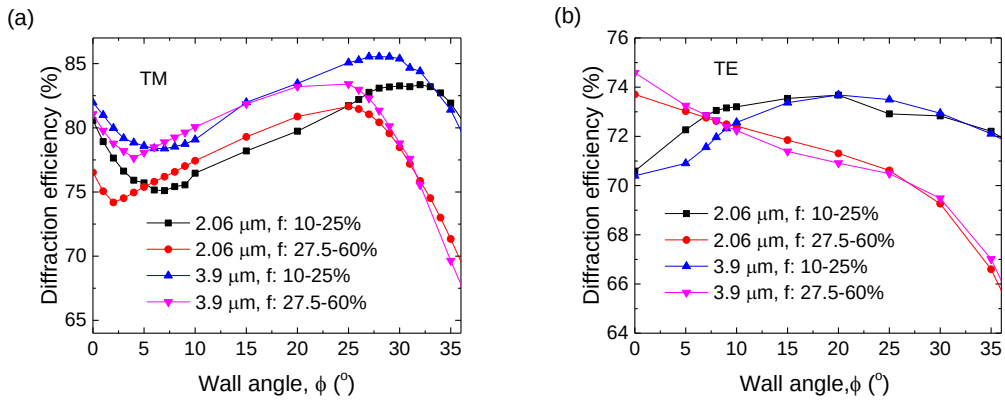

Figure 5-14: Variation of diffraction efficiency with wall angle (ϕ^o) for gallium phosphide at 2.06 μm and 3.9 μm, at 3 THz for (a) TM polarization, (b) TE polarization.

In the case of the TM polarization state (see Fig. 5-14a), the diffraction efficiency decreases monotonically from the perpendicular wall ($\phi = 0^o$) to a minimum value at a wall angle of $\phi = 5^o$ at 2.06 μm for both low duty cycles (less than 25%) and higher duty cycles (more than 27.5%), followed by a monotonical increase to a maximum value at $\phi = 27.5^o$ at low duty cycles, and $\phi = 25^o$ at higher duty cycles, respectively, as shown in Fig. 5-14. However, at wall angles greater than 25^o, the diffraction efficiency decreases with the wall angle in both low and higher duty cycles. Similar behaviour can be observed at 3.9 μm pump wavelength. In the investigated pump wavelengths, the drop of the diffraction efficiency with wall angle is less than 5%, even for a wall angle of $\phi = 25^o$. On the other hand, in the TE polarization state, the diffraction efficiency decreases monotonically from the perpendicular wall for higher duty cycles (> 27.5%) for both 2.06 μm and 3.9 μm pump wavelengths, as shown in Fig. 5-14(b). The decrease is less than 5% at wall angle 25^o. In contrast, at low duty cycles, the diffraction efficiency increases monotonically from $\phi = 5^o$ to a maximum value of 74% at 20^o wall angle, followed by a moderate decrease of 2% at 35^o, for both 2.06 μm and 3.9 μm. The same trend of variation of diffraction efficiency with wall angle can be observed in GaAs in the case of TE polarization, as shown in Fig. 5-15. Generally, in the TE and TM polarization states, deviation of angles less than $\phi = 25^o$ from the perpendicular wall results in a drop of 5% of diffraction efficiency. Therefore, while implementing the CGs the wall angle should not exceed 25^o.

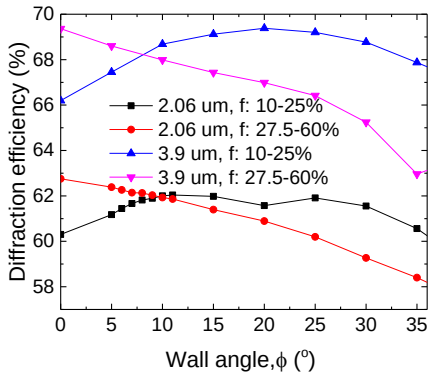

Figure 5-15: Diffraction efficiency variation with wall angle (ϕ^o) for gallium arsenide at 2.06 μm and 3.9 μm, at 3 THz for TE polarization.

5.6 Tolerances

For the fabrication of the contact grating profiles, it is essential to consider the tolerances on the duty cycle, groove depth and wall angle since its difficulty to implement a perfect CG profile. The tolerances were carefully determined from the optimum pair of parameters which yielded the highest diffraction efficiency. Figures 5-16 (a) and (b) show the diffraction efficiency in a small range around optimum duty cycle and wall angle for 2.06 µm and 3.9 µm pump wavelengths. For instance, if a diffraction efficiency of at least 75% is required at optimum duty cycle $f = 40\%$ and wall angle $\phi = 5.5^o$, at 2.06 µm (Fig. 5-16a). A duty cycle between 35% and 45%, as well as a wall angle between 4.5^o and 8^o can be tolerated. This corresponds to a fluctuation of 5% from the optimum duty cycle and about 18% from the optimum wall angle. In addition, if a diffraction efficiency of 78% is required at 3.9 µm pump wavelength with optimum parameters $f = 42\%$ and $\phi = 5^o$. A duty cycle between 34% and 48%, and a wall angle between 4^o and 8.5^o can be tolerated (Figure 5-16b). Note that the tolerances were determined by keeping the optimal groove depth fixed while varying the duty cycle and the wall angle. Similar calculations of tolerances for groove depth can be carried out by holding the duty cycle fixed while varying the groove depth and wall angle.

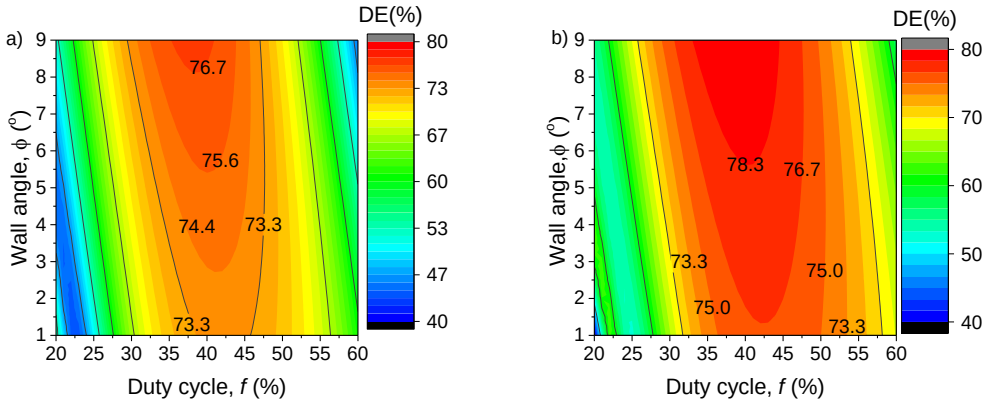

Figure 5-16: Tolerance fabrication. Diffraction efficiency as a function of wall angle (ϕ) and duty cycle *f*, for GaP (a) at 2.06 μm, $d = 1.74$ μm and optimum groove depth $h = 0.7$ μm (b) at 3.90 μm, $d = 3.09$ μm , optimum groove depth $h = 1.35$ μm both at 3 THz for trapezoidal profile TM mode.

5.7 Effect of adding antireflective (AR) coatings on the diffraction efficiency

Using numerical calculations, the effect of adding an anti-reflective coating to the CG groove profiles on diffraction efficiency was investigated for three cases, namely, adding SiO_2 ARC, adding an ARC of a material with a refractive index equal to the square root of the refractive index of the CG (GaP or GaAs) and adding a Norland optical adhesive 170 (NOA) ARC, for GaP and GaAs in the TE polarization state.

5.7.1 Adding SiO_2 AR coating

Consider adding a layer of SiO_2 on the ridges of the rectangular grating profile, as shown in Figure 4-2(c). In the case of the GaP, diffraction efficiency close to 76% can be attained by adding SiO_2 as an antireflective coating with the h_1=360 nm coating thickness calculated from Eq. 4-10, using the n_{SiO_2} = 1.437 refractive index value of SiO_2. The corresponding groove depth and duty cycle were $h \approx 0.40$ µm, and $f \approx 42.5\%$, respectively, for a wavelength of 2.06 µm. This is shown in Figure 5-17(a) by the contour plot of the calculated diffraction efficiencies for the GaP CG with a groove spacing, $d = 1.74$ µm as a function of duty cycle f, and groove depth h, at a phase matching frequency of 3 THz. To optimize the diffraction efficiency further, the antireflective coating layer thickness (h_1) was optimized numerically by varying coating thickness while keeping the optimum duty cycle and groove depth fixed. Figure 5-17(b) shows a plot of diffraction efficiency versus the optimized antireflective coating thickness (h_1). This optimization resulted in an additional 0.8% increase in the diffraction efficiency at h_1=280 nm. Numerical calculations were also performed using Al_2O_3 as an antireflecting coating on the CG. Since the optical refractive index of Al_2O_3

is near to the square root of the GaP's refractive index, a higher increase of the diffraction efficiency was expected for this case. Fig. 5-17(c) show the contour plot of the Al_2O_3 AR. However, the diffraction efficiency obtained was only slightly higher (about 1%) than those obtained with SiO_2.

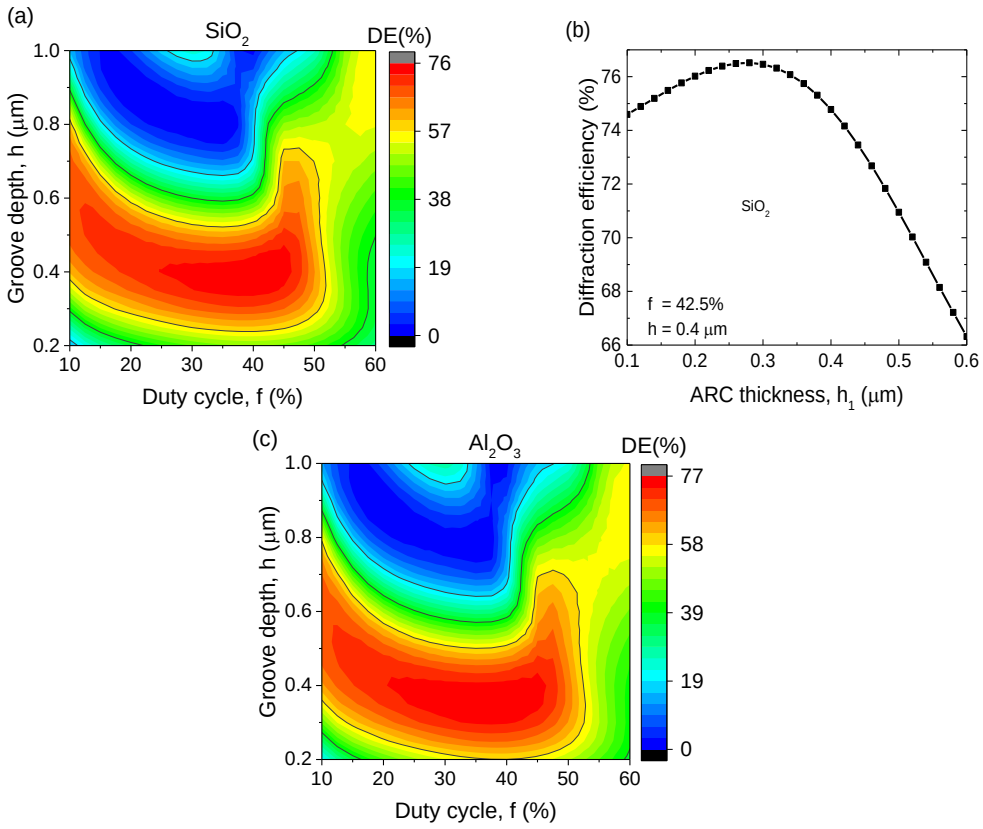

Figure 5-17: (a) Diffraction efficiency (DE) as a function of groove depth h and duty cycle f, with h_1=360 nm thick SiO_2 ARC, and (b) Diffraction efficiency (DE) versus SiO_2 ARC thickness (h_1), at $\lambda_p = 2.06\ \mu$m, $d = 1.74\ \mu$m and 3 THz (c) GaP CG with h_1=300 nm thick Al_2O_3 ARC, for GaP.

In the case of the GaAs, diffraction efficiency close to 72.5% can be achieved by adding SiO_2 as an ARC with the h_1=530 nm coating thickness which was calculated from Eq. 4-10, using the n_{SiO2}= 1.437 refractive index value. The corresponding groove depth and duty cycle were $h \approx 0.50$ μm, and $f \approx 37.5\%$, respectively, for a wavelength of 3.0 μm. This is shown in Fig. 5-18(a) by the contour plot of the calculated diffraction efficiencies for the GaAs CG with a groove spacing, $d = 2.41$ μm as a function of duty cycle f, and groove depth h, at a phase matching frequency of 3 THz. The antireflective coating layer thickness (h_1) was optimized numerically by varying coating thickness while keeping the optimum duty cycle and groove depth fixed, in order to optimize the diffraction efficiency. Figure 5-18(b) shows a plot of diffraction efficiency versus the optimized antireflective coating thickness (h_1). The optimization resulted in an additional 0.3% increase in the diffraction efficiency at h_1=460 nm.

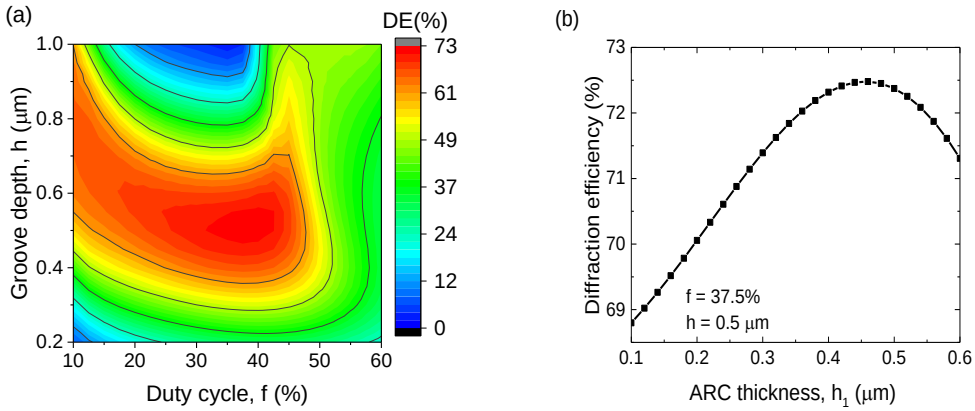

Figure 5-18: (a) Calculated GaAs diffraction efficiency (DE) as a function of groove depth h and duty cycle f, with h_1=530 nm thick SiO_2 ARC and (b) Diffraction efficiency versus SiO_2 ARC thickness (h_1), at $\lambda_p = 3.0\ \mu$m, $d = 2.41\ \mu$m, and 3 THz.

5.7.2 Adding an ARC of a material with a refractive index equal to the square root of the refractive index of the CG

Consider adding an AR layer having $n_{AR_2} = \sqrt{n_{GaP}}$ on the rectangular grating profile, as shown in Figure 4-2(d). Diffraction efficiencies close to 90% can be attained, with corresponding groove depth and duty cycle ranges of $h \approx 0.47$ to 0.51 μm, and $f \approx$ 25 to 35%, respectively, for a wavelength of 2.06 μm, with h_2= 300 nm as illustrated in Figure 5-19(a). The antireflective coating layer thickness (h_2) was optimized numerically by varying coating thickness while keeping the optimum duty cycle and groove depth fixed. Figure 5-19(b) shows a plot of diffraction efficiency versus the AR layer thickness (h_2). The maximum diffraction efficiency of 90% was achieved with optimal duty cycle, $f = 30\%$ and optimum groove depth, $h = 0.49$ μm. In this case, we found h_2= 320 nm optimal AR thickness was almost equal with the 300 nm obtained from Eq. 4-10.

On the other hand, adding an AR layer having $n_{AR_2} = \sqrt{n_{GaAs}}$ on the rectangular CG grating profile of GaAs, diffraction efficiencies close to 88% can be achieved, with corresponding groove depth and duty cycle ranges of $h \approx 0.62$ μm, and $f \approx 31\%$, respectively, for a wavelength of 3.0 μm, with h_2= 410 nm, as illustrated in Fig. 5-20(a). The antireflective coating layer thickness (h_2) was optimized numerically by varying coating thickness while keeping the optimum duty cycle and groove depth fixed. Figure 5-20(b) shows a plot of diffraction efficiency versus the ARC layer thickness (h_2). A maximum diffraction efficiency of 88.6% was achieved with optimal

duty cycle, $f = 27.5\%$ and optimum groove depth, $h = 0.65$ µm with h_2= 440 nm as the optimal ARC thickness.

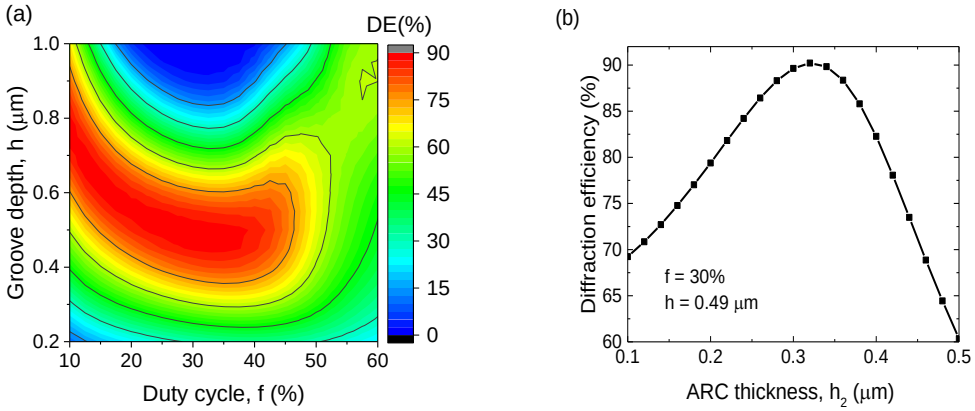

Figure 5-19: (a) Calculated GaP diffraction efficiency (DE) as a function of groove depth h and duty cycle f, with h_2=300 nm thick $n_{AR_2} = \sqrt{n_{GaP}}$ ARC and (b) Diffraction efficiency (DE) versus ARC thickness (h_2), at $\lambda_p =$ 2.06 μm, d = 1.74 μm and 3 THz.

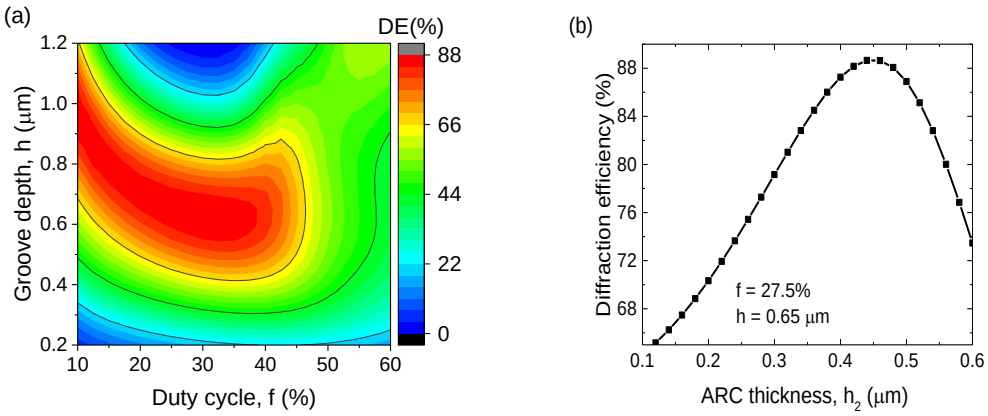

Figure 5-20: (a) GaAs calculated diffraction efficiency (DE) as a function of groove depth h and duty cycle f, with h_2=410 nm thick $n_{AR_2} = \sqrt{n_{GaAs}}$ ARC and (b) Diffraction efficiency (DE) versus ARC thickness (h_2), at $\lambda_p =$ 3.0 μm, d = 2.41 μm and 3 THz.

5.7.3 Adding Norland optical adhesive 170 AR

Consider adding a layer of NOA as an AR layer on a rectangular GaP CG profile, as shown in Fig. 4-2(e). Figure 5-21(a) shows a contour plot of the calculated diffraction efficiencies as a function of groove depth (h) and duty cycle (f) with addition of NOA AR coating. Diffraction efficiencies more than 90% can be achieved over the optimal ranges of $h \approx 0.70$ to 0.80 µm and $f \approx 27$ to 37%. The antireflective coating layer thickness (h_3) was optimized numerically by varying coating thickness while keeping the optimum duty cycle and optimum groove depth fixed at $f = 32.5\%$ and $h =$ 0.75 µm, respectively, as illustrated in Fig. 5-21(b). This resulted in a maximum

diffraction efficiency of as high as 92%, with $f = 32.5\%$ and $h = 0.75$ µm as the optimal parameters.

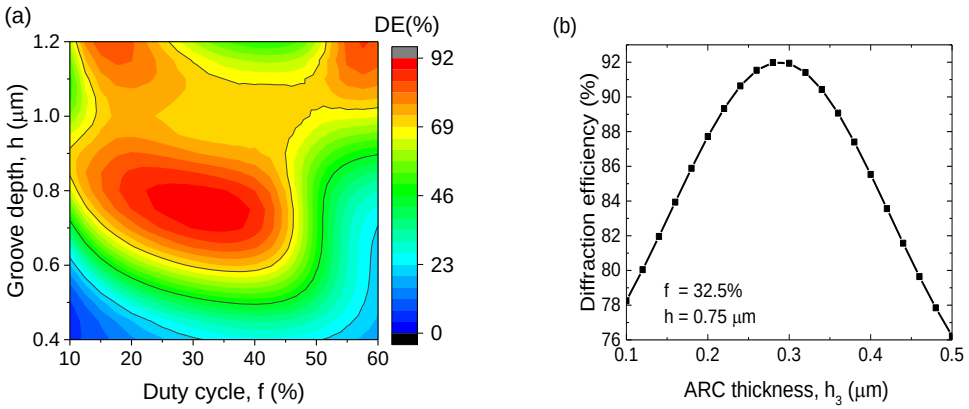

Figure 5- 21: (a) Diffraction efficiency (DE) as a function of groove depth h and duty cycle f, with h_3 = 315 nm thick NOA ARC and (b) Diffraction efficiency versus NOA ARC thickness (h_3), at $\lambda_p = 2.06$ μm, $d =$ 1.7 μm and 3 THz, both for GaP.

On the other hand, adding an NOA AR layer on the rectangular GaAs CG profile, diffraction efficiencies close to 89% can be achieved, with corresponding groove depth and duty cycle ranges of $h \approx 0.95$ to 1.05 µm, and $f \approx 22.5$ to 32.5%, respectively, for a wavelength of 3.0 µm, with h_3= 460 nm, as illustrated in Fig. 5-22(a). The anti-reflective coating layer thickness (h_3) was optimized numerically by varying coating thickness while keeping the optimum duty cycle and groove depth fixed. However, the optimized AR thickness was equal with 460 nm obtained from Eq. 4-10. Figure 5-22(b) shows a plot of diffraction efficiency versus the AR layer thickness (h_3). A maximum diffraction efficiency of 90% was achieved with optimal duty cycle, $f = 27.5\%$ and optimum groove depth, $h = 1.0$ µm with h_3= 460 nm as the optimal ARC thickness. Table 5-3 show a summary of the calculated diffraction efficiencies and their corresponding optimum parameters for the three cases of adding AR. The optimal AR layer thickness for each case is also indicated.

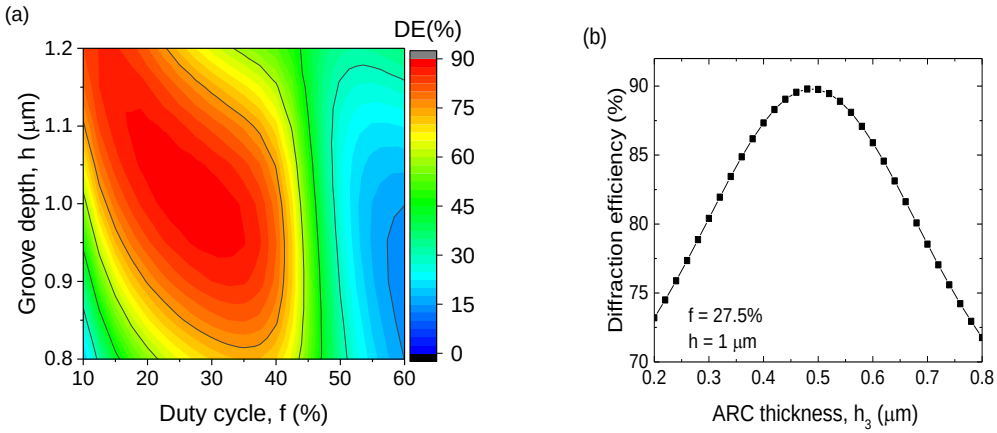

Figure 5-22: (a) Contour plot of calculated GaAs diffraction efficiency (DE) as a function of groove depth h and duty cycle f, with h_3 = 460 nm thick NOA ARC and (b) Diffraction efficiency versus NOA ARC thickness (h_3), at λ_p = 3.0 μm, d = 2.41 μm, and 3 THz.

Table 5-3: Summary of calculated diffraction efficiencies and their corresponding parameters with ARC, TE mode.

Material	ARC	n_c	f(%)	h(nm)	DE(%)	Optimized DE(%)
GaP *	-	-	42	430	74.2	-
	$AR_1(SiO_2)$	1.44	42.5	400	75.7 (h_1=360nm)	76.5 (h_1=280nm)
	$AR_1(Al_2O_3)$	1.73	37.5	350	77.0 (h_1=350nm)	77.4 (h_1=260nm)
	$AR_2(n_{AR_2} = \sqrt{n_{GaP}})$	1.74	30	490	89.8 (h_2=300nm)	90.2 (h_2=320nm)
	AR_3(NOA)	1.64	32.5	750	91.6 (h_3=315nm)	91.9 (h_3=300nm)
GaAs *	-	-	39	540	70.0	-
	$AR_1(SiO_2)$	1.42	37.5	500	72.2 (h_1=530nm)	72.5 (h_1=460nm)
	$AR_2(n_{AR_2} = \sqrt{n_{GaAs}})$	1.83	31	620	88.0 (h_2=410nm)	88.6 (h_2=440nm)
	AR_3(NOA)	1.62	27.5	1000	89.6 (h_3=460nm)	89.8 (h_3=460nm)

Table 5-3 shows that the highest diffraction efficiencies of CG without ARC and with any type of ARC are achieved when the duty cycle is less than 50%. In contrast to the simple linear system formulation of nonparaxial scalar diffraction theory of rectangular phase gratings that predicts maximum diffraction efficiency into the 1st order for a 50% duty cycle [124]. Transmission gratings utilized in the Littrow arrangement are well known to exhibit maximum diffraction efficiencies at less than 50% duty cycle [125].

Furthermore, for non-normal incidence, numerical simulations of LN and ZnTe rectangular CGs indicate maximum diffraction efficiency at duty cycles of less than 50% [126, 127]. However, this was not stated in the simulations for normal incidence

[127], and a 50% duty cycle was used in all realizations of semiconductor CGs [56, 118, 128]. It has to be noted, that according to our results less than 50% duty cycle resulted in the highest diffraction efficiency for normal incidence, as shown in Tables 5-1 and 5-2.

Clausnitzer *et al*. explained how rectangular phase transmission gratings function by examining the two propagating modes within the grating structure and considering their respective cumulative phase difference within the grating as well as their overlap integral with the pumping [129]. Although a quantitative explanation of the results based on that theory is beyond the scope of this study, we observe that such an explanation should be attainable in our case as well. Furthermore, evidence and significance of the effect of the phase difference of the two modes (one, the "semiconductor mode," propagates predominantly inside the semiconductor, and the second, the "air mode," propagates predominantly inside the air) are shown in Figs. 5-17(a) and (c), 5-18(a), 5-19(a), and 5-20(a), and in a less pronounced way in Figs. 5-21(a) and 5-22(a). In these Figs., the optimum groove depth increases as the duty cycle decreases. This method can keep the phase difference between the two modes roughly constant: When the duty cycle is reduced, a greater portion of the electric field corresponding to the "semiconductor mode" propagates within the air and, as a result, propagates faster. To acquire the same phase difference, a longer path is required.

According to Table 5-3, the first of the three investigated methods for increasing diffraction efficiency by minimizing Fresnel loss resulted in only around a 3% relative increase. However, it is worthwhile to consider using this method because, as previously stated, it involves fewer process steps during the CG preparation. The second (classical) method of adding ARC leads to a substantially higher relative increase in diffraction efficiency of 22% and 28% for GaP and GaAs CG, respectively. As a result, using this way is strongly recommended. Furthermore, unlike the first method, the optimum ARC thickness, in this case, equals the value predicted by Eq. 4-10. The third ARC method produces even higher relative increases in diffraction efficiency for GaP and GaAs CG of 24% and 30%, respectively. These values are comparable to the Fresnel losses of bare GaP and GaAs surfaces, which are 35% and 41%, respectively. As a result, adapting this procedure is strongly recommended if

technically feasible. Another advantage is that such a CG would be more durable because of its flat surface. Comparing the relative increase of the diffraction efficiency in GaAs and GaP, as shown in Table 5-3, GaAs has a larger relative increase than GaP. This is because GaAs has a higher refractive index than GaP; this greater rise is also accompanied by a higher Fresnel loss.

Chapter Six

6.0 Conclusion and Outlook

6.1 Conclusion

Numerical calculations were performed to determine the optimal pumping conditions and phase matching frequency for single-cycle THz pulse generation via optical rectification in GaAs and GaP in the broad pump wavelength range. An optimum pulse duration and phase matching frequency of 125 fs and 2 THz were realized for both GaP and GaAs. According to THz generation calculations, THz conversion efficiency of 0.9% and more than 1.14% in GaAs and GaP, respectively, can be achieved. It was also realized that higher pump intensities can be used in GaP compared to GaAs. It was recognised that pumping at longer wavelengths was better for the highest THz generation efficiency due to the absence of strong low-order multiphoton. However, limits of long pumping wavelengths that are not prosperous to exceed, were realized. In the case of GaAs, 3 μm, the cut-off wavelengths of 4PA was realized as the optimal long pumping wavelength, whereas in GaP, we realized 2 μm which correspond to the cut-off wavelength of 5PA as the optimal long pump wavelength. It was also found that the self-phase modulation due to the nonlinear refractive index reduces the THz generation efficiency and lowers the optimal pump wavelength.

In addition, demonstration of the basic designs of GaAs and GaP contact grating THz sources in order to develop an alternative semiconductor THz source for further upscaling of THz pulse energy and field strength by optical rectification of ultrashort laser pulses was done. The results reveal that rectangular contact grating profiles in the 2 to 4 μm infrared pump wavelength range, diffraction efficiencies of 69% and 75% in GaAs and GaP, respectively, can be attained in the TE mode. These efficiencies can be increase to values greater than 89% and 91% in GaAs and GaP, respectively, by addition of antireflective coatings. However, it was realized that the optimum parameters of the contact grating that result in the highest diffraction efficiency differed in the cases of having and not having an antireflective coating. The numerical calculations have also revealed that if the contact grating results in a trapezoidal profile with a wall angle less than 25^{o}, the diffraction efficiency drop remains below 5% for the reoptimized grating parameters, hence a less significant effect.

6.2. Outlook

Demonstration of THz pulse generation utilizing the GaP and GaAs contact grating THz sources should be performed to confirm the conversion efficiency. The contact grating technology can further be applied to other semiconductor materials. The investigated methods of adding an antireflection coating can also be applied to other semiconductor contact gratings like ZnSe and CdTe.

Chapter Seven

7.0 Thesis statements

1. Numerical simulations were performed in the 1 to 5 μm wavelength range to investigate the possible advantage of using longer pumping wavelengths to suppress the 2- to 7-PA in GaAs and GaP. A 0.9% and 1.14% conversion efficiency were predicted for GaAs and GaP, respectively, at an optimum pulse duration of 125 fs and optimum phase matching frequency of 2 THz.
2. The effect of the nonlinear refraction index and the wavelength dependency of the pumping OPA efficiency on the overall THz generation efficiency in GaP and GaAs was investigated numerically. According to the model used, it was realized that the nonlinear refractive index significantly reduced the terahertz generation efficiency and shortened the optimum wavelength in the semiconductors needed to achieve the highest conversion efficiency. The optimum wavelength realized was 2 μm for GaP and 3 μm for GaAs.
3. Using numerical calculations, designs of GaP and GaAs contact grating THz sources based on rectangular and trapezoidal profiles in the 2 to 4 μm infrared wavelength range were performed. With proper choice of the design parameters, diffraction efficiencies as high as 69% and 75% for a rectangular profile in the ±1st diffraction orders in the TE polarization state, and 80% and 82% in the TM polarization state, can be achieved in GaAs and GaP, respectively, with the pump beam incident perpendicular to the grating surface.
4. Due to the possible inaccuracy of the fabrication technique, deviations from perfect perpendicular wall in case of rectangular CG profiles may be realized. In order to achieve practical implementation numerical calculations were performed at various wall angles. At a wall angle of less than $\phi = 25^o$, diffraction efficiency loss of less than 5% was predicted in both GaP and GaAs. In contrast, beyond $\phi = 25^o$, the diffraction efficiency drops monotonically with an increase of wall angle. Therefore, special attention should be taken not to exceed a wall angle of 25^o.
5. Three possible methods for increasing the diffraction efficiencies of GaP CG and GaAs CG were investigated by numerical simulations, in the useful ±1 diffraction orders from 69-75% to more than 88-90% by adding an AR coating on the contact gratings. Based on the rectangular CG profiles, diffraction efficiency of more than 91% and 89% were predicted in GaP and GaAs, in the TE polarization state, at 2.06 μm and 3 μm pump wavelengths, respectively. The antireflective coatings helped minimize Fresnel losses due to reflections.

Chapter Eight

8.0 Összefoglaló

8.1 Absztrakt

Elméleti számolásokon keresztül megvizsgáltam különböző félvezető anyagú, bináris, illetve trapezoid rácsstruktúrájú kontaktrács terahertz- (THz-) forrásokat. Mind transzverzális elektromos (TE), mind transzverzális mágneses (TM) módusokat vizsgáltam. Bináris profil esetén közel hullámhosszfüggetlen 69% és 75%-os diffrakciós hatásfokot jósoltam a ± 1. rendekben TE módusban, GaAs és GaP esetén. TM módusnál a kiszámolt diffrakciós hatásfokok valamennyivel magasabb voltak, 80% és 82%, GaAs és GaP esetén. A bináris profilokhoz hasonló diffrakciós hatásfokokat kaptam trapezoid struktúra esetén a különböző módusokban. Az antireflexiós bevonatok diffrakciós-hatásfok-növelő hatását szintén vizsgáltam. 3 és 2.06 μm pumpáló hullámhosszakon, TE módusban, 89% és 91%-os diffrakciós hatásfokot számoltam GaAs és GaP esetén. Numerikus szimulációkon keresztül megvizsgáltam, hogyan változik a THz-keltés hatásfoka 1 és 5 μm közötti pumpáló hullámhossztartományon, ha a 2-től 7-fotonos abszorpció hatásait kiküszöbölöm GaAs-ben és GaP-ban. Megállapítottam, hogy a kétfotonos abszorpció kiküszöbölése nagymértékben növeli a THz-keltés hatásfokát. A magasabbrendű többfotonos abszorpciók kioltása azonban egyre kisebb mértékben járul hozzá a konverziós hatásfok növeléséhez, 3 μm hullámhossz fölötti pumpálásnál, GaAs és GaP esetében. Ezek mellett megállapítottam, hogy 0.9% illetve 1.14% konverziós hatásfokok érhetőek el GaAs-ben és GaP-ban, az 5-fotonos abszorpció kiküszöbölésével. Ezekhez a hatásfokokhoz meghatároztam, hogy az ideális pumpáló impulzushossz 125 fs 2 THz-es fázisillesztési frekvencián. Továbbá meghatároztam, hogy a nemlineáris törésmutató jelentősen csökkenti a THz-keltés hatásfokát és a maximális konverziós hatásfokhoz tartozó pumpáló hullámhosszat rövidíti.

8.2 Tézispontok

1. Numerikus szimulációkat készítettem 1 és 5 μm-es pumpáló hullámhossztartományon, hogy megvizsgáljam az előnyeit a 2-7 fotonos abszorpció kiküszöbölésének hosszú pumpáló hullámhosszokat alkalmazva GaP-ban és GaAs-ben. Optimális 2 THz-es fázisillesztési frekvenciát és optimális 125 fs-os pumpáló impulzushosszt feltételezve 0.9% és 1.14% hatásfokokat jósoltam GaAs-ben és GaP-ban [S1].

2. A nemlineáris törésmutató és az optikai parametrikus erősítés hullámhosszfüggő hatásfokát is figyelembe véve numerikus szimulációkkal vizsgáltam a teljes THz-keltési hatásfokot GaP-ban és GaAs-ben. A használt modell alapján megállapítottam, hogy a nemlineáris törésmutató jelentősen csökkenti a THz-keltés hatásfokát és rövidíti az optimális pumpáló hullámhosszat. Ez az optimális hullámhossz GaP esetén 2 μm, míg GaAs esetén 3 μm [S1].
3. Numerikus szimulációk segítségével megterveztem GaP és GaAs anyagú kontaktrács THz-forrásokat bináris és trapezoid profilokkal a 2-4 μm-es hullámhossz tartományra. A tervezési paraméterek optimális megválasztásával 69%-os és 75%-os diffrackiós hatásfokok érhetőek el a ± 1. rendekben TE polarizációval, és 80%-82%-os hatásfokok TM polarizációval, GaAs-ben és GaP-an, ha a pumpáló nyaláb merőleges a rács felületére.
4. Mivel a megmunkálás tökéletlenségei miatt a teljesen merőleges falak nem garantálhatók, emiatt a számolásokat kiterjesztettem a 0°-ostól eltérő falszögekre is. Megmutattam, hogy 25°-nál kisebb falszögek esetén a hatásfokveszteség kevesebb, mint 5% mind GaP-ban és GaAs-ben. Ezzel szemben 25°-nál nagyobb falszögek esetén a hatásfok monoton módon csökken a falszög növekedésével. Emiatt figyelni kell rá, hogy a fal dőlésének szöge ne haladja meg a 25°-ot.
5. Három különböző módszert vizsgáltam szimulációkon keresztül, hogy növeljem a 69-75%-os diffrakciós hatásfokokat GaP és GaAs kontaktrácsok esetén a ± 1. rendekben, és azt tapasztaltam, hogy antireflexiós bevonat hozzáadásával 88-90%-os hatásfokok is elérhetők. 91% és 89%-os hatásfokokat vetítettem előre GaP-ban és GaAs-ben, TE polarizációban, 2.06 μm és 3 μm pumpáló hullámhosszakon, amit a Fresnel-veszteség minimalizálásával magyaráztam.

Chapter Nine

9.0 Summary

9.1 Introduction

The advent of THz sources, which can generate pulses with high energies and peak electric and magnetic fields in the THz range (0 to 10 THz), has made new feasible applications such as nonlinear spectroscopy [36], manipulation of charged particles [40] and proposed for hadron therapy [28]. Terahertz pulses have been generated by optical rectification based on tilted-pulse-front excitation techniques [58]. The highest reported THz pulse energy in the low-frequency range to date utilizing the TPFP technique is more than 1.4 mJ in LN [14]. However, there are challenges in scaling the THz pulse energies and field strengths in lithium niobate; this includes: nonlinear interaction between the pump and THz beam leads to beam distortions [107, 108], large PFT angle leads to limited interaction length for THz pulse generation due to large angular dispersion [81]. In addition, the use of imaging optics in the case of conventional TPFP leads to imaging errors, which distorts the THz beam making it more difficult to focus the THz beam [82]. Several techniques to improve the conventional TPFP technique have been proposed and demonstrated [83-87]. On the other hand, organic materials have strong phonon absorption at low frequencies [76], are available in small sizes [17], and have a relatively low damage threshold [25]; this limits THz scalability.

Furthermore, THz pulse generation in semiconductors pumped in collinear geometry has been demonstrated [20, 97]. Unfortunately, semiconductors have small bandgap energies (E_g), which results in saturation effects when pumped at collinear geometry due to the presence of strong low order multiphoton absorption [19], limiting the useful pump intensity and, hence the terahertz energy. Pumping at long infrared pump wavelengths has been proposed and applied [51, 56] to eliminate low-order multiphoton absorption. THz pulses with energies as high as 14 μJ and conversion efficiency of 0.7% have been reported in ZnTe pumped at 1.7 μm infrared pump wavelength [19]. The contact grating (CG) based on TPFP was proposed [83] to achieve a collinear THz generation scheme at long pump wavelengths. Scalable and perfectly THz pulses with up to 3.9 μJ and conversion efficiency of 0.3% have been reported in the ZnTe CG source [56]. However, growing large size ZnTe crystals is difficult due to microbubbles [56] . Recently, GaP CG source has been reported [118]. GaP and GaAs are feasible

alternatives as they are easier to grow and are less expensive [130]. This dissertation presents numerical simulations to design optimal GaP CG and GaAs CG THz sources and three ways of increasing the diffraction efficiencies to more than 91% in GaP and 89% GaAs for efficient THz pulse generation in the long infrared wavelengths are presented. In addition, numerical calculations were performed to determine the optimum pumping wavelength; in the calculations, the effect of the nonlinear refractive index and the wavelength dependence of the pumping OPA efficiency were taken into account.

9.2 Aims and objectives

The main aim of this work was to numerically investigate THz generation efficiency and design optimized, scalable and highly efficient semiconductor contact grating terahertz sources pumped at a long infrared wavelength range.

By numerical simulations, the basic design aspects of semiconductors ZnTe and GaP, as well as their optimal pumping and phase matching conditions at infrared wavelengths below 2 μm, have been determined [99]. The first objective of the study was to extend by numerical calculations the determination of design aspects and the optimum pumping and phase matching conditions of GaAs and GaP pumped at long infrared wavelengths greater than 2 μm. I aimed to determine by numerical calculations the optimum pumping parameters such as pulse duration, pump intensity, crystal length, and phase-matching frequency that yield the highest terahertz conversion efficiency to give more insight into the semiconductor contact grating THz sources. In addition, It has been predicted and demonstrated that the elimination of low order multiphoton absorption (MPA) processes by using long pump wavelength can result in a significant increase in THz generation efficiency [19, 21, 70, 102] due to the possibility of using higher pump intensities without increasing the density of free carriers and their absorption in the THz range.

The second objective of the study was to numerically investigate the possibility of increasing terahertz generation efficiency in semiconductors by using longer pump wavelengths to suppress strong low-order multiphoton absorption and determine optimum long pump wavelength limit where the suppression of multiphoton absorption in semiconductors GaP and GaAs is beneficial. I aimed to determine by numerical calculations the extent to which the suppression of higher order multiphoton absorption significantly benefits the terahertz generation efficiency by determining the optimum

wavelength. I also aimed to investigate the effect of nonlinear refractive index on THz generation efficiency.

Scalable THz pulses with up to 3.9 μJ and a conversion efficiency of 0.3% have been reported in the ZnTe CG source [56]. However, growing large size ZnTe crystals is difficult due to microbubbles[56]. Semiconductors, GaP, and GaAs are feasible alternatives to ZnTe.

The third objective was to extend the design of the scalable and efficient semiconductor contact grating to other semiconductors GaP and GaAs THz sources. I aimed to determine a set of design parameters by numerical calculations that yield the highest diffraction efficiencies based on rectangular and trapezoidal structures in GaP and GaAs contact gratings to give practical guidance for designing and fabrication of highly efficient THz pulse sources. I also investigated the effect of deviations from the perpendicular wall on diffraction efficiency.

The fourth objective was to investigate the possible ways of increasing the diffraction efficiencies of the GaP and GaAs as high as possible to even more than 90% at long infrared wavelengths. I aimed to enhance the diffraction efficiencies of the GaP and GaAs contact grating by adding an antireflective coating layer to the contact grating. Here, a numerical investigation of three different ways of adding antireflective coatings was performed.

9.3 New scientific results

I. According to the numerical calculations I performed for THz generation efficiency in GaP and GaAs crystals pumped in the wavelength range of 1 to 5 μm, I have shown that there is a strong benefit of suppression of 2PA in both GaP and GaAs. I have also shown a limit of long infrared wavelength pumping where the suppression of higher order multiphoton absorption (MPA) is beneficial. Beyond that limit, no benefit is associated with the suppression of MPA. In the case of GaP, such a limit is about 2 μm, corresponding to the cut-off wavelength of 5PA, whereas in GaAs, the limit is 3.85 μm, corresponding to the cut-off wavelength of 4PA. I have also shown that pumping at wavelengths that allows suppression of 2PA and higher order MPA, THz conversion efficiency of 0.9% and 1.14% can be achieved in GaAs and GaP, respectively [S1].

II. According to my numerical calculations, using the modified model of THz generation, which took into account the nonlinear refractive index and its changes

with the wavelength, besides other processes in the semiconductors. For the first time, I have shown that the nonlinear refractive index causes a decrease in the THz generation efficiency and causes a shift of optimum pumping wavelengths to shorter values in semiconductors. The optimum wavelength was 2 μm for GaP and 3 μm for GaAs [S1].

III. I have designed GaP CG and GaAs CG THz sources by numerical calculation that can be used to achieve a collinear THz generation scheme with which the THz energy can be scalable with pump spot size and available crystal sizes. The optimum CG design parameters, i.e., the groove spacing, groove depth and duty cycle, that yield the highest diffraction efficiency in the ±1 diffraction orders satisfying the velocity matching condition have been determined. Such GaP and GaAs CGs THz sources can be used to achieve single-cycle THz pulses with energies of μJ to mJ energy range [S1,S2] .

IV. Using numerical calculations, I have shown that the diffraction efficiencies of the GaP CG and GaAs CG can be increased from 69-75% to 88-90% by adding an appropriate antireflective coating on the CG profiles. The antireflective coatings minimize Fresnel losses due to reflection. In particular, I have shown that by adding three different antireflective coatings, namely, SiO_2 AR, adding an AR of a material with a refractive index equal to the square root of the refractive index of the CG (GaP or GaAs) and adding a Norland optical adhesive 170 (NOA) AR, the diffraction efficiencies can significantly be enhanced [S2].

V. Due to the possible inaccuracy of the fabrication technique, the design parameters of the CGs may differ from the optimal values during fabrication. In order to achieve practical implementation, I have determined the tolerances of the design parameters that allow approximately a 7% decrease of diffraction efficiency. I have also shown that deviations of less than $\phi = 25^o$ (wall angle) from the perpendicular wall in the case of rectangular CG profiles, the diffraction efficiency loss is less than 5%. In contrast, beyond $\phi = 25^o$, the diffraction efficiency drops monotonically with an increase of wall angle. Therefore, during implementation, special attention should be taken not to exceed a wall angle of 25^o. I have also shown that the rectangular and trapezoidal profiles yield almost similar diffraction efficiencies [S2].

List of Publications

Publications related to the dissertation

[S1] **N. M. Mbithi**, G. Tóth, Z. Tibai, I. Benabdelghani, L. Nasi, G. Krizsán, J. Hebling, and G. Polonyi, "Investigation of terahertz pulse generation in semiconductors pumped at long infrared wavelengths," J. Opt. Soc. Am. B, (2022).

[S2] Z. Tibai, **N. M. Mbithi**, G. Almási, J. A. Fülöp and J. Hebling, " Design of semiconductor contact grating terahertz source with enhanced diffraction efficiency," Crystals, (2022).

Presentations

[E1] **N. M. Mbithi**, G. Krizsán, G. Polónyi, Z. Tibai, J. Hebling, and J. A. Fülöp, "Highly efficient THz pulse generation in semiconductors utilizing contact-gratings technology," in *High Intensity Lasers and High Field Phenomena*, (Optical Society of America, 2020), JW1A. 13.

[E2] **N. M. Mbithi**, G. Polónyi, Z. Tibai, G. Krizsán, L. Nasi, J. Hebling, J. A. Fülöp, Design of semiconductor contact-grating terahertz source for high energy terahertz pulse generation, MedPECS Medical Conference for PhD students and Experts of clinical Sciences, May 15 (2021).

[E3] G. Krizsán, **N. M. Mbithi**, G. Polónyi, G. Tóth, M. Mechler, J. Hebling, and J. A. Fülöp, "Semiconductors as Highly Efficient Single and Multicycle Terahertz Sources," in *The European Conference on Lasers and Electro-Optics*, (Optical Society of America, 2019), cc p22.

[E4] G. Krizsán, G. Polónyi, **N. M. Mbithi**, Z. Tibai, L. Pálfalvi, Gy. Tóth, L. Nasi, J. A. Fülöp and J. Hebling, Easily adaptable and scalable semiconductor THz pulse source, 46 th IRMMW-THz (2021).

[E5] G. Polónyi, P. Nugraha, **N.M. Mbithi**, G. Krizsán, B. Monoszlai, M. Mechler, G. Tóth, J. Hebling, and J. Fülöp, "Highly Efficient Scalable Semiconductor Terahertz Sources," in *2019 44th International Conference on Infrared, Millimeter, and Terahertz Waves (IRMMW-THz)*, (IEEE, 2019), 1-3.

[E6] J. A. Fülöp, G. Polónyi, K. Gergö, **N. M. Mbithi**, P. S. Nugraha, G. Almási, L. Pálfalvi, Z. Tibai, G. Tóth, and J. Hebling, "Novel intense single-and multicycle THz sources," in *2020 45th International Conference on Infrared, Millimeter, and Terahertz Waves (IRMMW-THz)*, (IEEE, 2020), 1-2.

[E7] J. A. Fülöp, G. Almási, G. Krizsán, **N. M. Mbithi**, M. I. Mechler, P. S. Nugraha, L. Pálfalvi, G. Polónyi, A. Sharma, and Z. Tibai, "Microstructured Intense THz Sources," in *Terahertz Science and Applications*, (Optica Publishing Group, 2019), TTh4D. 4.

Other publications

[S3] M. H. Abufadda, **N. M. Mbithi**, G. Polonyi, P. S. Nugraha, A. Buzady, J. Hebling, L. Molnar, and J. A. Fulop, "Absorption of Pulsed Terahertz and Optical Radiation in Earthworm Tissue and Its Heating Effect," J Infrared Millim Te **42**, 1065-1077 (2021).

References

1. D. L. Woolard, W. R. Loerop, and M. Shur, *Terahertz sensing technology: emerging scientific applications & novel device concepts* (World scientific, 2003), Vol. 2.
2. Y.-S. Lee, *Principles of terahertz science and technology* (Springer Science & Business Media, 2009), Vol. 170.
3. A. W. M. Lee, Q. Qin, S. Kumar, B. S. Williams, and Q. Hu, "Real-time terahertz imaging over a standoff distance (> 25 meters)," Appl. Phys. Lett. **89**, 141125 (2006).
4. A. Y. Pawar, D. D. Sonawane, K. B. Erande, and D. V. Derle, "Terahertz technology and its applications," Drug invent. today **5**, 157-163 (2013).
5. M. H. Alsharif, A. H. Kelechi, M. A. Albreem, S. A. Chaudhry, M. S. Zia, and S. Kim, "Sixth Generation (6G) Wireless Networks: Vision, Research Activities, Challenges and Potential Solutions," Symmetry-Basel **12**, 676 (2020).
6. T. Hattori, K. Tukamoto, and H. Nakatsuka, "Time-resolved study of intense terahertz pulses generated by a large-aperture photoconductive antenna," Jpn. J .Appl. Phys. 1 **40**, 4907-4912 (2001).
7. X. Ropagnol, M. Khorasaninejad, M. Raeiszadeh, S. Safavi-Naeini, M. Bouvier, C. Y. Cote, A. Laramee, M. Reid, M. A. Gauthier, and T. Ozaki, "Intense THz Pulses with large ponderomotive potential generated from large aperture photoconductive antennas," Opt. Express **24**, 11299-11311 (2016).
8. M. Clerici, M. Peccianti, B. E. Schmidt, L. Caspani, M. Shalaby, M. Giguere, A. Lotti, A. Couairon, F. Legare, T. Ozaki, D. Faccio, and R. Morandotti, "Wavelength scaling of terahertz generation by gas ionization," Phys. Rev. Lett. **110**, 253901 (2013).
9. M. D. Thomson, V. Blank, and H. G. Roskos, "Terahertz white-light pulses from an air plasma photo-induced by incommensurate two-color optical fields," Opt. Express **18**, 23173-23182 (2010).
10. K. Y. Kim, A. J. Taylor, J. H. Glownia, and G. Rodriguez, "Coherent control of terahertz supercontinuum generation in ultrafast laser-gas interactions," Nat. Photonics **2**, 605-609 (2008).
11. F. Blanchard, G. Sharma, X. Ropagnol, L. Razzari, R. Morandotti, and T. Ozaki, "Improved terahertz two-color plasma sources pumped by high intensity laser beam," Opt. Express **17**, 6044-6052 (2009).
12. A. Gopal, S. Herzer, A. Schmidt, P. Singh, A. Reinhard, W. Ziegler, D. Brommel, A. Karmakar, P. Gibbon, U. Dillner, T. May, H. G. Meyer, and G. G. Paulus, "Observation of gigawatt-class THz pulses from a compact laser-driven particle accelerator," Phys. Rev. Lett. **111**, 074802 (2013).
13. A. G. Stepanov, J. Kuhl, I. Z. Kozma, E. Riedle, G. Almási, and J. Hebling, "Scaling up the energy of THz pulses created by optical rectification," Opt. Express **13**(2005).
14. B. Zhang, Z. Ma, J. Ma, X. Wu, C. Ouyang, D. Kong, T. Hong, X. Wang, P. Yang, L. Chen, Y. Li, and J. Zhang, "1.4-mJ High Energy Terahertz Radiation from Lithium Niobates," Laser Photonics Rev. **15**(2021).
15. S. W. Huang, E. Granados, W. R. Huang, K. H. Hong, L. E. Zapata, and F. X. Kartner, "High conversion efficiency, high energy terahertz pulses by optical rectification in cryogenically cooled lithium niobate," Opt. Lett. **38**, 796-798 (2013).
16. C. Gollner, M. Shalaby, C. Brodeur, I. Astrauskas, R. Jutas, E. Constable, L. Bergen, A. Baltuska, and A. Pugzlys, "Highly efficient THz generation by optical rectification of mid-IR pulses in DAST," Apl. Photonics **6**, 046105 (2021).
17. C. Vicario, A. V. Ovchinnikov, S. I. Ashitkov, M. B. Agranat, V. E. Fortov, and C. P. Hauri, "Generation of 0.9-mJ THz pulses in DSTMS pumped by a Cr:Mg(2)SiO(4) laser," Opt. Lett. **39**, 6632-6635 (2014).
18. C. Vicario, B. Monoszlai, M. Jazbinsek, S. H. Lee, O. P. Kwon, and C. P. Hauri, "Intense, carrier frequency and bandwidth tunable quasi single-cycle pulses from an organic emitter covering the Terahertz frequency gap," Sci. Rep. **5**, 14394 (2015).
19. G. Polonyi, B. Monoszlai, G. Gaumann, E. J. Rohwer, G. Andriukaitis, T. Balciunas, A. Pugzlys, A. Baltuska, T. Feurer, J. Hebling, and J. A. Fulop, "High-energy terahertz

pulses from semiconductors pumped beyond the three-photon absorption edge," Opt. Express **24**, 23872-23882 (2016).
20. J. Xu, B. Globisch, C. Hofer, N. Lilienfein, T. Butler, N. Karpowicz, and I. Pupeza, "Three-octave terahertz pulses from optical rectification of 20 fs, 1 μm, 78 MHz pulses in GaP," J. Phys. B: At. Mol. Opt. Phys. **51**(2018).
21. F. Blanchard, B. E. Schmidt, X. Ropagnol, N. Thiré, T. Ozaki, R. Morandotti, D. G. Cooke, and F. Légaré, "Terahertz pulse generation from bulk GaAs by a tilted-pulse-front excitation at 1.8 μm," Appl. Phys. Lett. **105**(2014).
22. X. D. Mu, I. B. Zotova, and Y. J. Ding, "Power scaling on efficient generation of ultrafast terahertz pulses," IEEE J. Sel. Top. Quantum Electron. **14**, 315-332 (2008).
23. K. Zhong, W. Shi, D. Xu, P. Liu, Y. Wang, J. Mei, C. Yan, S. Fu, and J. Yao, "Optically pumped terahertz sources," Sci. China Technol. Sci. **60**, 1801-1818 (2017).
24. J. A. Fulop, Z. Ollmann, C. Lombosi, C. Skrobol, S. Klingebiel, L. Palfalvi, F. Krausz, S. Karsch, and J. Hebling, "Efficient generation of THz pulses with 0.4 mJ energy," Opt. Express **22**, 20155-20163 (2014).
25. H. A. Hafez, X. Chai, A. Ibrahim, S. Mondal, D. Férachou, X. Ropagnol, and T. Ozaki, "Intense terahertz radiation and their applications," J. Opt. **18**(2016).
26. H. Guerboukha, K. Nallappan, and M. Skorobogatiy, "Toward real-time terahertz imaging," Adv. Opt. Photonics **10**, 843-938 (2018).
27. M. Jewariya, E. Abraham, T. Kitaguchi, Y. Ohgi, M. Minami, T. Araki, and T. Yasui, "Fast three-dimensional terahertz computed tomography using real-time line projection of intense terahertz pulse," Opt. Express **21**, 2423-2433 (2013).
28. L. Palfalvi, J. A. Fulop, G. Toth, and J. Hebling, "Evanescent-wave proton postaccelerator driven by intense THz pulse," Phys. Rev. Spec. Top.-Ac. **17**, 031301 (2014).
29. K. Kitano, N. Ishii, and J. Itatani, "High degree of molecular orientation by a combination of THz and femtosecond laser pulses," Phys. Rev. A **84**, 053408 (2011).
30. W. R. Huang, S. W. Huang, E. Granados, K. Ravi, K. H. Hong, L. E. Zapata, and F. X. Kartner, "Highly efficient terahertz pulse generation by optical rectification in stoichiometric and cryo-cooled congruent lithium niobate," J. Mod. Opt. **62**, 1486-1493 (2015).
31. H. Hirori and K. Tanaka, "Nonlinear optical phenomena induced by intense single-cycle terahertz pulses," IEEE J. Sel. Top. Quantum Electron. **19**, 8401110-8401110 (2012).
32. R. Shimano, S. Watanabe, and R. Matsunaga, "Intense Terahertz Pulse-Induced Nonlinear Responses in Carbon Nanotubes," J. Infrared Millim. Te. **33**, 861-869 (2012).
33. G. Imeshev, M. E. Fermann, K. L. Vodopyanov, M. M. Fejer, X. Yu, J. S. Harris, D. Bliss, and C. Lynch, "High-power source of THz radiation based on orientation-patterned GaAs pumped by a fiber laser," Opt. Express **14**, 4439-4444 (2006).
34. F. Junginger, B. Mayer, C. Schmidt, O. Schubert, S. Mahrlein, A. Leitenstorfer, R. Huber, and A. Pashkin, "Nonperturbative interband response of a bulk InSb semiconductor driven off resonantly by terahertz electromagnetic few-cycle pulses," Phys. Rev. Lett. **109**, 147403 (2012).
35. K. Kawase, Y. Ogawa, Y. Watanabe, and H. Inoue, "Non-destructive terahertz imaging of illicit drugs using spectral fingerprints," Opt. Express **11**, 2549-2554 (2003).
36. T. Kampfrath, K. Tanaka, and K. A. Nelson, "Resonant and nonresonant control over matter and light by intense terahertz transients," Nat. Photonics **7**, 680-690 (2013).
37. K. Zhong, W. Shi, D. Xu, P. Liu, Y. Wang, J. Mei, C. Yan, S. Fu, and J. Yao, "Optically pumped terahertz sources," Sci. China Technol. Sci. **60**, 1801-1818 (2017).
38. A. Sharma, Z. Tibai, and J. Hebling, "Intense tera-hertz laser driven proton acceleration in plasmas," Phys. Plasmas **23**, 063111 (2016).
39. L. Pálfalvi, J. Fülöp, G. Tóth, and J. Hebling, "Evanescent-wave proton postaccelerator driven by intense THz pulse," Phys. Rev. Special Top.-Acc. Beams **17**, 031301 (2014).

40. P. Salén, M. Basini, S. Bonetti, J. Hebling, M. Krasilnikov, A. Y. Nikitin, G. Shamuilov, Z. Tibai, V. Zhaunerchyk, and V. Goryashko, "Matter manipulation with extreme terahertz light: Progress in the enabling THz technology," Phys. Rep. **836-837**, 1-74 (2019).
41. L. J. Wong, A. Fallahi, and F. X. Kartner, "Compact electron acceleration and bunch compression in THz waveguides," Opt. Express **21**, 9792-9806 (2013).
42. E. A. Nanni, W. R. Huang, K. H. Hong, K. Ravi, A. Fallahi, G. Moriena, R. J. Miller, and F. X. Kartner, "Terahertz-driven linear electron acceleration," Nat. Commun. **6**, 8486 (2015).
43. J. Hebling, J. Fülöp, M. Mechler, L. Pálfalvi, C. Tőke, and G. Almási, "Optical manipulation of relativistic electron beams using THz pulses," arXiv: .05739 (2011).
44. R. W. Boyd, *Nonlinear optics* (Academic press, 2020).
45. M. Bass, P. Franken, J. Ward, and G. Weinreich, "Optical rectification," Phys. Rev. Lett. **9**, 446 (1962).
46. K. Yang, P. Richards, and Y. Shen, "Generation of far-infrared radiation by picosecond light pulses in LiNbO3," Appl. Phys. Lett. **19**, 320-323 (1971).
47. D. H. Auston, K. P. Cheung, J. A. Valdmanis, and D. A. Kleinman, "Cherenkov Radiation from Femtosecond Optical Pulses in Electro-Optic Media," Phys. Rev. Lett. **53**, 1555-1558 (1984).
48. K. Y. Kim, J. H. Glownia, A. J. Taylor, and G. Rodriguez, "Terahertz emission from ultrafast ionizing air in symmetry-broken laser fields," Opt. Express **15**, 4577-4584 (2007).
49. M. C. Hoffmann and J. A. Fulop, "Intense ultrashort terahertz pulses: generation and applications," J. Phys. D Appl .Phys. **44**, 083001 (2011).
50. R. Huber, A. Brodschelm, F. Tauser, and A. Leitenstorfer, "Generation and field-resolved detection of femtosecond electromagnetic pulses tunable up to 41 THz," Appl. Phys. Lett. **76**, 3191-3193 (2000).
51. J. Hebling, K.-L. Yeh, M. C. Hoffmann, B. Bartal, and K. A. Nelson, "Generation of high-power terahertz pulses by tilted-pulse-front excitation and their application possibilities," J. Opt. Soc. Am. B **25**, B6-B19 (2008).
52. J. A. Fulop, L. Palfalvi, G. Almasi, and J. Hebling, "Design of high-energy terahertz sources based on optical rectification," Opt. Express **18**, 12311-12327 (2010).
53. K. Ravi, W. R. Huang, S. Carbajo, X. J. Wu, and F. Kartner, "Limitations to THz generation by optical rectification using tilted pulse fronts," Opt. Express **22**, 20239-20251 (2014).
54. A. Schneider, M. Neis, M. Stillhart, B. Ruiz, R. U. A. Khan, and P. Gunter, "Generation of terahertz pulses through optical rectification in organic DAST crystals: theory and experiment," J. Opt. Soc. Am. B **23**, 1822-1835 (2006).
55. F. Blanchard, B. Schmidt, X. Ropagnol, N. Thiré, T. Ozaki, R. Morandotti, D. Cooke, and F. L. Légaré, "Terahertz pulse generation from bulk GaAs by a tilted-pulse-front excitation at 1.8 μ m," Appl. Phy. **105**, 241106 (2014).
56. J. A. Fülöp, G. Polónyi, B. Monoszlai, G. Andriukaitis, T. Balciunas, A. Pugzlys, G. Arthur, A. Baltuska, and J. Hebling, "Highly efficient scalable monolithic semiconductor terahertz pulse source," Optica **3**(2016).
57. J. Hebling, A. G. Stepanov, G. Almaasi, B. Bartal, and J. Kuhl, "Tunable THz pulse generation by optical rectification of ultrashort laser pulses with tilted pulse fronts," Appl. Phys. B: Lasers Opt. **78**, 593-599 (2004).
58. J. Hebling, G. Almasi, I. Z. Kozma, and J. Kuhl, "Velocity matching by pulse front tilting for large-area THz-pulse generation," Opt. Express **10**, 1161-1166 (2002).
59. J. Hebling, "Derivation of the pulse front tilt caused by angular dispersion," Opt. Quantum Electron. **28**, 1759-1763 (1996).
60. K. Y. Kim, *Recent Optical and Photonic Technologies* (BoD–Books on Demand, 2010).

61. R. J. Lanzafame, "Ultrashort Laser Pulse Phenomena: Fundamentals, Techniques, and Applications on a Femtosecond Time Scale, by Jean-Claude Diels and Wolfgang Rudolph," Photomed. Laser Thera. **25**, 58-58 (2007).

62. J. E. Nkeck, X. Ropagnol, R. Nechache, and F. Blanchard, "Electro-optical detection of terahertz radiation in a zinc sulphide crystal at a wavelength of 512 nm," Appl. Phys. Express **13**(2020).

63. X. Xie, J. Xu, and X. C. Zhang, "Terahertz wave generation and detection from a cdte crystal characterized by different excitation wavelengths," Opt. Lett. **31**, 978-980 (2006).

64. O. Hatem, "Optimizing the electro-optic detection of terahertz waves by ZnTe at 780 and 1560-nm probe-beam wavelengths," J. Nonlinear Opt. Phys. Mater. **27**, 1850043 (2018).

65. M. I. Bakunov, S. B. Bodrov, and E. A. Mashkovich, "Terahertz generation with tilted-front laser pulses: dynamic theory for low-absorbing crystals," J. Opt. Soc. Am. B **28**, 1724-1734 (2011).

66. A. Nahata, A. S. Weling, and T. F. Heinz, "A wideband coherent terahertz spectroscopy system using optical rectification and electro-optic sampling," Appl. phys. lett. **69**, 2321-2323 (1996).

67. M. Nagai, K. Tanaka, H. Ohtake, T. Bessho, T. Sugiura, T. Hirosumi, and M. Yoshida, "Generation and detection of terahertz radiation by electro-optical process in GaAs using 1.56 μ m fiber laser pulses," Appl. phys. lett. **85**, 3974-3976 (2004).

68. J. A. Fülöp, S. Tzortzakis, and T. Kampfrath, "Laser-Driven Strong-Field Terahertz Sources," Adv. Opt. Mater. (2019).

69. M. C. Hoffmann, K. L. Yeh, J. Hebling, and K. A. Nelson, "Efficient terahertz generation by optical rectification at 1035 nm," Opt. Express **15**, 11706-11713 (2007).

70. J. Fülöp, L. Pálfalvi, G. Almási, and J. Hebling, "Design of high-energy terahertz sources based on optical rectification," Opt. express **18**, 12311-12327 (2010).

71. C. Vicario, M. Jazbinsek, A. V. Ovchinnikov, O. V. Chefonov, S. I. Ashitkov, M. B. Agranat, and C. P. Hauri, "High efficiency THz generation in DSTMS, DAST and OH1 pumped by Cr:forsterite laser," Opt. Express **23**, 4573-4580 (2015).

72. Z. Li, P. Bing, and S. Yuan, "Terahertz generation by DSTMS based on cascaded difference frequency generation," Optik **127**, 3552-3555 (2016).

73. C. Ruchert, C. Vicario, and C. P. Hauri, "Scaling submillimeter single-cycle transients toward megavolts per centimeter field strength via optical rectification in the organic crystal OH1," Opt. Lett. **37**, 899-901 (2012).

74. A. Rovere, Y. G. Jeong, R. Piccoli, S. H. Lee, S. C. Lee, O. P. Kwon, M. Jazbinsek, R. Morandotti, and L. Razzari, "Generation of high-field terahertz pulses in an HMQ-TMS organic crystal pumped by an ytterbium laser at 1030 nm," Opt. Express **26**, 2509-2516 (2018).

75. Y. Shirota and H. Kageyama, "Handbook of Organic Materials for Optical Devices," (Elsevier: Amsterdam, The Netherlands, 2013).

76. C. Vicario, B. Monoszlai, and C. P. Hauri, "GV/mSingle-Cycle Terahertz Fields from a Laser-Driven Large-Size Partitioned Organic Crystal," Phys. Rev. Lett. **112**(2014).

77. K. L. Yeh, M. C. Hoffmann, J. Hebling, and K. A. Nelson, "Generation of 10μJ ultrashort terahertz pulses by optical rectification," Appl. Phys. Lett. **90**(2007).

78. A. G. Stepanov, S. Henin, Y. Petit, L. Bonacina, J. Kasparian, and J. P. Wolf, "Mobile source of high-energy single-cycle terahertz pulses," Appl. Phys. B: Lasers Opt. **101**, 11-14 (2010).

79. X. J. Wu, J. L. Ma, B. L. Zhang, S. S. Chai, Z. J. Fang, C. Y. Xia, D. Y. Kong, J. G. Wang, H. Liu, C. Q. Zhu, X. Wang, C. J. Ruan, and Y. T. Li, "Highly efficient generation of 0.2 mJ terahertz pulses in lithium niobate at room temperature with sub-50 fs chirped Ti:sapphire laser pulses," Opt. Express **26**, 7107-7116 (2018).

80. M. Kunitski, M. Richter, M. D. Thomson, A. Vredenborg, J. Wu, T. Jahnke, M. Schöffler, H. Schmidt-Böcking, H. G. Roskos, and R. Dörner, "Optimization of single-

cycle terahertz generation in LiNbO 3 for sub-50 femtosecond pump pulses," Opt. Express **21**, 6826-6836 (2013).
81. J. A. Fulop, L. Palfalvi, M. C. Hoffmann, and J. Hebling, "Towards generation of mJ-level ultrashort THz pulses by optical rectification," Opt. Express **19**, 15090-15097 (2011).
82. H. Hirori, A. Doi, F. Blanchard, and K. J. A. P. L. Tanaka, "Single-cycle terahertz pulses with amplitudes exceeding 1 MV/cm generated by optical rectification in LiNbO 3," Opt. Express **98**, 091106 (2011).
83. L. Pálfalvi, J. A. Fülöp, G. Almási, and J. Hebling, "Novel setups for extremely high power single-cycle terahertz pulse generation by optical rectification," Appl. Phys. Lett. **92**(2008).
84. M. Tsubouchi, K. Nagashima, F. Yoshida, Y. Ochi, and M. Maruyama, "Contact grating device with Fabry–Perot resonator for effective terahertz light generation," Opt. lett. **39**, 5439-5442 (2014).
85. L. Pálfalvi, Z. Ollmann, L. Tokodi, and J. Hebling, "Hybrid tilted-pulse-front excitation scheme for efficient generation of high-energy terahertz pulses," Opt. Express **24**, 8156-8169 (2016).
86. L. Pálfalvi, G. Tóth, L. Tokodi, Z. Márton, J. A. Fülöp, G. Almási, and J. Hebling, "Numerical investigation of a scalable setup for efficient terahertz generation using a segmented tilted-pulse-front excitation," Opt. express **25**, 29560-29573 (2017).
87. P. S. Nugraha, G. Krizsan, C. Lombosi, L. Palfalvi, G. Toth, G. Almasi, J. A. Fulop, and J. Hebling, "Demonstration of a tilted-pulse-front pumped plane-parallel slab terahertz source," Opt. Lett. **44**, 1023-1026 (2019).
88. Y. K. Danileiko, A. Manenkov, and A. Sidorin, "10.6 um, 2. 76 um, and 2.94 um radiation wavelengths of the pulsed CO2, Ca2F: Er3+ and YAG: Er3+ lasers is investigated. Generation of free," J NBS Special Publication, 305 (1979).
89. M. J. Weber, *Handbook of optical materials* (CRC press, 2018).
90. P. S. Nugraha, G. Krizsan, G. Polonyi, M. I. Mechler, J. Hebling, G. Toth, and J. A. Fulop, "Efficient semiconductor multicycle terahertz pulse source," J. Phys. B-at. Mol. Opt. **51**(2018).
91. J. Wei, J. M. Murray, J. O. Barnes, D. M. Krein, P. G. Schunemann, and S. Guha, "Temperature dependent Sellmeier equation for the refractive index of GaP," Opt. Mater. Express **8**(2018).
92. Q. Wu and X. C. Zhang, "7 terahertz broadband GaP electro-optic sensor," Appl. Phys. Lett. **70**, 1784-1786 (1997).
93. Y. A. Goldberg, "Gallium phosphide (GaP)," Handbook series on semiconductor parameters **1**, 104-124 (1996).
94. S. Griffin, S. Knapen, T. Y. Lin, and K. M. Zurek, "Directional detection of light dark matter with polar materials," Phys. Rev. D **98**(2018).
95. G. Chang, C. J. Divin, C. H. Liu, S. L. Williamson, A. Galvanauskas, and T. B. Norris, "Power scalable compact THz system based on an ultrafast Yb-doped fiber amplifier," Opt. Express **14**, 7909-7913 (2006).
96. M. Nagai, K. Tanaka, H. Ohtake, T. Bessho, T. Sugiura, T. Hirosumi, and M. Yoshida, "Generation and detection of terahertz radiation by electro-optical process in GaAs using 1.56 mu m fiber laser pulses," Appl. Phys. Lett. **85**, 3974-3976 (2004).
97. F. Blanchard, L. Razzari, H.-C. Bandulet, G. Sharma, R. Morandotti, J.-C. Kieffer, T. Ozaki, M. Reid, H. Tiedje, and H. Haugen, "Generation of 1.5 μJ single-cycle terahertz pulses by optical rectification from a large aperture ZnTe crystal," Opt. Express **15**, 13212-13220 (2007).
98. K. Aoki, J. Savolainen, and M. Havenith, "Broadband terahertz pulse generation by optical rectification in GaP crystals," Appl. Phys. Lett. **110**(2017).
99. G. Polónyi, M. I. Mechler, J. Hebling, and J. A. Fülöp, "Prospects of Semiconductor Terahertz Pulse Sources," IEEE J. Sel. Top. Quantum Elecron. **23**, 1-8 (2017).

100. F. Liu, Y. F. Li, Q. R. Xing, L. Chai, M. L. Hu, C. L. Wang, Y. Q. Deng, Q. Sun, and C. Y. Wang, "Three-photon absorption and Kerr nonlinearity in undoped bulk GaP excited by a femtosecond laser at 1040 nm," J. Opt. **12**, 095201 (2010).
101. W. C. Hurlbut, Y. S. Lee, K. L. Vodopyanov, P. S. Kuo, and M. M. Fejer, "Multiphoton absorption and nonlinear refraction of GaAs in the mid-infrared," Opt. Lett. **32**, 668-670 (2007).
102. K. L. Vodopyanov, "Optical THz-wave generation with periodically-inverted GaAs," Laser Photonics Rev. **2**, 11-25 (2008).
103. B. S. Wherrett, "Scaling Rules for Multiphoton Interband Absorption in Semiconductors," J. Opt. Soc. Am. B **1**, 67-72 (1984).
104. S. Benis, C. M. Cirloganu, N. Cox, T. Ensley, H. Hu, G. Nootz, P. D. Olszak, L. A. Padilha, D. Peceli, and M. Reichert, "Three-photon absorption spectra and bandgap scaling in direct-gap semiconductors," Optica **7**, 888-899 (2020).
105. V. Nathan, A. H. Guenther, and S. S. Mitra, "Review of Multiphoton Absorption in Crystalline Solids," J. Opt. Soc. Am. B **2**, 294-316 (1985).
106. L. Keldysh, "Ionization in the field of a strong electromagnetic wave," J Sov. Phys. JETP **20**, 1307-1314 (1965).
107. C. Lombosi, G. Polónyi, M. Mechler, Z. Ollmann, J. Hebling, and J. A. Fülöp, "Nonlinear distortion of intense THz beams," New J. Phys. **17**(2015).
108. K. Ravi, W. R. Huang, S. Carbajo, X. J. Wu, and F. Kartner, "Limitations to THz generation by optical rectification using tilted pulse fronts," Opt. Express **22**, 20239-20251 (2014).
109. Z. Ollmann, J. A. Fulop, J. Hebling, and G. Almasi, "Design of a high-energy terahertz pulse source based on ZnTe contact grating," Opt. Commun. **315**, 159-163 (2014).
110. P. Y. Yu and M. Cardona, "Vibrational properties of semiconductors, and electron-phonon interactions," in *Fundamentals of Semiconductors* (Springer, 2010), pp. 107-158.
111. A. A. Said, M. Sheikbahae, D. J. Hagan, T. H. Wei, J. Wang, J. Young, and E. W. Vanstryland, "Determination of Bound-Electronic and Free-Carrier Nonlinearities in Znse, Gaas, CdTe, and Znte," J. Opt. Soc. Am. B: Opt. Phys. **9**, 405-414 (1992).
112. B. Monoszlai, P. S. Nugraha, G. Tóth, G. Polónyi, L. Pálfalvi, L. Nasi, Z. Ollmann, E. J. Rohwer, G. Gäumann, J. Hebling, T. Feurer, and J. A. Fülöp, "Measurement of four-photon absorption in GaP and ZnTe semiconductors," Opt. Express **28**(2020).
113. B. U. Sohn, M. Kang, J. W. Choi, A. M. Agarwal, K. Richardson, and D. T. H. Tan, "Observation of very high order multi-photon absorption in GeSbS chalcogenide glass," Apl. Photonics **4**(2019).
114. I. Vurgaftman, J. R. Meyer, and L. R. Ram-Mohan, "Band parameters for III-V compound semiconductors and their alloys," J. Appl. Phys. **89**, 5815-5875 (2001).
115. A. H. Kachare, W. G. Spitzer, and J. E. Fredrickson, "Refractive index of ion-implanted GaAs," J. Appl. Phys. **47**, 4209-4212 (1976).
116. D. Parsons and P. J. A. o. Coleman, "Far infrared optical constants of gallium phosphide," **10**, 1683_1681-1685 (1971).
117. E. D. Palik, *Handbook of optical constants of solids* (Academic press, 1998), Vol. 3.
118. M. Bashirpour, W. Cui, A. Gamouras, and J. M. Menard, "Scalable Fabrication of Nanogratings on GaP for Efficient Diffraction of Near-Infrared Pulses and Enhanced Terahertz Generation by Optical Rectification," Crystals **12**, 684 (2022).
119. M. G. Moharam and T. K. Gaylord, "Diffraction Analysis of Dielectric Surface-Relief Gratings," J. Opt. Soc. Am. **72**, 1385-1392 (1982).
120. W. B. Zimmerman, *Multiphysics modeling with finite element methods* (World Scientific Publishing Company, 2006), Vol. 18.
121. M. Sheik-Bahae, D. C. Hutchings, D. J. Hagan, and E. W. Van Stryland, "Dispersion of bound electron nonlinear refraction in solids," IEEE J. Quantum Electron. **27**, 1296-1309 (1991).

122. T. K. Gaylord, W. E. Baird, and M. G. Moharam, "Zero-reflectivity high spatial-frequency rectangular-groove dielectric surface-relief gratings," Appl. Opt. **25**, 4562 (1986).
123. G. Krizsán, Z. Tibai, G. Almási, G. Tóth, L. Pálfalvi, and J. Hebling, "New Generation Terahertz Pulse Sources Utilizing Volume Phase Holographic Gratings," in *High Intensity Lasers and High Field Phenomena*, (Optica Publishing Group, 2022), HF3B. 6.
124. J. E. Harvey and R. N. Pfisterer, "Understanding diffraction grating behavior: including conical diffraction and Rayleigh anomalies from transmission gratings," Opt. Eng. **58**, 087105 (2019).
125. T. Clausnitzer, J. Limpert, K. Zollner, H. Zellmer, H. J. Fuchs, E. B. Kley, A. Tunnermann, M. Jupe, and D. Ristau, "Highly efficient transmission gratings in fused silica for chirped-pulse amplification systems," Appl. Opt. **42**, 6934-6938 (2003).
126. Z. Ollmann, J. Hebling, and G. Almási, "Design of a contact grating setup for mJ-energy THz pulse generation by optical rectification," Appl. Phys. B **108**, 821-826 (2012).
127. Z. Ollmann, J. A. Fülöp, J. Hebling, and G. Almási, "Design of a high-energy terahertz pulse source based on ZnTe contact grating," Opt. Commun. **315**, 159-163 (2014).
128. W. Cui, K. M. Awan, R. Huber, K. Dolgaleva, and J. M. Ménard, "Broadband and High-Sensitivity Time-Resolved THz System Using Grating-Assisted Tilted-Pulse-Front Phase Matching," Adv. Opt. Mater. **10**, 2101136 (2022).
129. T. Clausnitzer, T. Kampfe, E. B. Kley, A. Tunnermann, U. Peschel, A. V. Tishchenko, and O. Parriaux, "An intelligible explanation of highly-efficient diffraction in deep dielectric rectangular transmission gratings," Opt. Express **13**, 10448-10456 (2005).
130. N. M. Mbithi, G. Tóth, Z. Tibai, I. Benabdelghani, L. Nasi, G. Krizsán, J. Hebling, and G. Polonyi, "Investigation of terahertz pulse generation in semiconductors pumped at long infrared wavelengths," J. Opt. Soc. Am. B (2022).

Funding

This work was supported and funded by National Research, Development, and Innovation Office (2018-1.2.1-NKP-2018-00009 and 2018 1.2.1-NKP-2018-00010), the Hungarian Scientific Research Fund (OTKA) (12934).